Studying Permafrost and Active Layer Dynamics in Tibet and Arctic by Multi-temporal Radar Interferometry

CHEN, Jie

A Thesis Submitted in Partial Fulfilment

of the Requirements for the Degree of

Doctor of Philosophy

in

Earth System and GeoInformation Science

The Chinese University of Hong Kong

September 2019

Thesis Assessment Committee

Professor HUANG Bo (Chair)

Professor LIN Hui (Thesis Supervisor)

Professor LIU Lin (Thesis Co-supervisor)

Professor ZHANG Hongsheng (Committee Member)

Professor ZHOU Qiming (External Examiner)

Abstract

of thesis entitled:

Studying Permafrost and Active Layer Dynamics in Tibet and Arctic by Multi-temporal Radar Interferometry

Submitted by **CHEN, Jie**

for the degree of **Doctor of Philosophy**

at **The Chinese University of Hong Kong**

in **September 2019**

supervised by **Prof. LIN, Hui and Prof. LIU, Lin**

Permafrost, extremely ice-rich permafrost, is vulnerable to thawing and degradation under continuous climatic warming. Generally, in permafrost region the ground surface subsides/uplifts seasonally as a result of the volumetric contraction/expansion due to moisture phase transition between the frozen and unfrozen soil in the active layer. In addition, the thawing of excess ground ice in the uppermost permafrost layer might trigger secular subsidence and/or the formation of thermokarst landforms. The dynamic processes between the active layer and underlying permafrost interacts with local and regional hydrological, ecological, and geomorphological processes, leading to changes in ground thermal regime and the energy exchanges between the land surface and the atmosphere. Furthermore, permafrost thaw subsidence can severely damage buildings and infrastructure stability. However, permafrost and active layer dynamics remains poorly quantified or understood both in Tibet and Arctic. The aim of this thesis is to map and quantify the gradual elevation changes in permafrost

environment using multi-temporal radar interferometry and ground measurements. To achieve this goal, I selected three study sites with different permafrost landforms in Tibet and Arctic.

Thermal erosion gullies, typical thermokarst landforms, are well developed on a north-facing slope of Eboling Mountain near the northern edge of Tibet. I introduced the piecewise elevation change model that includes the seasonal elevation changes and the linear subsidence trends. I incorporated the model into the developed persistent scatterer interferometry approach to exploit all repeat ALOS-1 SAR acquisitions at a fine spatial resolution of about 7 m. I found that the gradual permafrost thaw subsidence occurs both inside and around the thermal erosion gullies between 2006 and 2011. The subsidence trends were up to 3 cm/yr inside and around the thermal erosion gullies, suggesting that 28% of the study area experiences permafrost thaw processes, which is about 40 times larger than the visible gullies. The spatial pattern of gradual subsidence trends showed correlations between the gullies and their surroundings, suggesting that the permafrost thaws and degrades in a wider region than the gullies. I demonstrated the potentials of using persistent scatterer interferometry to study permafrost thaw processes and to assess its impacts over vast areas, especially with low vegetation and shallow snow cover.

I explored and successfully tested the capability of Sentinel-1 InSAR measurements for quantifying both permafrost thaw subsidence during one thaw season and the inter-annual elevation changes between two thaw seasons in Sobo-Sise Island, Lena River Delta. Compared with X-band InSAR in Yedoma uplands, the C-band Sentinel-1 InSAR showed higher coherence, even for the interferograms between the years. I also found that the flat tops of Yedoma uplands exhibit the highest seasonal elevation changes. Benefiting from the Sentinel-1 InSAR measurements with short time intervals (12 days in this case), I found that delayed thawing associated with air

temperature fluctuations affects inter-annual elevation changes.

I used an advanced small baseline interferometry to quantifying the long-term ground subsidence by exploiting both persistent scatterer and distributed scatterer in Bayelva catchment, Spitsbergen. The long-term subsidence trends reached to about 5-8 cm during the past 20 years, together with the long-term ground measurements, suggesting the permafrost is thawing and degrading. I also found some of the buildings were undergoing strong subsidence, which might serve as an alarm. In addition, by simulating interferometric phase based on soil moisture measurements, I found that InSAR-derived ground uplift might be overestimated due to the fast soil moisture dropping during the freezing stage, which also acts as "uplift".

This thesis demonstrates the potential and capability of multi-temporal radar interferometry to detecting permafrost-related elevation changes both in Tibet and Arctic. The multi-temporal radar interferometry approach developed can be used to other permafrost environments. The derived subsidence maps might help people to better understand the permafrost and active layer dynamics.

摘要

多年凍土，尤其是富冰多年凍土，在持續氣候變暖情況下極容易融化和退化。一般來說，活動層中冰與水之間的相位轉變會引起體積的收縮/膨脹，進而導致地面季節性的下沉/抬升。另外，多年凍土最上面一層過量冰的融化會導致長期的地面沉降以及/或者熱喀斯特地貌的形成。活動層和多年凍土之間的動態過程與地方性或者區域性的水文、生態以及地貌過程之間相互影響，影響著地面熱狀況和陸地與大氣之間的能量交換。多年凍土融化引起的地面沉降可能會造成嚴重的建築物和公共設施的破壞。然而，青藏高原和北極的多年凍土和活動層的動態過程仍然缺乏量化或者理解。這篇論文的目的就是利用多時相合成孔徑雷達干涉測量技術（InSAR）和地面觀測來繪製并量化多年凍土區的地面沉降。為此，我選擇了三個不同地貌的研究區域：一個在青藏高原，兩個在北極。

在青藏高原北部俄博嶺山的一個北坡上，熱力侵蝕溝發育良好。熱力侵蝕溝是一種典型的熱喀斯特地貌。我引入了包含季節性以及長期性的分段地面形變模型并把這個模型并入了多年散射體InSAR技術。因此我可以使用全部可用的合成孔徑雷達影像并達到7米左右的分辨率。我發現地表沉降發生在熱力侵蝕溝以及周邊在2006-2011年間。沉降趨勢達到了每年3釐米，這表明28%的區域經歷著多年凍土融化過程。這大概是熱力侵蝕溝面積的40倍。熱力侵蝕溝內和周邊的地面沉降有一定的相關性，這表明多年凍土融化不僅發生在溝內也發生在溝邊更大的範圍。我展示了多年散射體InSAR技術的在研究多年凍土融化過程，尤其是在植被和積雪稀少的區域的潛力。

我探索并成功檢驗了Sentinel-1 InSAR在業叨碼凍土地面沉降的能力。我量化了季節內以及年間的地面沉降在勒拿河三角洲的Sobo-Sise島。和X波段InSAR相比，C波段Sentinel-1 InSAR展示了更高的相干性，即使是年間的干涉圖。我發現

平坦的高地經歷了最大的地面形變。獲益于Sentinel-1時間更短的重訪週期（12天在這個例子中），我還發現氣温波動影響著凍融過程進而影響地面沉降的幅度。
在斯瓦爾巴的Bayelva流域，我利用先進的小基線干涉技術（同時包含永久散射體和分佈式散射體目標）量化了長期的地面沉降。長期的地面沉降在過去的20年間達到了5-8釐米。地表沉降以及地面觀測都表明了這個區域的多年凍土在融化和退化。我還發現這個區域的一些房屋經歷著形變，這可以作為一個早期預警。另外，通過用土壤水觀測模擬干涉相位，我發現多時相InSAR推導的地面抬升值可能被高估了。這是由於在凍結過程中土壤水的變化可能會影響InSAR的相位變化，進而導致類似的“地面抬升”信號。
本論文證實了多時相InSAR技術在量化多年凍土區地面沉降方面的潛力和能力。本文中開發的多時相InSAR區域可以使用在其他多年凍土區域。本文的地面沉降結果可能會幫到人們更好的理解多年凍土和活動層的動態過程。

Acknowledgments

There are many people to whom I would like to express my fully gratitude during the past four and half year.

First of all, I would like to express my sincere gratitude to my supervisor, Prof. Hui Lin, for his support and encouragement both in research and life throughout my doctoral studies. Prof. Lin always emphasizes the important of scientific-oriented research with his infectious enthusiasm and unique visions, which inspires me a lot. The special thanks to my co-supervisor Prof. Lin Liu both as a independent researcher and as a person. I greatly appreciate and enjoy all the discussions between us, which is one of the most invaluable things for me. I also appreciate for his support on my participation of international conferences and workshops. He supported me with his knowledge of permafrost science and precious scientific writing advice.

My deeply appreciation also goes to Prof. Irena Hajnsek for her host and support during my ETH visit. As one of the world-leading polarimetric SAR group, her knowledge and special views help me treat the problems in new ways. Many thanks to the colleagues in ETH, Dr. Simon Zwieback, Dr. Silvan Leinss, Dr. Simon Baffelli, Dr. Philipp Bernhard, Lanqing Huang. I really enjoy the time with you in ETH.

My special thanks to PD Dr. Julia Boike for her trust and support. Her interest on my study extremely encourage me. We have lots of discussions and every time she unreservedly share her ideas and field data. Thanks to Prof. Grosse Guide for his host and support during my short visit in AWI. I really enjoy the collaboration with Prof. Guide and Dr. Frank Günther. My thanks also gives to the colleagues, Dr. Ingmar Nitze and Dr. Langer Moritz, in AWI.

I also would like to thank Prof. Tingjun Zhang. Dr. Bin Cao, Dr. Xiangqing Peng, Dr. Lili Li from Lanzhou University. Prof. Zhang supports me for field works in Tibet, which advanced my understanding on permafrost.

Thanks to the whole ISEIS families for their kindness and support: Dr. Peifeng Ma, Dr. Rui Zhang, Dr. Fan Zhang, Dr. Ming Zhang, Dr. Yulin Ding, Dr. Jing Wang, Dr. Gang Li, Dr. Yu Li, Dr. Na Dong, Dr. Zhen Liu, Dr. Weitao Che, Dr. Mingyuan Hu, Dr. Hongsheng Zhang Dr. Zhaocheng Zeng and Xianzhi Hu. I would like to thank our supporting staffs for their kindness and help, they are Isaac Chan, Carol Du, Wendy Wong, Kin Yeung, Chloris Yip. I would also like to thank the colleges from ESSC: Xiyu Chen, Lingcao Huang, Enze Zhang, Yan Hu, Jiahua Zhang. I greatly enjoy the CUHK time with all of you and the friendships with you are precious and unforgettable for me.

I would like to thank my friends Dr. Lei Zhang, Dr. Wenhao Wu, Dr. Xiaowen Wang, Chong Xu, Hao Zhang. They give me a lot of support and pleasure.

Finally, The endless and deepest thanks to my wife Yuzhen Cao. Without her support and encouragement, I cannot pass through my difficult time. Also special thanks to my parents, my sister for their continuous support during my life. Thanks for the born of my little daughter Yunyi Chen. She gives us a lot of pleasure.

Contents

Abstract **i**

Abstract **v**

Acknowledgments **vii**

List of acronyms **xi**

1 Introduction **1**

1.1 Scientific background 1

1.2 Research objectives 6

1.3 Roadmap of thesis 6

2 Surface elevation changes of permafrost environments and InSAR observations **9**

2.1 Permafrost thaw subsidence and its relevance 9

2.2 The principle of InSAR 14

2.3 Multi-temporal InSAR 18

3 Permafrost thaw subsidence in Eboling Mountain **27**

3.1 Introduction 27

3.2 Study site and field measurements 28

3.3 Results 39

3.4 Discussions 45

3.5 Summary 49

4 InSAR measurements of elevation changes over Yedoma upland 51

4.1 Introduction 51

4.2 Study site and field measurements 53

4.3 Results 59

4.4 Discussions 62

4.5 Summary 69

5 Permafrost degradation evidence from InSAR in Bayelva, Spitsbergen 71

5.1 Introduction 71

5.2 Study site 72

5.3 Data and methods 74

5.4 Preliminary results 77

5.5 Discussion 81

5.6 Summary and future work 83

6 Soil moisture impacts on InSAR permafrost studies 85

6.1 Introduction 85

6.2 Microwave dielectric properties of moist soil 86

6.3 Soil moisture impacts on InSAR observables 88

6.4 Soil moisture impacts on multi-temporal InSAR 91

6.5 Summary and future work 94

7 Conclusions and outlook 97

7.1 Conclusions 97

7.2 Outlook 99

Bibliography 101

List of acronyms

AD	Anderson-Darling
ADDT/F	Accumulated degree days of thaw/freeze
ALT	Active Layer Thickness
ASA	Actively Subsiding Area
ASF	Adaptive Spatial Filtering
CDC	Complex Dielectric Constant
DEM	Digital Elevation Model
DS	Distributed Scatterer
ECMWF	European Center for Medium-Range Weather Forecasts
GIAnT	Generic InSAR Analysis Toolbox
GPS	Global Positioning System
GPS-IR	GPS interferometric reflectometry
GPS-RTK	GPS Real Time Kinematic
HM-InSAR	Hybrid Multi-temporal InSAR
HRSC	High Resolution Stereo Camera
InSAR	Interferometric Synthetic Aperture Radar
ISCE	InSAR Scientific Computing Environment
KS	Kolmogorov-Smirnov
LOS	Line Of Sight
PL	Phase Linking
PS	Persistent Scatterer
PSC	Persistent Scatterer Candidate
PSI	Persistent Scatterer InSAR
QTP	Qinghai-Tibet Plateau
RCS	Radar Cross Section
RMS	Root Mean Square
SAR	Synthetic Aperture Radar
SB	Small Baseline
SBAS	Small Baseline Subset
SNR	Signal to Noise Ratio
SRDMM	Semi-empirical Refractive Dielectric Mixing Model
TOPS	Terrain Observation by Progressive Scans

List of Figures

2.1 Illustration of abrupt and gradual subsidence 10

2.2 Illustration of the conceptual permafrost thaw subsidence and uplift. (a) no permafrost thaw: the piece-wise line on the right indicates the cycling of seasonal thawing subsidence, freezing uplift and a stable period after the ground is totally frozen; the line with arrow shows no subsidence trends. (b) permafrost thaw: the seasonal elevation changes are the same to (a); The line with arrow shows an example of linear subsidence trends during each summer season. 11

2.3 Illustration of (a) persistent scatterer (PS) and (b) distributed scatterer (DS) in one resolution cell 17

3.1 Our study site and thermokarst features. (a) Google Earth image of our study site. The red polygon outlines the Eboling permafrost zone (same in all maps). The blue polygons outline the thermal erosion gullies. The red star shows the location of a ground temperature borehole. The red triangle marks the position of our InSAR reference point. The inset denotes the location of our study site (marked by the plus symbol) on the QTP. (b) A ground photo that shows the surficial features inside a thermal erosion gully. (c) A ground photo that shows massive ground ice exposed beneath the active layer within a thermal erosion gully. 29

3.2 Downscaled 2 m air temperature in the study area. 31

3.3 The flowchart of the PSI approach. PSs: Persistent Scatterers 34

3.4 The thaw subsidence and its uncertainty. (a) Map of linear subsidence trends from 2006 to 2011. Negative values mean subsidence. (b) Map of maximum seasonal subsidence. Negative values mean subsidence. (c) and (d) show the uncertainties of (a) and (b), respectively. 40

3.5 The spatial patterns of gradual thaw subsidence. (a) Map of 12 actively subsiding areas (ASAs, black polygons, numbered using the red digits) inside the Eboling permafrost zone. The blue polygons denote the boundaries of thermal erosion gullies. The time series of surface elevation changes at the crosses labeled as 'A' and 'B' are shown in Figure 3.6. (b) Same as Figure 4a but showing only the linear subsidence trends inside the ASAs. 41

3.6 Time series of the PSI-derived and modeled elevation changes at points A (a) and B (b), located inside and outside the actively subsiding areas, respectively. Their locations are marked in Figure 5a. 43

3.7 The comparison of the ALT-derived and the PSI-derived seasonal subsidence. The black bars show the confidence intervals. The differences between the two seasonal subsidence datasets are smaller than 2 cm within the two dashed lines. 44

3.8 The difference between the ALT-derived and the PSI-derived seasonal subsidence (former minus latter). 45

4.1 (**a**) Google Earth Image of Sobo-Sise Island. The red polygon outlines the island. The red crosses mark the four positions for which I present the results from InSAR time-series analysis. The three blue polygons are used to calibrate the InSAR measurements. The inset shows the location of Sobo-Sise Island in the southeastern Lena River Delta. (**b**) Elevation above the mean sea level over the Yedoma uplands and slopes. Thermokarst basins and water bodies are masked out. 55

4.2 The connections between 12 Sentinel-1A/B SAR images with the perpendicular and temporal baselines. 58

4.3 Surface elevation changes over the Yedoma uplands on Sobo-Sise Island from 23 June to 9 September in 2017. Minus values denote ground subsidence. 59

4.4 Box plot (minimum, first quartile, median, third quartile, maximum) for seasonal subsidence at different Yedoma elevations during the thaw season of 2017. 60

4.5 Averaged inter-annual elevation changes between the late thaw seasons of 2016 and 2017. 60

4.6 Inter-annual elevation changes between image pairs (**a**) 20160722–20170723 (**b**) 20160803–20170804; (**c**) 20160815–20170816; (**d**) 20160827–20170828; (**e**) 20160908–20170909 and (**f**) 20160926–20170921. 61

4.7 Time series of elevation changes based on our InSAR measurements at points (**a**) A; (**b**) B; (**c**) C; (**d**) D relative to the first acquisition on 22 July 2016. The error bars denote the uncertainty of the InSAR time series. The locations of the four points are shown in Figure 4.1. . . . 62

4.8 All the possible coherence maps for the thaw season of 2017. 67

4.9 Mean coherence over the Yedoma upland for all the 2017 interferograms. The legend symbols denote the months of the master images used to construct the interferograms. 68

4.10 Daily air temperature for the thaw season of 2016 (red) and 2017 (black). The six vertical solid lines denote the dates of the inter-annual SAR acquisition pairs. 68

5.1 Aerial image captured in August 2008. The time-series of surface elevation changes at the red crosses labeled as 'airport building', 'polar institute', and 'mass hall' are shown in Figure 5.6. The red star marks the location of Bayelva observation site. 73

5.2 The flowchart of multi-temporal InSAR approach 75

5.3 Baseline networking of (a) ERS-2; (b) Sentinel-1A and -1B 76

5.4 (a) Accumulated ground subsidence between 1995-06-18 and 2009-07-19; (b) The uncertainty of accumulated subsidence. Negative value means ground subsidence. 78

5.5 InSAR subsidence time-series of (a) ERS between 1995-06-18 and 2009-07-19; (b) Sentinel-1 between 2015-08-02 and 2018-09-21. 79

5.6 Sentinel-1 subsidence time-series of (a) the building of polar institute (latitude: 78.923283° , longitude: 11.929776°); (b) the mass hall (78.923732 ° , 11.933765°); (c) a building in the airport (78.929705° , 11.863437°) during 2015-2018. The position of the three buildings are marked out by the red crosses in Figure 5.1 80

5.7 (a) Yearly averaged soil moisture; (b) Yearly averaged soil temperature in the active layer at different depth in Bayelva site. 82

5.8 Ground photo of soil stratigraphy taken from (a) 1999; (b) 2018 by Dr. Julia Boike (AWI). 82

6.1 Modeled relative permittivity and loss factor by using Mironov's temperature-dependent SRDMM (Mironov et al., 2017) 88

6.2 Simulated interferometric phase (in degrees) and coherence. 90

6.3 Phase triplets calculated from real Sentinel-1 interferogram stacks in Lena Delta, Siberia. The number under each sub-figure denotes the acquisition times (YYYYMMDD) of the three images. 91

6.4 InSAR time-series calibration by compensating the simulated soil moisture phase. SBAS-based correction and raw InSAR time-series shows a noticeable bias within the two free red cycles which is mainly occurred during the freezing stage of 2017 and 2018. 94

List of Tables

3.1 List of interferograms generated in the PSI processing. Common master image was acquired on 14 December 2009. 35

3.2 The area and average subsidence trends inside the actively subsiding areas (ASAs). 42

4.1 The acquisition date and platform of SAR images used in this study. 57

Chapter 1

Introduction

1.1 Scientific background

1.1.1 Thawing and degrading permafrost

Permafrost, or permanently frozen ground, is found on about 24 % (22.8 million square kilometers) of the exposed land surface of the northern hemisphere (Zhang et al., 2008) and defined solely by a temperature below 0 °C, which has been continuously present for at least two years (van Everdingen, 1998). The layer above permafrost which thaws in summer and freeze in winter is called active layer. The extent of permafrost occurs mostly in Alaska, Siberia, northern Canada, and Greenland at high latitude. Permafrost at lower latitude mainly occurs in high elevation areas, such as Qinghai-Tibetan Plateau, European Alps, the Mountains of North America and the Andes. The thickness of permafrost varies from less than 1 meter to greater than 1,000 meters.

Under ongoing climatic warming and extreme weather, permafrost is extremely vulnerable to thawing and degrading. It has been observed that permafrost is warming in a global scale associated with the rising air temperature and/or the increasing snow depth (Biskaborn et al., 2019). Permafrost is a large organic carbon reservoir that is very sensitive to the warming climate. The total soil carbon deposited in permafrost is about 1700 Pg (1 Pg = 1 billion metric tons), which is more than twice the total soil carbon storage in the atmosphere (Zimov et al., 2006; Schuur et al., 2008).

The thawing permafrost makes a large amount of frozen soil carbon vulnerable to microbial breakdown, which consequently contributes to climatic warming through positive feedback (Koven et al., 2011; MacDougall et al., 2012; Schuur et al., 2015; Schadel et al., 2016). The permafrost thaw processes also interact with the local hydrological condition (O'Donnell et al., 2012; Liljedahl et al., 2016; Walvoord and Kurylyk, 2016), the ecosystems (Osterkamp et al., 2000; Jorgenson and Osterkamp, 2005; Nauta et al., 2015; Vonk et al., 2015), and the geomorphological processes (Grosse et al., 2011; Lantuit et al., 2013).

In addition, thawing and degrading permafrost is threatening the infrastructure (such as buildings, roads and railways, airports, and pipelines etc.) (Nelson et al., 2001; Instanes, 2003; Streletskiy et al., 2012). The infrastructure damage is unprecedentedly challenging the local economic and social sustainability, climate migration and adaptation, and human well-being. Considerable efforts have been devoted to conducting the hazards maps by feeding the current and projection of permafrost degradation and consequently assessing the risks of Arctic infrastructure (Nelson et al., 2001; Shiklomanov et al., 2017; Hjort et al., 2018). Based on these up-down climatic impact models, researchers predict that 70% of pan-Arctic infrastructures are vulnerable to thaw-related damage and 3.6 million people may be affected by 2050 (Hjort et al., 2018). The estimated economic cost will reach up to 4.2-5.5 billion USD by 2100 in Alaska (Melvin et al., 2017), and around 80 billion USD by 2050 in Russia (Streletskiy et al., 2019). But, the infrastructure instabilities in permafrost regions are limited known.

One major distinctive indicator of permafrost degradation is the development of thermokarst landforms (Kokelj and Jorgenson, 2013). Thermokarst is a process that characterizes landforms caused by the thawing of ice-rich permafrost or the melting of massive ice (van Everdingen, 1998). Thermokarst processes are associated with

local or widespread collapse, and instability of the ground surface, together with surface subsidence (French, 2007). The dynamic processes between the active layer and underlying ice-rich permafrost further affect soil moisture content and vegetation growth, leading to changes in ground thermal regime and the energy exchanges between the land surface and the atmosphere (Shiklomanov et al., 2010). These interactions potentially provide further feedback to surface elevation changes.

In regions underlain by permafrost, thaw subsidence can be gradual or abrupt. Whether thaw subsidence is gradual or abrupt is related to the patterns and timing of movement of surficial unconsolidated material due to the thawing of the active layer and the ice-rich permafrost. Here I define gradual thaw subsidence as being the small and continuous lowering of the ground surface that spans periods from several years to decades. Gradual thaw subsidence is continuous both in time and space, and therefore the ground surface remains intact without forming thermokarst landforms. Abrupt thaw subsidence refers to the sudden or rapid lowering of the ground surface within a few hours, days, or months. The abrupt thaw subsidence is more likely to be discrete both in time and space, and it results in irregular thermokarst topography. In general, both gradual and abrupt thaw subsidence occurs in thermokarst processes (for instance, retrogressive thaw slump, thermal erosion gully, and shoreline erosion etc.).

However, permafrost thaw subsidence both in Arctic and on the QTP is still poorly quantified or understood.

1.1.2 Geodesy and remote sensing

Since the 1970s, field-based methods have been applied to measure the gradual thaw subsidence in permafrost regions. Frost tube or heavemeter, an instrument used to measure the depth and timing of the freezing, is designed and installed to observe the

frost heave within the active layer during the freeze season (Mackay, 1973a, 1983). Repeat leveling surveys are conducted to measure the gradual thaw subsidence and frost heave, against benchmarks (such as steel pipes) anchored into permafrost (Mackay, 1973b, 1983; Mackay and Burn, 2002). Since the 2000s, the differential Global Positing System (GPS) has been used to measure the elevation changes in permafrost regions at different time scales (Little et al., 2003; Shiklomanov et al., 2013; Streletskiy et al., 2017). The terrestrial laser scanning is a new field-based method mostly used to monitor the slope instability related to permafrost degradation (Luo et al., 2017). More recently, GPS interferometric reflectometry (GPS-IR) has been firstly used to measure the decadal seasonal subsidence and uplift over permafrost regions (Liu and Larson, 2018; Hu et al., 2018). All the aforementioned field-based methods have accuracies of centimeters or better. However, these site-specific measurements offer limited spatial coverage or few repeat observations, and therefore hardly reveal the spatial dynamics of gradual thaw subsidence. Furthermore, some of these methods are intrusive and may disturb the local permafrost conditions in the first few years after the installation. Even worse, scientists may lost their equipment due to the abrupt permafrost thawing under climatic warming.

Recently, space- and air-borne remote sensing techniques have been utilized to measure permafrost thaw subsidence. Differential digital elevation models (DEMs) generated from stereographic images have been successfully used to measure the permafrost thaw subsidence (Kääb, 2002; Lantuit and Pollard, 2005; Günther et al., 2015). Repeat air-borne LiDAR has observed the ground elevation change due to permafrost thawing (Jones et al., 2013, 2015; Obu et al., 2017). Single-pass space-borne radar interferometry (InSAR) are also used to observe the elevation changes of thaw slumps (Zwieback et al., 2018). Because the DEM intervals are typically one year or longer and the subsidence accuracy of DEM differencing is in sub-meters, this method effec-

tively detects only the large, abrupt subsidence.

Repeat-pass InSAR has been used to map and quantify gradual permafrost thaw subsidence during recent years. For instance, Short et al. (2011, 2014) observed the seasonal thaw subsidence within one year by the interferogram stacking methods. Liu et al. (2010, 2015) mapped and quantified permafrost thaw subsidence based on a multi-looked small baseline subset (SBAS) approach in Alaska. Daout et al. (2017) detected both seasonal thaw subsidence and freeze uplift over extensive regions in northwestern Tibet. However, these multi-temporal InSAR studies used a few and limited SAR acquisitions, and hence suffered from poor temporal sampling. Therefore, these measurements are vulnerable to measurement noises and any deficiencies in the assumed time series model. These studies also applied spatial averaging and reduced the original spatial resolution of SAR images. Persistent Scatterer Interferometric Synthetic Aperture Radar (PSI) is an advanced pixel-specific InSAR time series technique with the usage of all repeat SAR acquisitions because it is less affected by temporal or geometric decorrelation and has millimeter to submillimeter accuracy (Ferretti et al., 2001, 2007; Hooper et al., 2004). There are also advanced hybrid multi-temporal InSAR (HM-InSAR) approaches with the aim to take the essence from both SBAS and PSI (Ferretti et al., 2011; Fornaro et al., 2012). PSI and HM-InSAR approaches have been widely used to measure the ground subsidence associated with buildings and infrastructures in urban environments (Crosetto et al., 2015; Gernhardt et al., 2010), groundwater withdrawal (Bell et al., 2008; Colesanti et al., 2003a), volcano dynamics (Hooper et al., 2004, 2012), and landslides (Ciampalini et al., 2016; Colesanti et al., 2003b; Hilley et al., 2004). But, there are limited studies to exploit the application of these approaches in permafrost regions.

1.2 Research objectives

Permafrost thaw subsidence both in Arctic and on the QTP is still poorly quantified or understood. Thus, the specific objectives of this thesis are:

1. To develop an advanced persistent scatterer InSAR approach for mapping and quantifying fine-scale thermokarst subsidence.

2. To exploit the capability of Sentinel-1 InSAR measurements for quantifying permafrost thaw subsidence.

3. To evaluate the permafrost degradation as well as building risks from long-term InSAR and ground measurements.

4. To illustrate the effects of soil moisture associated with freezing and thawing on InSAR measurements.

1.3 Roadmap of thesis

The thesis is organized as follows:

Chapter 1 is the general introduction for the scientific background and research objectives. The principle of permafrost thaw subsidence and InSAR and multi-temporal InSAR techniques are introduced in **Chapter 2**.

In **Chapter 3**, the persistent scatterer InSAR (PSI) is used to remotely measure gradual surface subsidence on Eboling Mountain in the northeastern region of the Qinghai-Tibet Plateau, where thermal erosion gullies are well developed. In the PSI analysis, a piecewise elevation change model that includes periodic subsidence/uplift because of its seasonally varying components as well as its linear subsidence trends is introduced to capture the dynamic processes of the active layer and the underlying

permafrost. Ground surface subsidence, ranging from 0.3 cm/year to 3 cm/year, occurred both inside the visible thermal erosion gullies and their surroundings.

In **Chapter 4**, I use C-band Sentinel-1 InSAR measurements to map the elevation changes over ice-rich Yedoma uplands on Sobo-Sise Island, Lena Delta with frequent revisit observations (as short as six or twelve days). Significant seasonal thaw subsidence during summer months and heterogeneous inter-annual elevation changes are observed during 2016–17. Interesting patterns of stronger seasonal thaw subsidence on elevated flat Yedoma uplands is also observed by comparing to the surrounding Yedoma slopes.

In **Chapter 5**, the long-term thaw subsidence both from the permafrost ground surface and the above infrastructures during the past three decades (1998-2018) are quantified in Bayelva, Spitsbergen. To isolate the persistent scatterers and meanwhile mitigate the resolution loss, an advanced hybrid multi-temporal InSAR approach is introduced. Consistent with InSAR measurements, permafrost degradation evidence, such as increase of active layer thickness and permafrost temperature, is also found from the field measurements.

In **Chapter 6**, soil moisture impacts on InSAR observables and multi-temporal InSAR approaches are illustrated. I found that it is very likely that the two signals from soil moisture and real ground elevation changes are superimposed in the InSAR-derived subsidence time-series. Since this phenomena is very common in permafrost regions, this explanation would challenge all the InSAR-based permafrost subsidence studies.

Chapter 7 are the conclusions and outlooks for future study.

Chapter 2

Surface elevation changes of permafrost and InSAR observations

2.1 Permafrost thaw subsidence and its relevance

In regions underlain by permafrost, thaw subsidence can be gradual or abrupt (Figure 2.1). Whether thaw subsidence is gradual or abrupt is related to the patterns and timing of movement of surficial unconsolidated material due to the thawing of the active layer and the ice-rich permafrost. Here I define gradual thaw subsidence as being the small and continuous lowering of the ground surface that spans periods from several years to decades. Gradual thaw subsidence is continuous both in time and space, and therefore the ground surface remains intact without forming thermokarst landforms. Abrupt thaw subsidence refers to the sudden or rapid lowering of the ground surface within a few hours, days, or months. The abrupt thaw subsidence is more likely to be discrete both in time and space, and it results in irregular thermokarst topography. In general, both gradual and abrupt thaw subsidence occurs in thermokarst processes (for instance, retrogressive thaw slump, thermal erosion gully, and shoreline erosion, etc.). While it is relatively easier to identify landforms associated with abrupt thaw subsidence in the field or from optical remote sensing images, detecting the gradual thaw subsidence requires repeat and accurate measurements.

Gradual elevation change (subsidence/uplift) is dominantly associated with the freez-

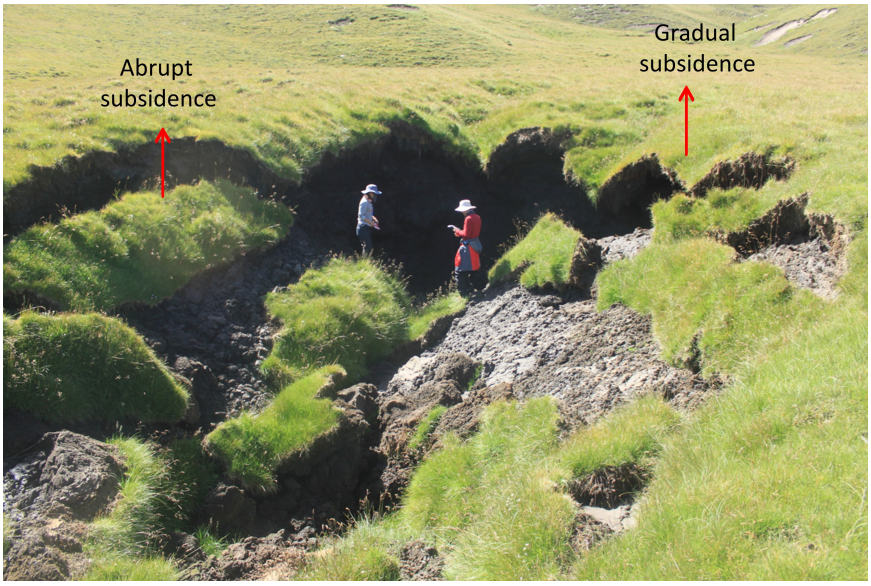

Figure 2.1 Illustration of abrupt and gradual subsidence

ing and thawing of the active layer and the uppermost permafrost (Figure 2.2). The ground subsides seasonally in association with the thawing and volumetric contraction of the active layer due to the phase transition of the frozen soil to a liquid state in summer. Conversely, in winter ground uplift occurs in association with the freezing and volumetric expansion of the active layer due to the phase transition of the unfrozen soil to a frozen state. As soon as the freezing processes stop, the ground surface remains stable until the onset of the next thaw season. Under warming or disturbance, the volumetric ice content may exceed the total soil pore volume in freezing season, forming excess ground ice (van Everdingen, 1998). If the excess meltwater upon thawing in the uppermost permafrost layer is well drained, the ground experiences additional gradual thaw subsidence. Otherwise, the excess meltwater may pool up and subsequently trigger the formation of thermokarst landforms.

Starting from one-dimensional Fourier's non-stationary heat conduction equation

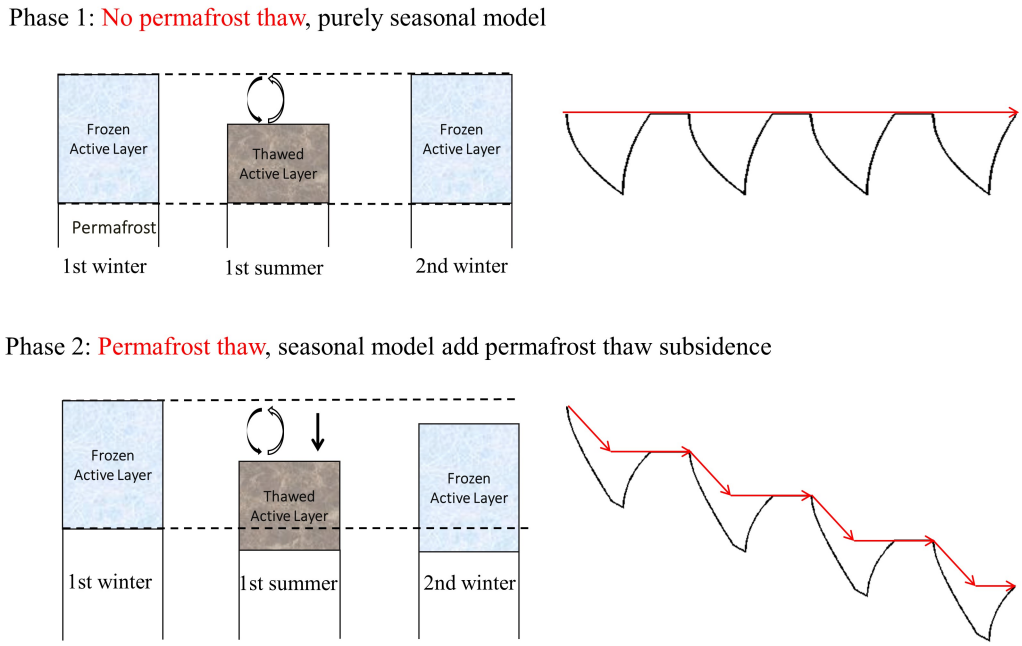

Figure 2.2 Illustration of the conceptual permafrost thaw subsidence and uplift. (a) no permafrost thaw: the piece-wise line on the right indicates the cycling of seasonal thawing subsidence, freezing uplift and a stable period after the ground is totally frozen; the line with arrow shows no subsidence trends. (b) permafrost thaw: the seasonal elevation changes are the same to (a); The line with arrow shows an example of linear subsidence trends during each summer season.

without considering soil freezing and thawing (Yershov, 1998):

$$C_{vol}(z)\frac{\partial T}{\partial \tau} = \frac{\partial}{\partial z}(k(z)\frac{\partial T}{\partial z}) + f(z) \tag{2.1}$$

To keep fluent, I define all the symbols of this section at the end of this section. Assume that the heat source or sink is zero which means no lateral heat transfer in time and depth ($f(z) = 0$) and the soil density does not change with time and depth ($\rho = const$, homogeneous soil). The heat conduction equation becomes:

$$\frac{\partial T}{\partial \tau} = \frac{k}{C\rho}\frac{\partial^2 T}{\partial z^2} = \kappa\frac{\partial^2 T}{\partial z^2} \tag{2.2}$$

Regarding for the soil freezing (thawing) processes, the freezing boundary or front is simply defined as the zero isotherm. The specific heat capacity C is replaced by the latent heat used for phase transition $l\,(\approx 3.34e5\,J\mathrm{kg}^{-1})$ and the soil water/ice content θ in the phase transition layer. Stefan condition at the freezing boundary is (Yershov, 1998):

$$\begin{aligned}
&\frac{\partial T_{fro}(z,\tau)}{\partial \tau} = \frac{k_{fro}}{\theta l \rho}\frac{\partial^2 T_{fro}(z,\tau)}{\partial z^2} \qquad 0 < z < \xi(\tau);\ t > 0 \\
&\frac{\partial T_{unf}(z,\tau)}{\partial \tau} = \frac{k_{unf}}{\theta l \rho}\frac{\partial^2 T_{unf}(z,\tau)}{\partial z^2} \qquad \xi(\tau) < z < u;\ t > 0 \\
&T_{fro}(\xi(\tau),\tau) = T_{unf}(\xi(\tau),\tau) = T_{fre} \\
&k_{fro}\frac{\partial T_{fro}}{\partial z}|_{z=\xi-0} - k_{unf}\frac{\partial T_{unf}}{\partial z}|_{z=\xi+0} = \theta l \rho \frac{d\xi(\tau)}{d\tau}
\end{aligned} \tag{2.3}$$

The underlying assumptions are that the freezing temperature is a fixed value (0 °C) and the moisture migration from frozen to unfrozen zone is ignored. The approximate solution used for calculating the thawing depth under the Stefan condition, i.e. the Stefan formula, is:

$$\begin{aligned}
&k_{fro}\frac{\partial T_{fro}}{\partial z}|_{z=\xi(\tau)} - k_{unf}\frac{\partial T_{unf}}{\partial z}|_{z=\xi(\tau)} = \theta l \rho \frac{d\xi(\tau)}{d\partial\tau} \\
&where \qquad \frac{\partial T_{unf}}{\partial z} = 0 \\
&\Rightarrow \xi_{fro}(\tau) = \sqrt{\frac{2k_{fro}T\tau}{\theta l \rho}} = \sqrt{\frac{2k_{fro}}{\theta l \rho}}\sqrt{A_{fro}}
\end{aligned} \tag{2.4}$$

Considering the zero curtain effects, the moving freeze depth becomes:

$$\xi_f(\tau) = \sqrt{\frac{2n_f k_f}{\theta l \rho}}\sqrt{A_f(T,\tau)} \tag{2.5}$$

Similarly, the moving thaw depth is:

$$\xi_t(\tau) = \sqrt{\frac{2n_t k_t}{\theta l \rho}} \sqrt{A_t(T, \tau)} \tag{2.6}$$

The active layer thickness (ALT) is the maximum thaw depth:

$$\xi_{ALT} = \sqrt{\frac{2n_t k_t}{\theta l \rho}} \sqrt{A_{max}} \tag{2.7}$$

For fully saturated frozen active layer, the maximum seasonal thaw subsidence due to the phase transition from pore water to pore ice is expressed as (Liu et al., 2012):

$$d = \int_0^{\xi} \theta(\xi) \frac{\rho_w - \rho_i}{\rho_i} d\xi \tag{2.8}$$

Note that the soil moisture content is the specific value in the phase transition layer, which generally fully saturated due to the water migration. To simplify of the model, soil moisture content is assumed as a constant with depth. Another assumption is that the seasonal thaw depth is equal to the freeze depth, which is equivalent to the seasonal subsidence and uplift are equal. Equation 2.5, 2.6, and the differential form of Equation 2.8 at any given time during thawing stage reads:

$$\begin{aligned} d_t(\tau) &= \frac{\rho_w - \rho_i}{\rho_i} \sqrt{\frac{2\theta n_t k_t}{l\rho}} \sqrt{A_t} \\ d_f(\tau) &= \frac{\rho_w - \rho_i}{\rho_i} \sqrt{\frac{2\theta n_f k_f}{l\rho}} \sqrt{A_f} \end{aligned} \tag{2.9}$$

The net ground subsidence is:

$$\begin{aligned} d(\tau) &= d_t(\tau) - d_f(\tau) \\ &= \frac{\rho_w - \rho_i}{\rho_i} \sqrt{\frac{2\theta}{l\rho}} \sqrt{n_t k_t} (\sqrt{A_t} - \sqrt{\frac{n_f k_f}{n_t k_t}} \sqrt{A_f}) \end{aligned} \tag{2.10}$$

Introduce a composite index to account for both thawing and freezing (Hu et al., 2018):

$$I(\tau) = \sqrt{A_t(\tau)} - \sqrt{\frac{n_f k_f}{n_t k_t}}\sqrt{A_f(\tau)} \tag{2.11}$$

To calculate the accumulated seasonal thaw subsidence or freeze uplift, the subsidence and composite index are normalized by their maximum values:

$$d(\tau) = \frac{d_{max}}{I_{max}} I(\tau) + \epsilon \tag{2.12}$$

ϵ is the random noise.

Symbols

T	The air temperature (units: K)
τ	Time (units: s)
z	Soil depth (units: m)
$\xi_{f/t}$	Freezing or thawing depth (units: m)
k	Soil thermal conductivity (units: $W\,m^{-1}\,K^{-1}$)
C	Specific heat capacity (units: $J\,\mathrm{kg}^{-1}\,K^{-1}$)
ρ	Soil bulk density (units: $\mathrm{kg}\,m^{-3}$)
f	Heat source or sink
l	Latent heat of fusion (units: $J\,\mathrm{kg}^{-1}$)
$A_{f/t}$	Accumulated degree days of freezing/thawing (units: day °C)
q	Heat flux or heat flux density (units: Wm^{-2})
Q_{ph}	The amount of heat released or absorbed with respect to complete freezing or thawing of the moist soil (units: Jm^{-3})

2.2 The principle of InSAR

The basic principle of InSAR is to compare the phase of two complex SAR signals acquired from slightly different positions at different time. In general, the interfer-

ometric phase is modeled as a linear mixture of Light of Sight (LOS) displacement (ϕ_{disp}), flat-earth phase ϕ_{flat}, topographic phase (ϕ_{topo}), atmospheric phase (both ionospheric and tropospheric disturbance, ϕ_{atm}), and thermal noise (ϵ). Such first-order linear interferometric phase model reads (Bamler and Hartl, 1998; Hanssen, 2001):

$$\phi = \phi_{disp} + \phi_{flat} + \phi_{topo} + \phi_{atm} + \epsilon \tag{2.13}$$

The displacement phase refers to the projection of the movement of ground surface onto the LOS direction during the two SAR acquisition times. The flat-earth phase refers to the phase fringe in range direction generated by a flat earth against an ellipsoidal reference, whereas its amplitude depends on the sensor-target geometry. The topographic phase refers to the phase generated by the height of the ground target above the reference surface. The atmospheric phase mainly refers to the different phase delay due to the tropospheric and/or ionospheric disturbance during the two SAR acquisition times (Hanssen, 2001). In principle, the thermal noise is only determined by the signal-to-noise-ratio (SNR) of the signal transmitter and receiver of radar system. But here, the thermal noise also includes the effects from the response of ground target in terms of backscatter coefficient (or normalized Radar Cross Section, RCS), which is mainly determined by target roughness, mixture dielectric constant, and local incident angle. More details about the principle and practice of InSAR can be found from Bamler and Hartl (1998); Hanssen (2001).

Recently, De Zan et al. (2014) and Zwieback et al. (2015a) proposed a first-order interferometric model to isolate the soil moisture effects. The complex interferogram between two acquisitions m and n could be expressed as an integral:

$$I(k_{z,m}, k_{z,n}) = \int_0^\infty f(z) e^{-jk_{z,m}z} (e^{-jk_{z,n}z})^* dz \tag{2.14}$$

where k is the vertical wavenumber and $f(z)$ is the vertical scattering profile. By assuming that the vertical scattering profile is uniform within the soil medium, the interferometric phase can be expressed as:

$$\phi = \arg(\frac{1}{2j(k_z^m - (k_z^s)^*)}) \tag{2.15}$$

The interferometric model described in Equation 2.13 only considered the propagation of radar waves in air and assumed that the wavenumber in air is a constant ($k_{air} = 2\pi/\lambda$). However, the radar wave may penetrate into the soil medium, where the wavenumber in soil is highly dependent on the complex dielectric constant of moist soil and thus magnitude of soil moisture content. Note that different from the linear phase components, the soil moisture phase is highly nonlinear.

The complex backscattered signal of each SAR resolution cell is the integration of all the scatterers within the cell. The signal strongly depends on the backscatter coefficient, which relates to the SAR geometry and the ground nature. The SAR pixel is statistically dominated scatterer (or persistent scatterer, point scatter, PS) if the resolution cell is dominant by one ground target, or distributed scatterer (DS) if no dominant signal emerge (Figure 2.3) (Bamler and Hartl, 1998).

The coherence between two SAR images quantifies the similarity of the scattering coefficients. The degree of coherence (γ) between two SAR images s_1 and s_2 can be expressed by a complex correlation function:

$$\gamma = \frac{E[s_1 s_2^*]}{\sqrt{E[|s_1|^2]E[|s_2|^2]}} = |\gamma| e^{j\phi} \tag{2.16}$$

where $E[]$ means the expectation value and * is the complex conjugate. The changes of surface conditions and sensor-target geometry result in different scattering coef-

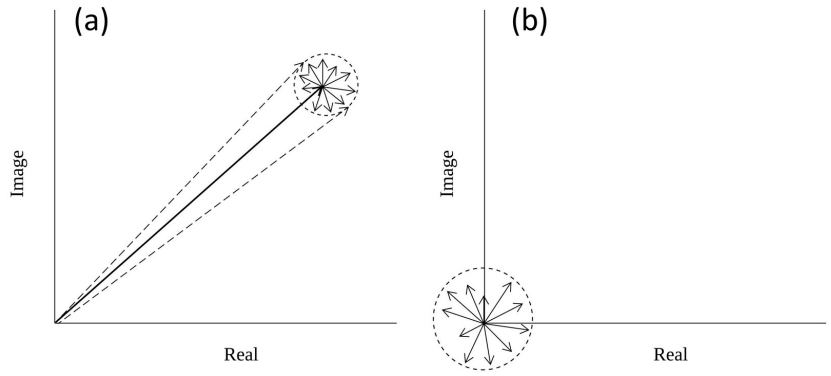

Figure 2.3 Illustration of (a) persistent scatterer (PS) and (b) distributed scatterer (DS) in one resolution cell

ficients and subsequently decorrelation. The magnitude of the complex coherence, ranging from 0 to 1 (0: totally decorrelation; 1: noise-free coherent signal), is used as a measure of the accuracy of the interferometric phase. In general, the total decorrelation between two SAR images can be decomposed into: spatial decorrelation ($\gamma_{spatial}$), caused by the changes of incident angles; Doppler centroid decorrelation, caused the changes of Doppler centroids ($\gamma_{doppler}$); volumetric decorrelation (γ_{vol}), caused by volumetric scattering whereas radar wave penetrating into a volume of targets (such as high vegetation cover, snow cover et al.); temporal decorrelation ($\gamma_{temporal}$), caused by physical changes in the ground surface; and thermal noise ($\gamma_{thermal}$) and be expressed as (Zebker and Villasenor, 1992; Bamler and Just, 1993; Hanssen, 2001):

$$\gamma_{total} = \gamma_{spatial} \cdot \gamma_{doppler} \cdot \gamma_{vol} \cdot \gamma_{temporal} \cdot \gamma_{thermal} \tag{2.17}$$

By migrating or ignoring the other components in Equation 2.13, InSAR can be used to observe ground surface movement or topography. However, there is no effective way to remove the atmospheric phase delay in terms of only one single interferogram, especially when the ground subsidence is gradual. This is mainly because atmospheric

phase delay and ground subsidence are both on the order of millimeters to centimeters and spatially correlated. In addition, severe geometric (such as large spatial baseline) or temporal (such as thawing and freezing, vegetation succession, soil moisture variation) decorrelation further lowers the accuracy of InSAR measurement and challenges the applicability of InSAR.

2.3 Multi-temporal InSAR

To overcome the aforementioned interferometric decorrelation and atmospheric artifacts, multi-temporal InSAR approaches have emerged since late 1990s (Zebker et al., 1997; Sandwell and Price, 1998; Ferretti et al., 1999a,b). The principle of the multi-temporal InSAR is to isolate the moderate and/or high coherent ground target in temporal and mitigate the atmospheric phase delay. Aiming to observe different ground targets (such as infrastructures, bare soil, volcanic dynamics, slope movements) in more spatial and temporal detail, the concepts of multi-temporal InSAR can be roughly categorized as single-master-based persistent scatterer InSAR (PSI), multi-master-based small baseline subset InSAR (SBAS), and hybrid methods. The conventional PSI only deals with the discrete targets (only acts as PSs) from single-master interferograms, while the conventional SBAS only deals with the discrete targets (only acts as DSs) from small-baseline-based multiple-master interferograms. The hybrid multi-temporal InSAR (HM-InSAR) approaches refer to dealing with PSs and DSs together. As there is no uniform concept for the hybrid approaches, some researchers still use PSI and SBAS to represent the hybrid approaches by integrating PSs and DSs. In this way, the concepts of PSI and SBAS becomes more likely different data processing strategies, i.e. how to construct the interferogram pairs (single or multiple master). In this section, I will introduce the main steps of the conventional

PSI and SBAS. More details about their implementation can be found: PSI (Ferretti et al., 2001; Colesanti et al., 2003a; Hooper et al., 2004), SBAS (Berardino et al., 2002; Lanari et al., 2004; Lauknes et al., 2011), HM-InSAR (Guarnieri and Tebaldini, 2008; Ferretti et al., 2011; Goel and Adam, 2012).

2.3.1 Persistent scatterer radar interferometry (PSI)

In practice, a persistent scatterer (PS) refers to a stable natural or man-made target that exhibits a consistent phase behavior over time (Ferretti et al., 2001; Hooper et al., 2004). The PSI technique estimates the surface elevation changes through time series by analyzing the differential interferometric phase of discrete targets (only acts as PSs) from repeat SAR images (Colesanti et al., 2003a; Ferretti et al., 2001). The main steps of PSI approach contain PS selection, phase unwrapping and decomposition, and atmospheric phase migration.

Essentially, PS refers to the resolution cell whose phase is stable in time. However, the initial phase is a mixture of several components (see Equation 2.13) and thus cannot be used to estimate the phase stability. Based on that the phase noise approximately follows the Gaussian distribution, Ferretti et al. (2001) found that if the signal-to-noise ratio of a pixel is high, the pixel-specific amplitude dispersion can serve as a proxy for phase standard deviation (σ_ϕ) in time domain. The amplitude dispersion is defined as the ratio of the standard deviation of the amplitude variation (σ_A) over its mean (μ_A).

$$D_A = \frac{\sigma_A}{\mu_A} \approx \sigma_\phi \tag{2.18}$$

There are also some similar amplitude-based approaches, such as mean amplitude index (Adam et al., 2004). Amplitude-based approaches perform well for the ground targets with strong backscattered power, such as man-made buildings and infrastruc-

tures. There are also phase-based approaches by specifically assuming a spatial phase model (Hooper et al., 2004). The aim of the phase-based approach is to detect the ground target with less strong power but still high SNR.

It should be noted that in practice the approaches mentioned above are used to select PS candidates. After phase unwrapping and decomposition (i.e., the separation of different phase components), the magnitude of temporal ensemble coherence is commonly used to detect the final stable PSs among the PS candidates. Given $N+1$ SAR images, the temporal ensemble coherence is defined by the summation of the averaged phase residuals (ϕ_{res}) after subtracting the modeled phase (i.e., the displacement and topographic phase) in time domain.

$$\gamma_{ens} = \frac{1}{N}\sum_{i=1}^{N}\exp(j\phi_{res}) \tag{2.19}$$

The magnitude of ensemble coherence ranges from 0 to 1, whereas a higher value means a stable PS.

All the interferogram stacks here is wrapped by 2π due to the nature of electromagnetic waves. Compared with other ground targets, PS are less sensitive to the temporal or geometrical decorrelation and thus have gradual ground movements, constant topographic height and low thermal noise. Moreover, the atmospheric effect are assumed to be spatially correlated within a certain distance (e.g. smaller than 2 km (Colesanti et al., 2003a)) but not correlated in time in terms of the operational SAR revisit time (days or months). The initial topographic phase can be easily compensated by using external DEM. The atmospheric effects are considered constant between two nearby PSs and random in time domain. Thus, the basic observation of

PSI becomes the phase difference between two nearby PSs:

$$_{\Delta}\phi_i = k_{air\Delta}d_i + \frac{2B_{\perp}}{rsin\theta}k_{air\Delta}h_i + {}_{\Delta}\phi_{atm,i} + {}_{\Delta}\epsilon_i \tag{2.20}$$

where $B_{\perp}$ is the perpendicular spatial baseline, θ is the incidence angle, $_{\Delta}d$ and $_{\Delta}h$ are the relative displacement and topographic residual between two nearby PSs, respectively. To solve equation 2.20, the temporal displacement should be predefined, such as by a linear model (Ferretti et al., 2001) or linear plus seasonal model (Colesanti et al., 2003a). By assuming that $|_{\Delta}\epsilon_i| < \pi$, the problem can be considered as a nonlinear complex inversion problem that can be solved by discretely sampled periodogram (Ferretti et al., 2001), or integer least squares (Kampes and Hanssen, 2004). By constructing global network among all PSs, the two-dimensional spatial phase unwrapping approaches (e.g., simple least squares, minimum cost network flow approach (Costantini, 1998; Chen, 2001)) are commonly used to retrieve the global solution, i.e., the modeled displacement and/or the topographic residual.

In general, the migration of atmospheric phase is an optional process and highly dependent on the real atmospheric conditions. The split-spectrum method is commonly used to mitigate the strong ionospheric effects at the expense of spatial resolution (Gomba et al., 2016; Fattahi et al., 2017). The strong tropospheric effect is commonly mitigated by spatial-temporal filtering (Ferretti et al., 2001) and/or additional tropospheric model (Yu et al., 2018). However, it should be noted that all the migration processes may also introduce additional error due to certain correlation between atmospheric and ground displacement, especially in the case when atmospheric artifacts are comparable to the ground displacement.

It also should be noted that a predefined phase model is needed in all PSI approaches. The retrieval of phase stabilities in time domain, no matter amplitude-based or phase-

based approaches, is highly dependent on the predefined phase model. An imperfect phase model may introduce additional systemic error and thus make the ensemble coherence fail to detect the PS targets.

2.3.2 Small baseline subset radar interferometry (SBAS)

The SBAS approach is based on an optimal combination of small-baseline (SB) interferograms by selecting image pairs with small temporal and spatial baselines, which are therefore less affected by neither geometric or temporal decorrelation (Berardino et al., 2002). In this case, the phase component in terms of topographic residual is relatively small and can be treated as random in time. Another key idea in SBAS is the spatial complex multilooking, i.e., averaging a number of complex pixels within a boxcar window no matter PSs or DSs, to improve phase statistics at the cost of spatial resolution and loss of PSs. Note that the spatial multilooking is based on the assumption that the pixels within the boxcar window are statistically homogeneous. The improved phase statistics could detect more natural targets especially in non-urban regions. Lanari et al. (2004) proposed a full-resolution SBAS approach by combining the multilooked and single-look SB interferograms. But as the DSs are characterized with low or moderate coherence, the accuracy of DSs without multilooking may be low.

It should be noted that different from PSI, the feeding data in SBAS is the spatial-unwrapped SB interferograms. To take full usage of all the SAR images, each image should be connected with at least one other image. Given $N+1$ SAR images, the number of SB interferograms (M) satisfies:

$$\frac{N+1}{2} \leq M \leq \frac{N(N+1)}{2} \tag{2.21}$$

Thus, the SB interferograms ($\phi_{m,n}$) can be expressed by phase time-series relative to the specific master image (s):

$$\phi_{m,n} = \phi_{s,m} - \phi_{s,n} \qquad \forall m, n = 1, ..., N+1 \tag{2.22}$$

For each pixel, let $\phi^T = [\phi_1, ..., \phi_M]$ be the vector of M SB interferometric phases and $\varphi^T = [\varphi_1, ..., \varphi_N]$ be the vector of the N equivalent single-master phases:

$$\underset{M\times 1}{\phi_{\mathrm{T}}} = \underset{M\times N}{\mathrm{B}} \underset{N\times 1}{\varphi_{\mathrm{T}}} \tag{2.23}$$

where B is the linear design matrix related to the SB construction. The solution of Equation 2.23 can be obtained by minimizing the L_2-norm of the residual vector (Berardino et al., 2002). In the case of all the SAR images are connected, B is in full column rank. The equivalent single-master phase can be estimated by simple least square methods. To mitigate the possible errors from spatial phase unwrapping, an alternative method is the L_1-norm minimization (Lauknes et al., 2011). For full-rank B, the L_1-norm problem can be solved based on iteratively reweighted least squares method. In the case of several disconnected subsets, the rank-deficient B makes the solution not unique. Singular-value decomposition or other similar pseudo-inverse approaches can be used to find the unique solution for both L_1-norm and L_2-norm minimization.

Different from PSI, the estimated equivalent single-master phase are pre-unwrapped. Given the phase model, the displacement can be easily estimated by another L_1-norm and L_2-norm minimization. The modeled parameters can also be estimated within one minimization by introducing the phase model (such as linear subsidence rate v)

in Equation 2.23:

$$\begin{aligned} \underset{M\times 1}{\phi_{\mathrm{T}}} &= \underset{M\times N}{\mathrm{B}}\ \underset{N\times 1}{\mathrm{A}}\ v \\ \text{where:} \quad A &= [k_{air\Delta}t_1, k_{air\Delta}t_2, \cdots, k_{air\Delta}t_N]^T \end{aligned} \tag{2.24}$$

Compared with PSI, the phase model is not necessarily predefined. Thus, SBAS may perform better in case when the unknown ground movement is difficult to model.

2.3.3 Hybrid multi-temporal InSAR approaches

The key idea of hybrid multi-temporal InSAR (HM-InSAR) is to jointly exploit both DS and PS targets. Based on different application scenarios, HM-InSAR could be implemented under the framework of single-master (such as PSI) or small-baseline multi-master (such as SBAS) configuration. Here to avoid ambiguity, single-master HM-InSAR represent the HM-InSAR group under the framework of PSI (Ferretti et al., 2011; Fornaro et al., 2015; Samiei-Esfahany et al., 2016), and small-baseline HM-InSAR is the HM-InSAR group under the framework of SBAS (Fornaro et al., 2012).

The common and most important step of HM-InSAR is the so-called adaptive spatial filtering (ASF) (Ferretti et al., 2011; Parizzi and Brcic, 2011). Instead of averaging all the pixels inside a boxcar window, the idea of ASF is to spatially average the pixels around a given pixel that are regarded to be statistically homogeneous. The amplitude-based approaches have been proven to be a proper measure for distinguishing between PS and DS targets (Ferretti et al., 2011; Parizzi and Brcic, 2011). A neighborhood homogeneous cluster around each pixel could be identified by using hypothesis test approaches. Depending on the numbers of SAR images used, different hypothesis test strategies could be used to identify the neighborhood homoge-

neous cluster, i.e., non-parametric and parametric test approaches (Samiei Esfahany, 2017). Non-parametric approaches used are based on testing two neighborhood pixel in time domain without any assumption on target probability distribution, such as the Anderson-Darling (AD) test (Pettitt, 1976) and Kolmogorov-Smirnov (KS) test (Kvam and Vidakovic, 2007). Non-parametric approaches could perform well even with a small data stack but with high computational burden. To deal with the computational burden especially in the era of big data InSAR, parametric approaches can be used with the assumption that the DS targets follow Rayleigh distribution (Hanssen, 2001). In this way, the neighborhood homogeneous cluster could be identified by testing the amplitude mean (Jiang et al., 2015) or variance (Parizzi and Brcic, 2011). However, it should be noted that parametric approaches need large data stacks, say larger than 100 images, to ensure the feasibility of tests.

In the case of single-master HM-InSAR, another important idea behind is the so-called phase linking (Guarnieri and Tebaldini, 2008; Ferretti et al., 2011). Other than only dealing with small-baseline pairs, phase linking refers to retrieve N interferometric phases with $N+1$ SAR images by taking full usage of all the $(N+1)N/2$ multilooked or ASF filtered interferogram pairs. The interferograms with large decorrelation noise are understated by given a lower weight based on the target statistics. For a PS target, the phase model proposed in Equation 2.22 still holds. However, for a DS target, Equation 2.22 does not hold due to phase inconsistency. More details about the phase inconsistency are introduced in De Zan et al. (2015). Note that the phase inconsistencies might be also related to the non-linear soil moisture impacts (De Zan et al., 2014; Zwieback et al., 2015a). In general, the linked phase can be estimated by optimizing the covariance or coherence matrix. Different optimization methods have been used, such as maximum likelihood estimation (Guarnieri and Tebaldini, 2008; Ferretti et al., 2011); integer least squares (Samiei-Esfahany et al., 2016); and

eigen-decomposition methods (Fornaro et al., 2015).

In the case of small-baseline HM-InSAR, ASF could be utilized to replace the complex multilooking without need to modifying other steps (Fornaro et al., 2012). In this way, PS targets are reserved. Meanwhile, the performance of spatial phase unwrapping may be improved with minimized resolution loss.

Chapter 3

Mapping and quantifying permafrost thaw subsidence in Eboling Mountain, Tibetan Plateau

3.1 Introduction

Permafrost degradation has become widespread over the Qinghai-Tibet Plateau (QTP) during the recent decades mainly due to continuous climatic warming. The total area of permafrost on the QTP is about 1.06 ± 0.09×10^6 km^2 (Zou et al., 2017). From 1975 to 2006, the total permafrost extent on the QTP shrank by about 0.24 ×10^6 km^2 (Jin et al., 2011). The lower altitudinal limit of permafrost occurrence on the QTP extended upwards by about 40–80 m between the 1970s and the 2000s (Cheng and Wu, 2007; Wang et al., 2000). The permafrost temperature on the QTP was within about 4℃ below the freezing point of water and it increased by 0.1–0.5 ℃ over the past decade (Wu and Zhang, 2008; Wu et al., 2010). One major distinctive form of permafrost degradation is the development of thermokarst landforms. In addition, thermokarst subsidence can severely damage buildings and infrastructure stability (Nelson et al., 2001, 2002). Permafrost thaw subsidence in the Arctic has been investigated by using in situ and remote sensing observations (Günther et al., 2015; Jones et al., 2013; Little et al., 2003; Liu et al., 2015). However, permafrost thaw subsidence on the QTP is still poorly quantified or understood.

The objective of this study is to utilize PSI to map and quantify the gradual thaw

subsidence involved in permafrost degradation. To exploit all repeat SAR acquisitions and to better capture the dynamic processes of the active layer and permafrost, I introduce a piecewise elevation change model that includes the periodic subsidence/uplift as its seasonally varying components as well as linear subsidence trends. Furthermore, I analyze the spatio-temporal patterns of the gradual thaw subsidence and interpret its relationship between thermokarst landforms.

3.2 Study site and field measurements

In this section, I present our study site and field measurements (subsections 2.1 and 2.2). In subsection 2.3, I describe the time series model of permafrost thaw subsidence that I incorporate into our PSI approach. In subsection 2.4, I describe the method of generating a 12-m resolution DEM from TanDEM-X data. This DEM is used in the PSI processing to remove the topographic phases. Finally, in subsection 2.5, I introduce our PSI approach for quantifying the gradual thaw subsidence.

3.2.1 Study site

In this study, I investigate a permafrost region located on Eboling Mountain near the northern edge of the QTP ($38.01^{\circ}N$, $100.90^{\circ}E$) (Figure 3.1a). Our study area is a roughly triangular region bounded by the road and mountain ridges, underlain by ice-rich permafrost which has its main distribution on the north-facing slopes. The northern area, near the road and the western mountain ridge, is predominantly low-lying, whereas the southern area is occupied mainly by the upper slopes. Permafrost temperature at 16-m depth at a borehole (red star in Figure 3.1a) has increased by about 0.2 °C since 2012 (Cao et al., 2018). The study area is characterized by high levels of soil organic carbon and nitrogen stocks in the active layer (Mu et al.,

2017). The active layer thickness (ALT) varies from 0.8 m to 2.0 m with a mean of about 1.3 m (Cao et al., 2017). The mean elevation is about 3,680 m and the spatial extent is about 3.4 km^2. The dominant vegetation is alpine swamp meadow and it is characterized by turf hummocks. This area is dominated by an alpine climate with a mean annual air temperature of about -6℃ to 10℃. Since 1950, the mean annual air temperature has increased by 0.6–1℃ (Mu et al., 2014). The annual mean precipitation is about 400 mm and the mean annual evaporation is about 1,100 mm, with 10% falling as snow in winter.

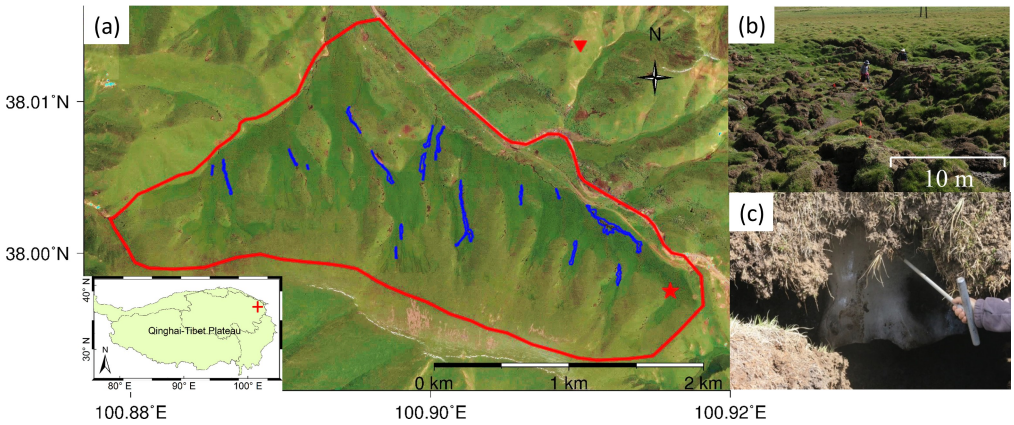

Figure 3.1 Our study site and thermokarst features. (a) Google Earth image of our study site. The red polygon outlines the Eboling permafrost zone (same in all maps). The blue polygons outline the thermal erosion gullies. The red star shows the location of a ground temperature borehole. The red triangle marks the position of our InSAR reference point. The inset denotes the location of our study site (marked by the plus symbol) on the QTP. (b) A ground photo that shows the surficial features inside a thermal erosion gully. (c) A ground photo that shows massive ground ice exposed beneath the active layer within a thermal erosion gully.

Thermal erosion gullies, formed when channelized surface water flow has thickened the active layer and thawed ice-rich permafrost (Jorgenson, 2013), are well developed in this area. In our field investigation in July 2016, I identified and outlined the boundaries of 18 polygons of thermal erosion gullies by using Global Positioning

System Real Time Kinematic (GPS-RTK). The size of these gullies ranges from 20 m to 420 m long, 1 m to 50 m wide, and up to 2 m deep. At meter-level horizontal scales, the microscopic geomorphologic features are characterized by irregular, collapsed-soil, and long fissures (Figure 3.1b). Excess ground ice is abundant and exposed beneath the collapsed active layer (Figure 3.1c).

3.2.2 Field measurements and downscaled air temperature data

I conducted the mechanical probing and the ground-penetrating radar in late September 2014. Mechanical probing inserts a steel rod into the soil until the resistance from the uppermost permafrost is reached. It is the primary way of detecting the ALT if our 1.5 m steel rod can reach the top of the permafrost. Otherwise, ground-penetrating radar is utilized to obtain the ALT. In late September, the thaw depth reaches its maximum, i.e., the ALT. Details on how to obtain the ALT from ground-penetrating radar measurements could be found from Cao et al. (2017).

I obtain the 2 m air temperature in our study area by downscaling the ERA-Interim reanalysis product. ERA-Interim reanalysis data, produced by the European Center for Medium-Range Weather Forecasts (ECMWF), have been well proved to resolve near-surface air temperature for various mountain regions (Bao and Zhang, 2013; Fiddes et al., 2015). Cao et al. (2017) proposed an advanced downscaling approach by incorporating the parameters related to cold air pooling (or winter inverse). The downscaled 2 m air temperature had been validated against the in situ measurements with a high-degree match over the Qilian Mountains during 2012-2016 (Cao et al., 2017). Figure 3.2 shows the downscaled 2 m air temperature in our study area during 2006-2011.

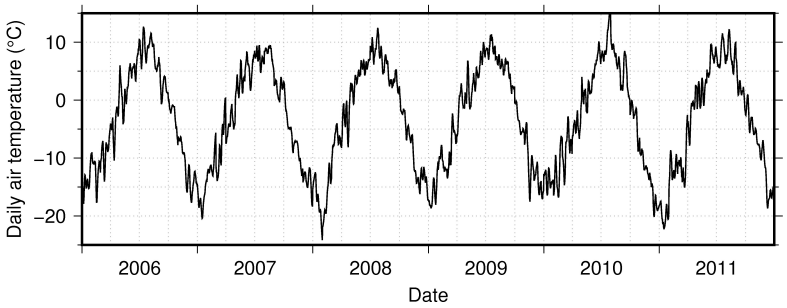

Figure 3.2 Downscaled 2 m air temperature in the study area.

3.2.3 Seasonal and long-term elevation change model

In regions underlain by permafrost, the gradual elevation change (subsidence/uplift) is dominantly associated with the freezing and thawing of the active layer and the uppermost permafrost. The ground subsides seasonally in association with the thawing and volumetric contraction of the active layer due to the phase transition of the frozen soil to a liquid state in summer. Conversely, in winter ground uplift occurs periodically in association with the freezing and volumetric expansion of the active layer due to the phase transition of the unfrozen soil to a frozen state. As soon as the freezing processes stop, the ground surface remains stable until the onset of the next thaw season. Under warming or disturbance, the volumetric ice content may exceed the total soil pore volume in freezing season, forming excess ground ice (van Everdingen, 1998). If the excess meltwater upon thawing in the uppermost permafrost layer is well drained, the ground experiences additional thaw subsidence. Otherwise, the excess meltwater pools up and subsequently triggers the formation of thermokarst landforms.

Here I introduce a piecewise elevation change model to include long-term and seasonal elevation changes by incorporating complete freeze-thaw cycles. Without loss of generality, I define the complete freeze-thaw cycle as a consecutive permafrost year from the beginning of the thaw season until the beginning of the next thaw season.

Liu et al. (2012) introduced a seasonal subsidence model based on the relationship between the seasonal thaw subsidence and the square root of the accumulated degree days of thaw (ADDT). ADDT is calculated based on the Stefan equation (Nelson et al., 1997), which is widely used to estimate the thaw depth. Hu et al. (2018) proposed a new composite seasonal elevation change model to include both the thaw subsidence and the freeze uplift. In the composite model, Hu et al. (2018) used the square root of the accumulated degree days of freeze (ADDF) to account for the seasonal freeze uplift. The underlying assumption of the composite model is that the thaw or freeze front moves from the top downwards, i.e., from the ground surface to the lower boundary of the active layer. In this work, I add a linear subsidence trend to account for the long-term permafrost thaw subsidence in the thaw season.

The seasonal elevation change d at any given time t is (Hu et al., 2018):

$$d(t) = S \cdot I(t) \tag{3.1}$$

where: d_s is the maximum amplitude of seasonal elevation change (m); I is the composite index:

$$I\left(t\right) = \sqrt{A_T\left(t\right)} - \sqrt{\frac{k_F n_F}{k_T n_T}}\sqrt{A_F\left(t\right)} \tag{3.2}$$

where: k_F and k_T are the soil thermal conductivity in the freeze and thaw seasons, respectively; n_F and n_T are the n-factors indicating the ratio between ground surface temperature and air temperature (Lunardini, 1978); A_T and A_F are the ADDT and ADDF (℃ days), respectively; ADDT reaches the maximum at the end of the thaw season. For a complete freeze-thaw cycle, the composite index becomes zero when the active layer is completely frozen. In other words, the total seasonal thaw subsidence is equal to the seasonal freeze uplift within one consecutive permafrost year.

I roughly determine the soil thermal conductivity ($k_F = 1.4\ W \cdot M^{-1} \cdot K^{-1}$; $k_T =$

0.6 $W \cdot M^{-1} \cdot K^{-1}$) based on the local soil type and volumetric water content (Romanovsky and Osterkamp, 2000). The n-factors ($n_F = 0.61$; $n_F = 0.62$) are calculated by Cao et al. (2018).

Then, the piecewise elevation change can be modeled by summing the seasonal elevation changes and the linear subsidence trends:

$$D(t) = \begin{cases} V(t - t_{\mathrm{T}}) + S \cdot I(t) & \text{if } t_{\mathrm{T}} \leq t \leq t_{\mathrm{F}} \\ VT + S \cdot I(t) & \text{if t} > t_{\mathrm{F}} \end{cases} \tag{3.3}$$

where: D is the total ground elevation change on any day t since the thawing onset; V is the rate of the subsidence trends (meters/year); t_{T} and t_{F} are the thawing and the freezing onsets, respectively; T is the number of consecutive permafrost years (in units of years);

Because of a lack of in situ measurements of air temperature during 2006-2011, I calculate the ADDT and ADDF by using the downscaled 2 m air temperature as an alternative. According to the five-year-averaged air temperature, I determine the thawing and freezing onsets as 3 May and 20 October, respectively (Figure 3.2). I assume that the two onset dates were the same during the acquisitions of the SAR images used in this study (i.e., 2006–2011).

3.2.4 DEM generation from TanDEM-X

I generate a high-resolution DEM by using the single-pass InSAR method applied to two TanDEM-X images in the GAMMA software. These are from two ascending SAR acquisitions taken on 2 February 2014. GAMMA is a commercial InSAR data processing software (Werner et al., 2000). To reduce spatial noise, spatial multilooking is applied to the interferogram. The generated DEM has a spatial resolution of about 12 m × 12 m. I use in situ GPS measurements to calibrate the DEM. The DEM is

used to remove the topographic phase contribution in our PSI processing.

3.2.5 PSI approach

A Persistent Scatterer (PS) refers to a stable natural or man-made target that exhibits a consistent phase behavior over time (Ferretti et al., 2001). The PSI method estimates the surface elevation changes through time series by analyzing the differential interferometric phase of discrete targets (only acts as PSs) from repeat SAR images (Colesanti et al., 2003a; Ferretti et al., 2001). In this subsection, I will describe our PSI approach that is specifically designed for permafrost studies by integrating the piecewise elevation change model introduced earlier in section 2.3. Moreover, to improve the performance of PSI in permafrost regions, I introduce the two-order networking approach. Figure 3.3 illustrates the flowchart of our PSI method.

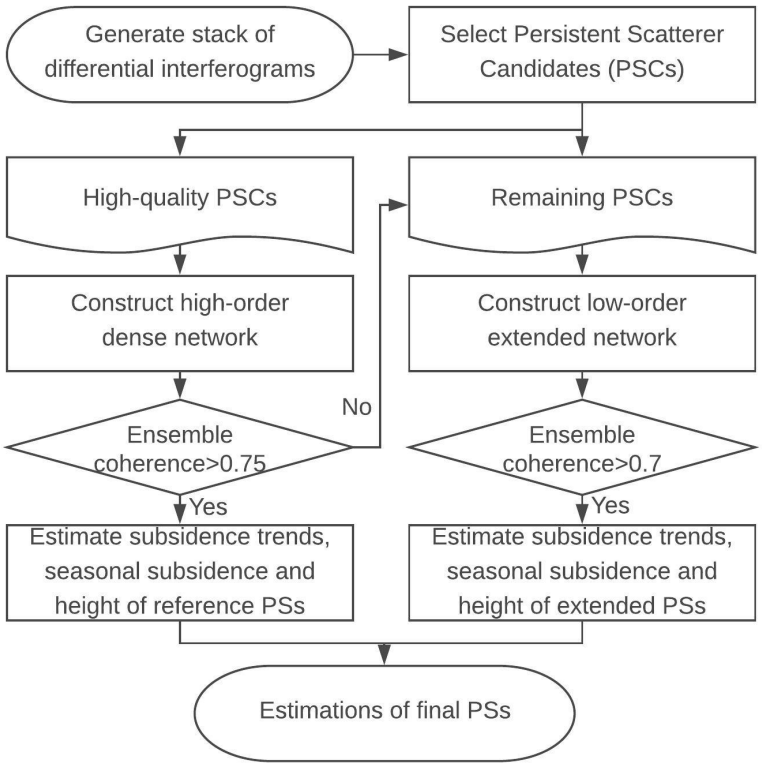

Figure 3.3 The flowchart of the PSI approach. PSs: Persistent Scatterers

I use 17 ascending PALSAR images taken by the ALOS-1 satellite between December 2006 and February 2011. I select the image acquired on 14 December 2009 as the common master image and then generate 16 differential interferograms. Table 3.1 lists the temporal and perpendicular baselines of each interferogram.

Table 3.1 List of interferograms generated in the PSI processing. Common master image was acquired on 14 December 2009.

Slave Image (yyyymmdd)	**Perpendicular baseline (m)**	**Time interval (days)**
20061206	-237	1,104
20070121	-1,817	1,058
20070608	28	920
20071209	1,127	736
20080124	1,560	690
20080310	2,069	644
20080425	2,855	598
20080610	2,798	552
20090613	-1,027	184
20090729	-1,126	138
20100129	714	46
20100616	1,265	184
20100801	1,544	230
20101101	1,763	322
20101217	2,096	368
20110201	2,673	414

The original PSI approach selects the PS targets based on the amplitude dispersion index (Ferretti et al., 2001). The pixel-specific amplitude dispersion is defined as the ratio of standard deviation of the amplitude variation over its mean, representing the amplitude stability over time. If the signal-to-noise ratio of a pixel is high, the amplitude dispersion can serve as a proxy for phase stability in the time domain (Ferretti

et al., 2001). The amplitude dispersion index can detect the man-made structures easily, especially in urban areas. However, in permafrost regions, few targets act at PSs due to the low signal-to-noise ratio resulting in the loss of critical signals. The averaged interferometric coherence could potentially detect more stable targets, helping to detect more landscape-scale details. I calculate the interferometric coherence by taking a spatial average with a 5x5 window for each individual differential interferogram. The averaged interferometric coherence of each pixel is calculated by simply averaging all the interferometric coherence. In this study, I initially select PS targets based on thresholding the amplitude dispersion to be smaller than 0.35 (Hooper et al., 2004) and the averaged interferometric coherence to be larger than 0.5, serving as PS candidates (PSCs).

As described in previous studies (Colesanti et al., 2003a; Ferretti et al., 2001), the differences of the differential interferometric phase between the nearby PSs in the ith interferogram can be written as:

$$\Delta\phi_i = \phi_{\text{def},\ i}\,(\Delta V,\ \Delta S) + \phi_{\text{topo},\ i}\,(\Delta\tau) + \Delta\phi_{\text{atm},\ i} + \Delta\varepsilon_i \tag{3.4}$$

where: $\Delta()$ denotes the differences between the nearby PSs; ϕ_{def} is the phase change due to the surface movement projected into the Light-of-Sight (LOS) direction; V and S denote the rate of linear subsidence trend and seasonal elevation change (Equation 3), respectively; ϕ_{topo} is the residual topographic phase due to DEM error (τ); ϕ_{atm} is the atmospheric phase; and ε is the 2π-modulus of the integer phase and phase noise due to the decorrelation.

I construct a high-order dense network to connect the set of high-quality PSCs, defined by those having an amplitude dispersion index smaller than 0.25. Firstly, I utilize the Delaunay triangulation to connect the high-quality PSCs. I check the number

of connected edges for each of the PSCs. If the numbers are smaller than 5, I add more edges by connecting it to its nearest PSCs by using the k-Nearest Neighbor methods to increase the network density (de Berg et al., 2008). Then, I calculate the differences of the phase for all edges of the network and term them the edge measurements. I optimally estimate $\Delta\tau,\ \Delta V, \Delta S$ for all the edge measurements by using the periodogram approach (Ferretti et al., 2000; Stoica, 2005). I accept only those edges whose ensemble temporal coherence values are larger than 0.75 (Ferretti et al., 2000). The ensemble temporal coherence is defined by the summation of the averaged phase residuals after subtracting the estimated $\Delta\tau,\ \Delta V, \Delta S$ in the time domain. Essentially, a higher ensemble temporal coherence means a more accurate and reliable edge estimation (Colesanti et al., 2003a). I discard the edges that are longer than 1 km to mitigate the spatially correlated phase errors (e.g., atmosphere artifacts and orbital errors). The networking approach keeps more redundant edges and PSs in the high-order network compared to when only the Delaunay triangulation networking is considered.

I then estimate $\tau,\ V, S$ of each PSC relative to the reference point by integrating all the connected edges. The discarded edges break the network connectivity, thereby hampering the integration of the edge estimations. I check the network connectivity and keep the edges connected in the maximum network by using the maximum connected components approach (Tarjan, 1972). I pick a pixel located on exposed bedrock outside the study area as the reference point (marked by the red triangle in Figure 3.1a) and assume that no subsidence occurs at this location during 2006–2011. I integrate all the connected edges by using an iteratively least square approach (Fong and Saunders, 2011). The reserved PSs in the high-order network serve as reference PSs in the low-order network.

Next, I construct the low-order extended network by connecting all the remaining

PSCs to the nearest reference PSs. To exclude outliers, each remaining PSC must be connected to the two nearest reference PSs. To keep more PSs, I relax the ensemble temporal coherence threshold to 0.7. Then, I estimate $\tau,\ V, S$ relative to the reference point for each remaining PSs, i.e., the extended PSs in the low-order network, by simply adding the edge estimations to its connected reference PSs. If two edges are kept for reserved PSs, I average them. Compared with the iteratively networking approach used in Costantini et al. (2014), the two-order network helps to mitigate error propagation due to spatially-related errors, especially in cases of low ensemble temporal coherence in the low-order network. All the reference PSs in the high-order network as well as the reserved PSs in the low-order network are the final PSs.

I calculate the phase residual (ϕ_{res}) after subtracting the estimated $\tau,\ V, S$ for all final PSs as follows,

$$\phi_{\text{res},i} = \phi_i - (c_{v,i}\hat{V} + c_{s,i}\hat{S} + c_{\tau,i}\hat{\tau}) \tag{3.5}$$

where: $\widehat{()}$ denotes the optimal estimation; and $c_v,\ c_s, c_\tau$ are the coefficients for the three parameters $(V, S,\ \tau)$. Ignoring the correlation between the three parameters, the variance-covariance matrix corresponding to the data uncertainty is:

$$\mathrm{C}_\varphi = \begin{bmatrix} \sigma_v^2 & 0 & 0 \\ 0 & \sigma_s^2 & 0 \\ 0 & 0 & \sigma_\tau^2 \end{bmatrix} \tag{3.6}$$

The diagonal entries are the variances for the three parameters. σ_v, σ_s and σ_τ are the standard deviations representing the uncertainties of the linear subsidence trends, the seasonal subsidence, and the topographic error, respectively.

I note that the estimations of V and S are along the slant LOS direction. I convert the LOS deformation to the vertical direction by simply dividing the former by the

cosine of the incidence angles.

3.3 Results

3.3.1 Linear subsidence trends and seasonal subsidence

Figure 3.4a depicts the map of linear subsidence trends during 2006–2011 at the PSs. The linear subsidence trends were up to 4 cm/year inside the study area, whereas the mean value was about 0.5 cm/year. The subsidence trends outside the study area were close to zero. The uncertainties of the subsidence trends were smaller than 0.3 cm/year (Figure 3.4c). The map of maximum seasonal subsidence corresponding to the PSs is shown in Figure 3.4b. The mean seasonal subsidence was about 1.5 cm with the maximum value of 6 cm, whereas its uncertainties ranged from 0 to 2 cm inside the study area (Figure 3.4d); outside the study area, the seasonal subsidence was generally smaller than 1 cm.

3.3.2 Spatio-temporal patterns of surface elevation changes

I analyze the spatial patterns of linear subsidence trends and their relationship to the thermal erosion gullies. I find some PSs inside the gullies, within which the averaged subsidence trends range from 0.3 cm/year to 3.0 cm/year. Because Figure 3.4a also shows the active subsidence trends outside the gullies, I group the pixels into 12 clusters within which the subsidence trends were larger than 0.5 cm/year. I term these clusters as 'actively subsiding areas' or ASAs. Their outlines are depicted in Figure 3.5a. The lengths of the ASAs range from 350 m to 1,800 m and their widths range from 100 m to 350 m. The total size of the ASAs is about 40 times larger than the gullies. I list the area and the mean subsidence trends for each ASA in Table 3.2. I find that five gullies are completely enclosed by ASAs, whereas 11 gullies are across

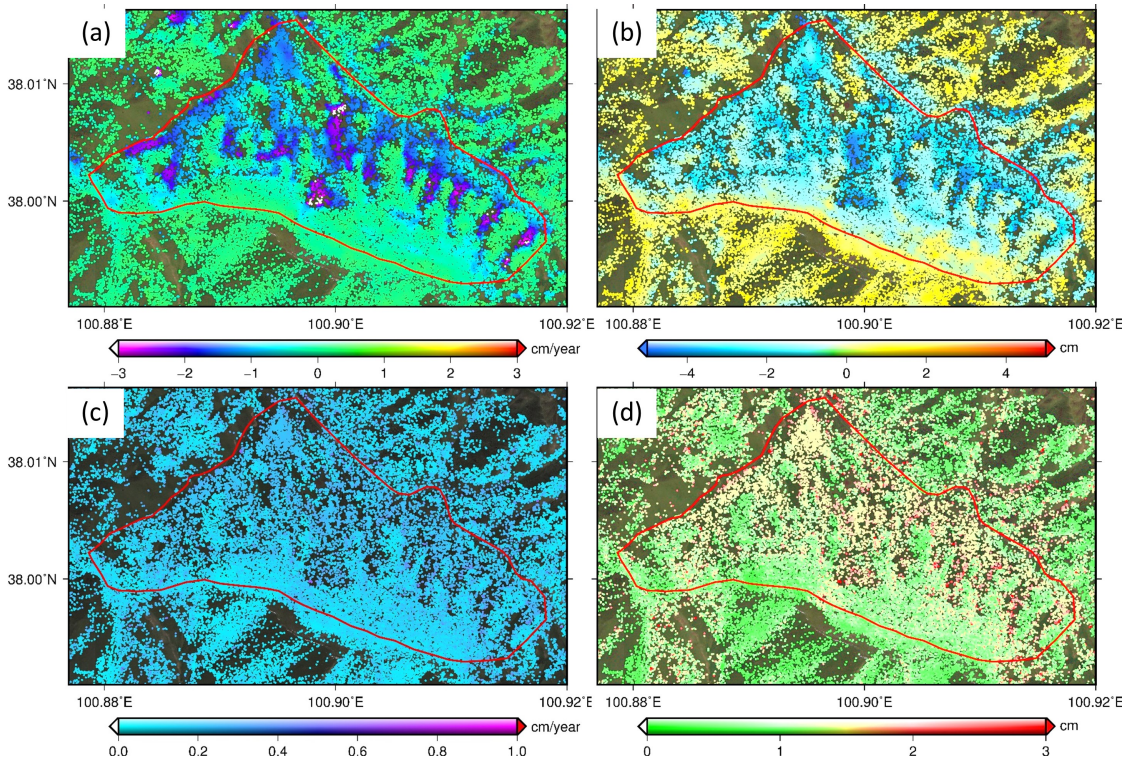

Figure 3.4 The thaw subsidence and its uncertainty. (a) Map of linear subsidence trends from 2006 to 2011. Negative values mean subsidence. (b) Map of maximum seasonal subsidence. Negative values mean subsidence. (c) and (d) show the uncertainties of (a) and (b), respectively.

the ASAs and the rest of the gullies are outside the ASAs. Yet, two of the ASAs contain no gullies. For most of the ASAs, the mean subsidence trends are larger than 1 cm/year. By contrast, the mean trends outside the ASAs were only 0.1 cm/year.

I use two PSs (marked as 'A' and 'B' in Figure 3.5a) as examples to demonstrate the temporal evolution of the surface elevation changes that I estimated from the PSI analysis. In Figure 3.6a and b, the black stars depict the elevation change determined by the phase time series after subtracting the estimated topographic errors, while the black polyline denotes the modeled elevation changes represented by Equation 3. PS point A, located inside the ASA #6 but not inside any thermal erosion gully, experienced seasonal subsidence and uplift up to 6 cm (Figure 3.6a). Its cumulative

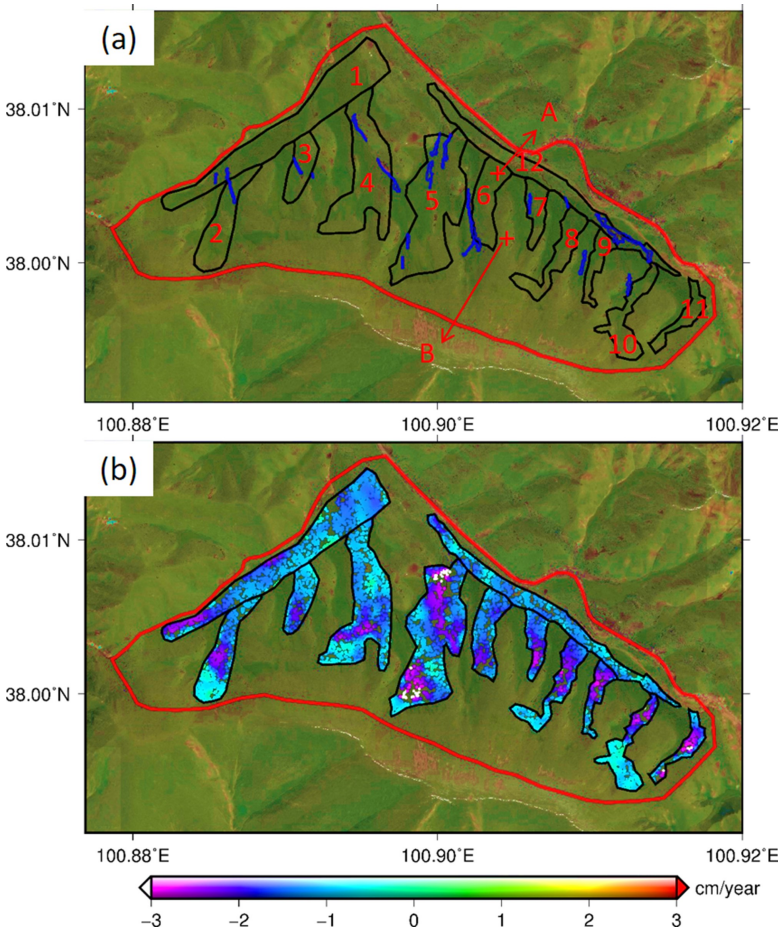

Figure 3.5 The spatial patterns of gradual thaw subsidence. (a) Map of 12 actively subsiding areas (ASAs, black polygons, numbered using the red digits) inside the Eboling permafrost zone. The blue polygons denote the boundaries of thermal erosion gullies. The time series of surface elevation changes at the crosses labeled as 'A' and 'B' are shown in Figure 3.6. (b) Same as Figure 4a but showing only the linear subsidence trends inside the ASAs.

subsidence trends were 8 cm during 2006–2011. By contrast, PS point B, located outside any ASA and far away from the thermal erosion gullies, underwent only negligible seasonal elevation change and subsidence trend (Figure 3.6b).

Table 3.2 The area and average subsidence trends inside the actively subsiding areas (ASAs).

ASA ID	**Area** (m^2)	**Number of gullies inside or cross the ASA**	**Average subsidence trend** (cm/year)
1	281,463	2	-1.3 ± 0.2
2	102,379	1	-1.0 ± 0.2
3	58,649	1	-1.1 ± 0.2
4	218,779	2	-1.1 ± 0.2
5	274,164	5	-1.5 ± 0.2
6	83,655	1	-1.4 ± 0.2
7	44,116	1	-1.5 ± 0.2
8	75,157	0	-1.3 ± 0.2
9	38,745	0	-1.6 ± 0.2
10	39,358	1	-1.6 ± 0.2
11	74,507	0	-0.9 ± 0.2
12	163,374	2	-1.1 ± 0.2

3.3.3 Indirect validation of seasonal subsidence with ALT measurements

Because no in situ elevation change measurements are available from our study period, I indirectly validate the seasonal subsidence estimated from PSI against the values modeled from the in situ ALT measurements. In subsection 2.3, I have assumed and explained that the seasonal elevation changes are mainly determined by the volumetric change associated with water phase transition between the liquid and the solid state in the active layer. Liu et al. (2014) proposed a model to derive the magnitude of seasonal subsidence from ALT and volumetric water content in the active layer. Here I utilize this model to estimate the seasonal subsidence based on the assumption that the active layer is fully saturated, and that the volumetric water content of the fully

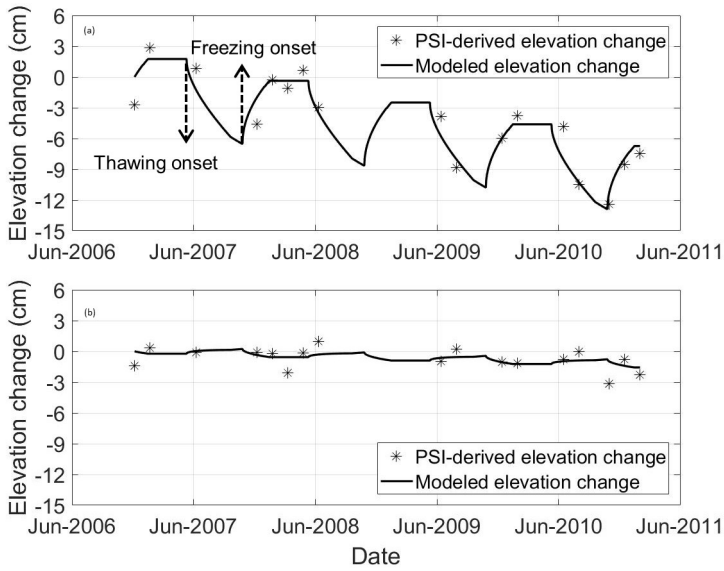

Figure 3.6 Time series of the PSI-derived and modeled elevation changes at points A (a) and B (b), located inside and outside the actively subsiding areas, respectively. Their locations are marked in Figure 5a.

saturated mineral soil is 60%. According to the soil moisture measurements in the study area, the soil in the low-lying areas is fully saturated, but the upper slope is not fully saturated due to water drainage. Therefore, the ALT measurements in the upland areas are excluded from the validation.

To mitigate the negative impacts of spatial heterogeneity on the validation, I calculate the weighted block average to represent the site-specific ALT-derived and pixel-specific PSI-derived seasonal subsidence, respectively. I firstly resample our study region to 100 m $\times$ 100 m blocks. I next calculate the average values of ALT-derived and PSI-derived seasonal subsidence inside each block weighted by its uncertainty. I also calculate the uncertainty of each block (error bars in Figure 3.7) through the uncertainty of observations. Figure 3.7 shows the comparison between the ALT-derived and the PSI-derived seasonal subsidence. I find that 20% of the ALT-derived subsidence is 2 cm larger than the PSI-derived seasonal subsidence. However, due to

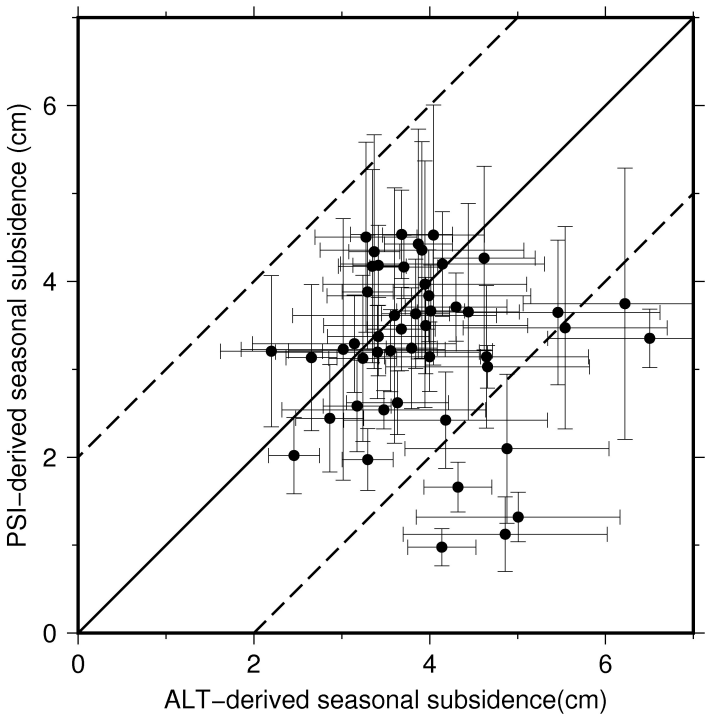

Figure 3.7 The comparison of the ALT-derived and the PSI-derived seasonal subsidence. The black bars show the confidence intervals. The differences between the two seasonal subsidence datasets are smaller than 2 cm within the two dashed lines.

the spatial heterogeneity of soil type and water content, the seasonal subsidence may be overestimated based on ALT inversion; because a lower water content means that there is a lower volumetric expansion/compression of ground surface due to water phase transition. The red dots in Figure 3.8 show the locations of those differences which are larger than 2 cm. All of the eight red dots are far away from the thermal erosion gullies, and outside our defined ASAs or at its edges. The mean bias decreases to 0.1 cm if I remove the measurements with offsets larger than 2 cm. The root-mean-square (RMS) error drops to 0.8 cm. The expected small bias and low RMS error indicate a moderate agreement between the ALT-derived and the PSI-derived seasonal subsidence.

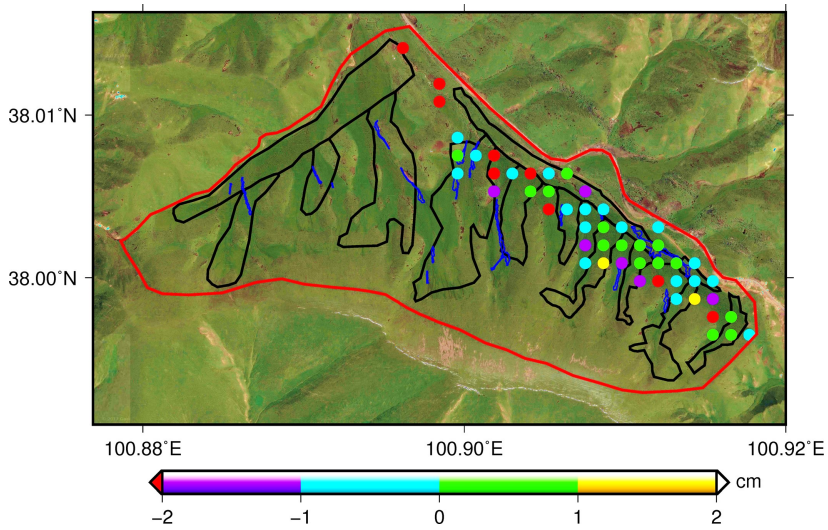

Figure 3.8 The difference between the ALT-derived and the PSI-derived seasonal subsidence (former minus latter).

3.4 Discussions

3.4.1 Geomorphological interpretation of the PSI-derived elevation changes

I have observed gradual subsidence both inside and near the thermal erosion gullies. The distinctive feature of gully geomorphology in our study area shows collapsed surface and exposed ground ice (Mu et al., 2016). Lowering the ground with the collapsed surface facilitates water runoff and leads to drainage of the upland areas in thaw seasons. In addition, the exposed ground ice would melt and increase the water runoff in the subsiding areas. Flowing water results in more heat transfer into the uppermost permafrost, which makes the underlying permafrost more vulnerable to gradual thawing and degradation. Meanwhile, the continuous lateral thawing associated with gully development would thaw surrounding permafrost, i.e., the observed subsidence trends near to the gullies. The thawing of ice-rich permafrost might increase the water content in the active layer near to the gullies, which contributes

positive feedback to permafrost thawing and thermokarst development.

The total extent of gullies and the surrounding ASAs is about 1.2 km^2, suggesting that 28% of the study area experiences permafrost thaw processes during 2006–2011. In other words, compared with the visible gully features, the permafrost degradation occurs in a wider region than I expected. In addition, I find nearly-zero subsidence trends outside the ASAs, suggesting no permafrost thaw. The spatial pattern of the gradual subsidence shows a strong correlation between the gullies and their surroundings, suggesting that the actively subsiding areas are more likely to form thermokarst landforms in our study site. This provides evidence that the development of a thermal erosion gully interacts not only with the underlying permafrost thaw processes but also with its surroundings. The distinct gullies are of major concern and interest to permafrost scientists and engineers. However, little attention has been paid to the surroundings of gullies, where the permafrost might also thaw and degrade. Here I show that the PSI method provides a new way of capturing gradual subsidence over a wider region than the gullies.

3.4.2 Comparison with other surface subsidence studies in permafrost areas

There is a lack of studies of permafrost thaw subsidence in the Eboling Mountain. I do not know if thermal erosion gullies are widely spread. Yet, I find numerous thermokarst landforms (thaw slumps, sinkholes, etc.) in a broader region by visually inspecting of Google Earth images. To put this work in a spatial context, I compared our study with several gradual subsidence studies in other permafrost regions. Antonova et al. (2018) observed accumulated subsidence trends of 4.4 ± 2.6 cm from 2013 to 2015 over a Yedoma landscape in Northern Siberia. Günther et al. (2015) reported an averaged linear subsidence trends of 5.8 ± 2.9 cm/year during 1951-2013

on Muostahk Island, Siberia. Liu et al. (2015) reported linear subsidence trends of 2-8 cm/year over a thermokarst landform in northern Alaska. Streletskiy et al. (2017) measured subsidence trends of 0.4-1.0 cm/year during 2003-2015 over an undisturbed permafrost region in Barrow, Alaska. I note that despite these case studies are conducted at different locations and different time periods, the gradual subsidence trends are all on the order of centimeters per year, similar to our reported subsidence trends.

3.4.3 Applicability of PSI for mapping permafrost thaw subsidence

This study demonstrates the capability of the proposed PSI by incorporating the piecewise elevation change model to capture the dynamic freeze-thaw processes of the active layer and the permafrost, not only in thaw seasons but also in the freeze season, based on all available SAR images. The piecewise elevation change model is relatively simple and does not require lots of inputs, which are always limited or unavailability in mountain permafrost regions. Using more SAR images in PSI tends to improve its performance and allows us to obtain more reliable estimations (Colesanti et al., 2003a). However, on the QTP, the historical L-band SAR images in the thaw seasons are usually limited. Including the SAR images in the freeze seasons can help to better separate the seasonal subsidence and long-term subsidence trends. Furthermore, I find at least two areas (location: $38.0197^{\circ}N$, $100.8664^{\circ}E$; $38.0153^{\circ}N$, $100.8990^{\circ}E$) outside the study area where PSI shows high subsidence trends and Google Earth images indicate thermokarst landforms. The proposed PSI is potentially capable of studying permafrost thaw processes and of assessing its impacts over vast areas on the Qinghai-Tibet Plateau and in the Arctic.

Using the pixel-specific PSI approach, I have detected more detailed geomorphological features associated with the gradual permafrost thaw. More specifically, I successfully

resolve fine-scale targets even inside the narrow gullies and detect gradual subsidence. The SBAS approach, which uses the multi-looked interferograms by taking the spatial average, would smooth the subsidence over these small thermokarst landforms. Furthermore, the atmospheric and orbital artifacts are largely mitigated by exploiting the spatial correlation between nearby targets within the PSI framework. By contrast, the SBAS approach usually applies spatio-temporal filters to reduce atmospheric and orbital artifacts.

However, the surface processes (for instance, vegetation succession, snow accumulation, and soil moisture variation) may cause severe decorrelation and damage the applicability of PSI. In this study area, the vegetation is low (0-20 cm) and snow cover is minimal (0-20 cm) (Cao et al., 2018). The surface soil is nearly saturated throughout the thaw season. I do not expect any multi-annual trends in vegetation, soil moisture, and/or snow cover changes. Therefore, their influences on the estimated subsidence trends are expected to be minimal. However, I cannot quantify to what level the surface processes affect the subsidence trends due to lack of in-situ measurements. Moreover, the application of the PSI approach highly depends on the density of stable ground targets. The surface processes (such as thick snow cover, high vegetation) might affect the PS selection due to severe decorrelation. A low PS density breaks the network connectivity and causes PSI to fail. Further efforts are needed to assess the uncertainty of PSI-derived subsidence trends related to these surface processes.

PSI can hardly detect the abrupt subsidence of the ground and it is susceptible to aliasing problems. Unlike field-based methods, one cannot select observation targets before a PSI analysis. In other words, I can measure only the subsidence over the targets that are selected as PSs. The abrupt subsidence causes severe temporal decorrelation, which results in ground targets being classified as non-PS pixels, where the

signal would be missed. Furthermore, PSI typically requires more than 15–20 acquisitions to ensure the reliability of PS selection (Crosetto et al., 2016). In this study, despite our using all repeat SAR acquisitions and gaining reasonable results, all I have is just 17 acquisitions spanning five years with a gap between June 2008 and June 2009. Thus, due to the limited and irregular sampling of the SAR acquisitions in the time domain, aliasing problems may occur and consequently bias our estimations.

In this study, I focus on the vertical ground elevation changes which occurs associated with the gradually freezing and thawing dynamics of permafrost and active layer. During the development of slopes and/or gullies, mass movement may also occur and cause surface deformation in three dimensions. The decomposited vertical elevation changes related to mass movement would be superimposed into our subsidence model and introduce model misfit. The horizontal surface displacement might be retrieved by combining the ascending and descending SAR dataset (Wright et al., 2004).

3.5 Summary

Using PSI, I are capable of monitoring permafrost thaw subsidence at a fine spatial resolution of about 7 m. I introduce the piecewise elevation change model that includes the seasonal elevation changes and the linear subsidence trends. I incorporate the piecewise elevation change model into our PSI approach to exploit all repeat SAR acquisitions. I find that the gradual permafrost thaw subsidence occurs both inside and around the thermal erosion gullies in an area located on Eboling Mountain between 2006 and 2011. The subsidence trends are up to 3 cm/year inside and around the thermal erosion gullies, suggesting that 28% of the study area experiences permafrost thaw processes, which is about 40 times larger than the visible gullies. The spatial pattern of gradual subsidence trends shows correlations between the gullies

and their surroundings, suggesting that the permafrost thaws and degrades in a wider region than the gullies. This study demonstrates the potentials of using PSI to study permafrost thaw processes and to assess its impacts over vast areas, especially with low vegetation and shallow snow cover.

Gradual thaw subsidence is a widespread phenomenon in permafrost regions. The distinct thermokarst landforms are of major concern and interest to permafrost scientists and engineers. However, little attention has been paid to the dynamic processes of the surrounding ground. The recently launched and future SAR missions, characterized by high resolution and shorter revisit times, provide us with an opportunity to monitor the gradual thaw subsidence at fine resolution of a few meters over large permafrost regions by using PSI. This type of remote sensing measurement can potentially supplement in situ measurements, especially in remote regions.

Chapter 4

InSAR measurements of elevation changes over Yedoma upland on Sobo-Sise, Lena Delta

4.1 Introduction

Yedoma, extremely ice-rich permafrost with massive ice wedges formed in extensive regions in northern Siberia, Alaska, and northwest Canada during the Late Pleistocene (Schirrmeister et al., 2011, 2013), is vulnerable to thawing and degradation under climate warming. The thawing of ice-rich permafrost results in widespread thermokarst development, reshaping the landscape into Yedoma uplands and interconnected drained thermokarst lake (Morgenstern et al., 2011; Ulrich et al., 2014). Due to its syngenetic formation history, Yedoma deposits store large amounts of organic carbon which are vulnerable to mobilization upon thaw (Hugelius et al., 2014; Strauss et al., 2017). Therefore, Yedoma degradation contributes to climate warming through the release of greenhouse gases from microbial decomposition of thawed organic carbon (Schuur et al., 2015; Walter Anthony et al., 2016).

The Sentinel-1A/B constellation is a new generation of two C-band SAR satellites, launched on 3 April 2014 and 25 April 2016, respectively. The main advancement of Sentinel-1 is the new imaging technique, i.e., the Terrain Observation by Progressive Scans (TOPS) (De Zan and Monti Guarnieri, 2006). This technique allows the Sentinel-1 SAR images to cover large footprints (about 250 km across the orbit track)

by three overlapping sub-swaths. Sentinel-1 measurements characterize with frequent revisit time (regular revisit time is 12 days; shortest is six days if both Sentinel-1A and -1B images are acquired). Furthermore, the orbit configuration of Sentinel-1 results in a spatial baseline for InSAR of about 150 m (Yagüe-Martínez et al., 2016). The European Space Agency (ESA), operated Global Monitoring for Environment and Security (GMES) space component program, provides all the Sentinel-1A/B archives at no cost to all users.

However, the availability of suitable SAR images for InSAR measurements not only relies on the revisit time of SAR missions but also highly depends on the interferometric coherence. Interferometric coherence, the similarity between the two SAR signals, is a key indicator of the quality of InSAR measurements. Generally, high interferometric coherence indicates that the phase observations contain useful information and are less affected by noise. The source of decorrelation (loss of coherence) is mainly related to the variation of geometric configuration between the repeat-pass satellites, the temporal variation in the physical features of the ground surface, and the thermal noise (Zebker and Villasenor, 1992; Bamler and Just, 1993). The geometric decorrelation is related to the satellite configurations (i.e., incident angle, wavelength, spatial resolution, and satellite to ground distance) and the spatial baseline between repeat satellite observations. Taking the maximum spatial baseline (about 150 m) as an example, the spatial correlation term is about 0.96, suggesting that the geometric decorrelation for Sentinel-1 InSAR can be ignored (Yagüe-Martínez et al., 2016). Hence, the dominant decorrelation source is the temporal decorrelation related to surface processes, mainly including soil moisture variation, freezing and thawing processes, and vegetation phenology changes and succession.

The space-borne X-band, C-band, and L-band repeat-pass SAR missions prior to the Sentinel-1A/B satellites have been used to monitor seasonal and inter-annual thaw

subsidence in permafrost regions (Liu et al., 2010, 2015). However, these InSAR measurements (C- and L-band) only provide a limited number of repeat images, and hardly resolve the temporal evolution of seasonal thaw subsidence and/or inter-annual variabilities. TerraSAR-X, the X-band repeat-pass SAR mission, provides frequent measurements (regular revisit time is 11 days). TerraSAR-X InSAR measurements have a high sensitivity to changes at the ground surface (Antonova et al., 2016; Zwieback et al., 2016; De Zan et al., 2014). Thus, the interferometric coherence of X-band data drops rapidly through time in tundra lowlands, which limits the suitability of X-band repeat-pass SAR to detect thaw subsidence (Antonova et al., 2018). The Sentinel-1 InSAR measurements with relatively high temporal resolution provide an excellent opportunity to study the suitability of C-band data for permafrost elevation changes in a detailed manner.

The aim of this study is to demonstrate the capability of Sentinel-1 InSAR measurements to detect elevation changes over Yedoma uplands in an Arctic permafrost region. I use the InSAR approach to quantify the seasonal and inter-annual elevation changes over ice-rich Yedoma uplands on Sobo-Sise Island, Lena Delta. To understand the spatial patterns of seasonal subsidence, I analyze the correlation between seasonal thaw subsidence and Yedoma elevation. To account for the temporal evolution of inter-annual elevation changes, I also analyze the relationship between the inter-annual elevation changes and air temperature.

4.2 Study site and field measurements

4.2.1 Study Site

Sobo-Sise Island is located between two Lena River channels (Sardakhskaya and Bykovskaya channels) in the southeastern Lena River Delta, adjacent to the Laptev

Sea (Figure 4.1a). According to Reference (Morgenstern et al., 2011), Sobo-Sise Island belongs to the third geomorphological terrace of the Lena Delta, that is characterized by remnants of Yedoma deposits with large syngenetic ice wedges and hence high ice content (Schwamborn et al., 2002). This island is largely occupied by Yedoma uplands as well as permafrost degradation landforms, such as thermokarst lakes, drained thaw lake basins, and thermal erosion gullies (Morgenstern et al., 2011). The total area of Sobo-Sise is about 340 km^2, accounting for 16% of the Yedoma coverage in the Lena Delta. Fuchs et al. Fuchs et al. (2018) classified and mapped different landforms (Yedoma uplands, thermokarst basins, water bodies, etc.) based on RapidEye satellite imagery. As I focus on Yedoma uplands, I mask out the thermokarst basins and water bodies using this geomorphological classification (Fuchs et al., 2018). Our study domain on Sobo-Sise thus consists of the classes flat undisturbed Yedoma uplands and partly degraded Yedoma slopes from Fuchs et al. (2018). The elevation of Yedoma uplands reaches about 35 m above the sea level (Figure 4.1b).

The closest weather station, located at Samoylov Island about 50 km to the southwest of Sobo-Sise Island, has collected meteorological data since 1998 (Boike et al., 2013). The weather is characterized by extremely cold winters with temperatures around −30 °C generally in January and February and highest temperatures around 10 °C in July and August. The mean annual air temperature is about −12.5 °C and the annual precipitation is in a range of 180–200 mm. Snowmelt usually begins in May and lasts until early to mid-June; by that time, the soil begins to thaw, and the highest thaw rates are recorded in June and July. The maximum thaw depth is reached in late August to early September and snowfall typically starts from early to mid-September. The vegetation coverage is sparse and characterized by moist to wet sedge- and moss-dominated tundra (Schneider et al., 2009). The vegetation growth period lasts from June to September and is roughly similar to the thaw season (Fuchs

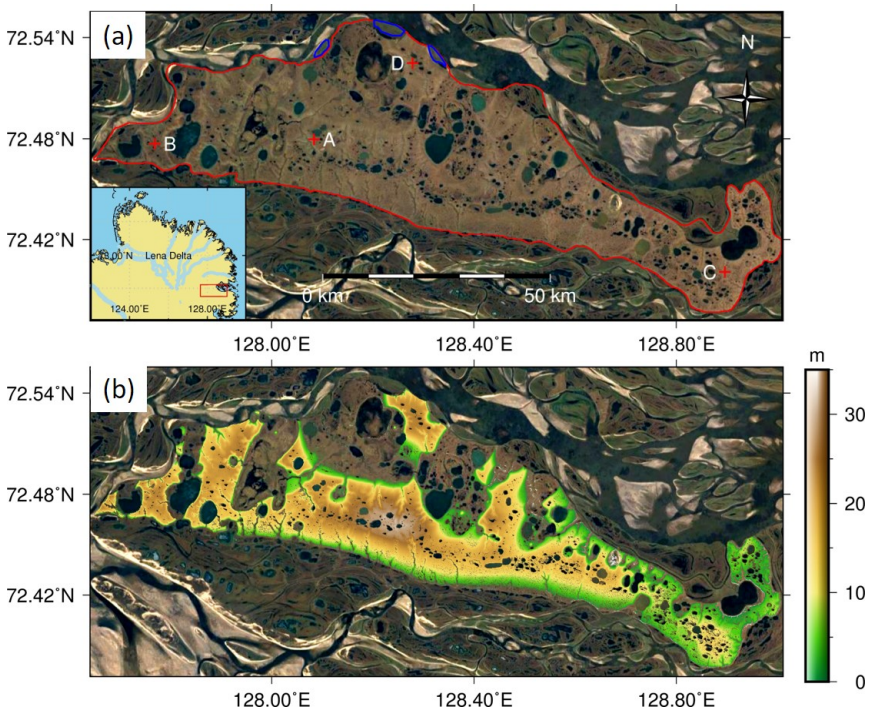

Figure 4.1 (**a**) Google Earth Image of Sobo-Sise Island. The red polygon outlines the island. The red crosses mark the four positions for which I present the results from InSAR time-series analysis. The three blue polygons are used to calibrate the InSAR measurements. The inset shows the location of Sobo-Sise Island in the southeastern Lena River Delta. (**b**) Elevation above the mean sea level over the Yedoma uplands and slopes. Thermokarst basins and water bodies are masked out.

et al., 2018). The maximum active layer thickness ranges from 20 cm to 50 cm on the Yedoma uplands.

4.2.2 TanDEM-X Digital Elevation Model

TanDEM-X (TerraSAR-X add-on for Digital Elevation Measurement) mission provides a global digital elevation model (DEM) product based on bistatic single-pass InSAR measurements (Wessel, 2016). The absolute vertical height accuracy of the TanDEM-X DEM is less than 10 m, whereas the relative height accuracy is about 3 m globally (Rizzoli et al., 2017). In this study, I utilize the standard DEM product

with a spatial resolution of about 12 m to remove the topographic phase contribution in our InSAR time-series processing. Figure 4.1b shows the TanDEM-X DEM over the Yedoma uplands.

4.2.3 Sentinel-1 InSAR Processing

I selected 14 descending Sentinel-1A/B images (6 scenes in 2016 and 8 scenes in 2017, interferometric wide swath mode) taken from the thaw seasons (late June–September). There were no ascending Sentinel-1 images of the same observation mode acquired over this region, therefore none were used in this study. Snow cover would alter the phase center corresponding to SAR images acquired in winter seasons and cause severe decorrelation (Oveisgharan, 2007), making the interferograms less reliable, therefore they were not adopted in this study. The acquisition dates and platforms for SAR image acquisitions are listed in Table 4.1.

I constructed one-season image pairs between any two SAR acquisitions in the thaw season of 2016 and 2017, separately. I excluded image pairs with time intervals exceeding 48 days to avoid severe temporal decorrelation. To exploit the inter-annual elevation changes between two thaw seasons, I also constructed the two-season image pairs with 366 days span. Then, I generated the interferograms for the selected image pairs using the InSAR Scientific Computing Environment (ISCE) (Rosen et al., 2012). I utilized the TanDEM-X DEM product to evaluate and remove the topographic phase of each interferogram. I further excluded the interferograms with low coherence and/or the ones accompanied by strong atmospheric artifacts. The perpendicular and temporal baselines of the selected 32 interferograms are presented in Figure 4.2. The largest spatial baseline is on the order of 150 m. Finally, I unwrapped the interferograms using the minimum cost flow approach (Chen and Zebker, 2001).

I calibrated our interferograms by selecting three regions that I knew from field studies

Table 4.1 The acquisition date and platform of SAR images used in this study.

Acquisition Date (yyyymmdd)	**Platform**
20160722	Sentinel-1A
20160803	Sentinel-1A
20160815	Sentinel-1A
20160827	Sentinel-1A
20160908	Sentinel-1A
20160926	Sentinel-1B
20170617	Sentinel-1B
20170711	Sentinel-1B
20170723	Sentinel-1B
20170804	Sentinel-1B
20170816	Sentinel-1B
20170828	Sentinel-1B
20170909	Sentinel-1B
20170921	Sentinel-1B

or high-resolution imagery where dominated by sandy deposits. The locations of the three sites are outlined by blue polygons in Figure 4.1a. I expect that these sites contain a low ground ice content and are well drained, and thus experience no or very limited elevation changes during 2016–17. I then averaged the interferometric phase for these sites, serving as the reference value, and subtracted it from each individual interferogram. Therefore, reported elevation changes in our study were relative to the reference value. I noted that the estimated elevation changes were along the slant LOS direction. Because the Yedoma uplands were flat, I assumed that vertical movement dominates the deformation. Therefore, LOS deformation rates were converted to the vertical direction by simply dividing by the cosine of the incidence angle.

I retrieved time series of elevation changes for each coherent pixel based on the small

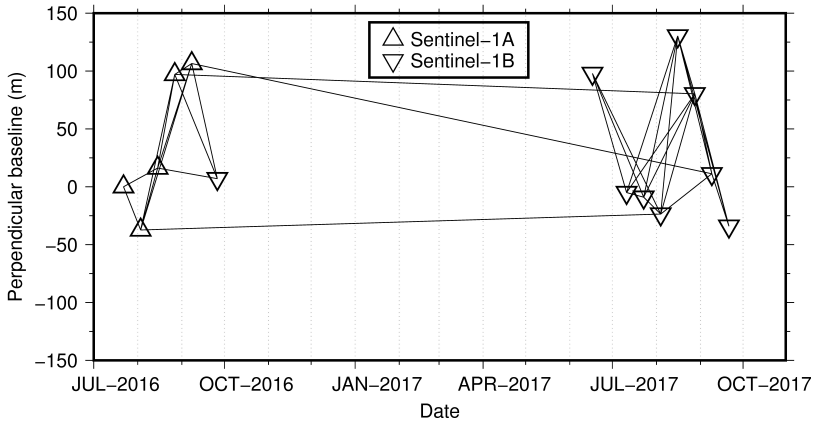

Figure 4.2 The connections between 12 Sentinel-1A/B SAR images with the perpendicular and temporal baselines.

baseline approach. The small baseline approach was proposed to derive the independent deformation with respect to each acquisition time from a set of redundant interferograms (Berardino et al., 2002). The well-developed Generic InSAR Analysis Toolbox (GIAnT) (Agram et al., 2012) was used to derive the time series of surface elevation changes in our study. I removed the possible orbital ramps prior to the time-series analysis, using the network de-ramping approach (Biggs et al., 2007). With each SAR acquisition time, I obtained the elevation changes relative to the first SAR acquisition.

According to the air temperature records, I determined the thawing and freezing onset as 13 June and 7 September in 2017, respectively. Then, I calculated the elevation changes between 17 June and 9 September to account for accumulated seasonal thaw subsidence in 2017. The thawing onset began on 28 May in 2016, which was about half a month earlier than in 2017. Due to no available Sentinel-1 SAR images between 28 May and 22 July in 2016, I could not obtain the maximum seasonal thaw subsidence in 2016. To evaluate the inter-annual elevation changes, I calculated the averaged elevation changes between the five inter-annual image pairs with 366-days interval from the thaw season of 2016 and 2017.

4.3 Results

4.3.1 Accumulated Subsidence in the Thaw Season of 2017

The InSAR measurements show that all the Yedoma uplands undergo ground subsidence in the thaw season of 2017. The accumulated subsidence between 17 June and 9 September in 2017 of up to 2–3 cm is most pronounced on top of flat Yedoma uplands (Figure 4.3). The eastern regions, as well as the outer boundaries of the Yedoma uplands with lower elevation, experience less subsidence (0.5–1.0 cm).

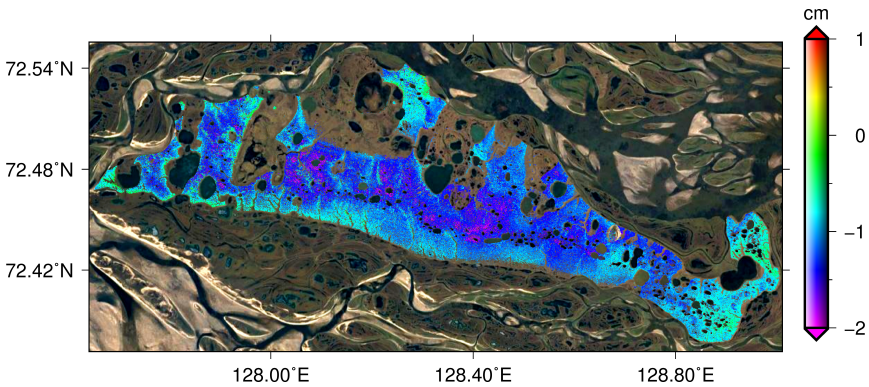

Figure 4.3 Surface elevation changes over the Yedoma uplands on Sobo-Sise Island from 23 June to 9 September in 2017. Minus values denote ground subsidence.

To further exploit the relationship between Yedoma elevation and seasonal subsidence, I averaged subsidence magnitudes in each 5 m elevation interval (Figure 4.4). The seasonal subsidence in different Yedoma height bins reveals exclusively negative changes over time. Stronger subsidence signals on top of Yedoma uplands and less pronounced subsidence are found on upland-surrounding slopes. According to the range of subsidence magnitudes at each elevation bin, the variability of height changes is less pronounced at elevations larger than 25 m.

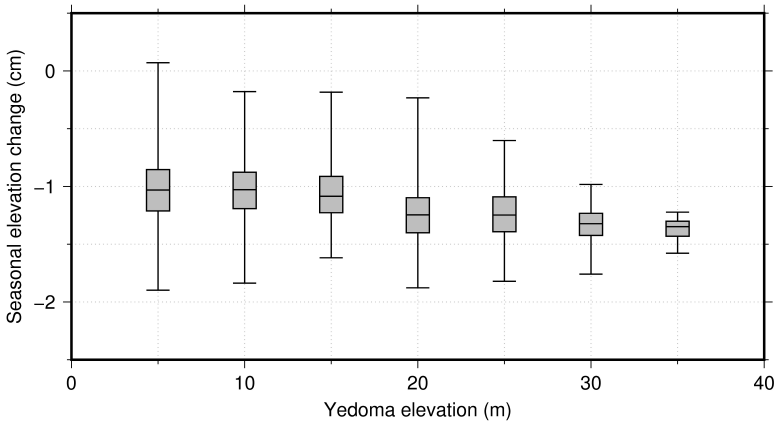

Figure 4.4 Box plot (minimum, first quartile, median, third quartile, maximum) for seasonal subsidence at different Yedoma elevations during the thaw season of 2017.

4.3.2 Inter-Annual Elevation Changes

The averaged inter-annual elevation changes show almost exclusively positive values in most of the Yedoma uplands (Figure 4.5). This suggested the averaged ground subsidence during the thaw season of 2017 is less intense when compared with the preceding year 2016 and results mostly in an overall positive net inter-annual elevation changes of up to 1 cm from late thaw season 2016–17.

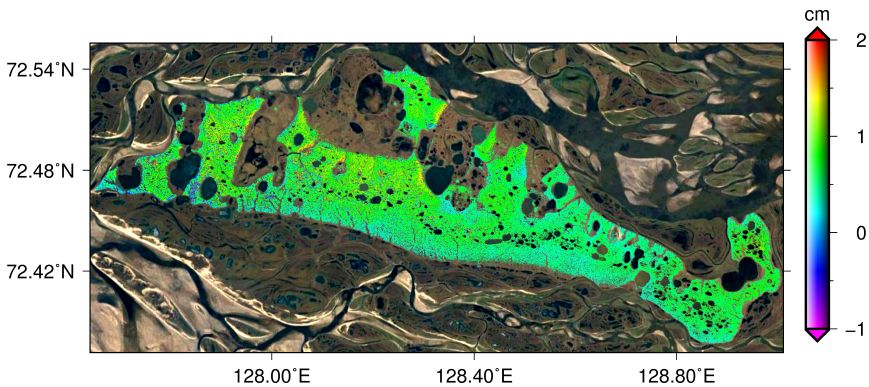

Figure 4.5 Averaged inter-annual elevation changes between the late thaw seasons of 2016 and 2017.

To characterize the temporal evolution of the net inter-annual uplift, I calculated the corresponding elevation changes from six individual image pairs with 366 days interval

between 2016 and 2017 (Figure 4.6). The net inter-annual uplift reaches its maximum values of up to 2 cm at the beginning of August comparing to the preceding 2016. The relative uplift drops rapidly and becomes zero or turns even into subsidence at about −0.5 cm on 9 September 2017 compared to 8 September 2016. Then, the uplift appeared again on 21 September 2017 compared to 26 September 2016.

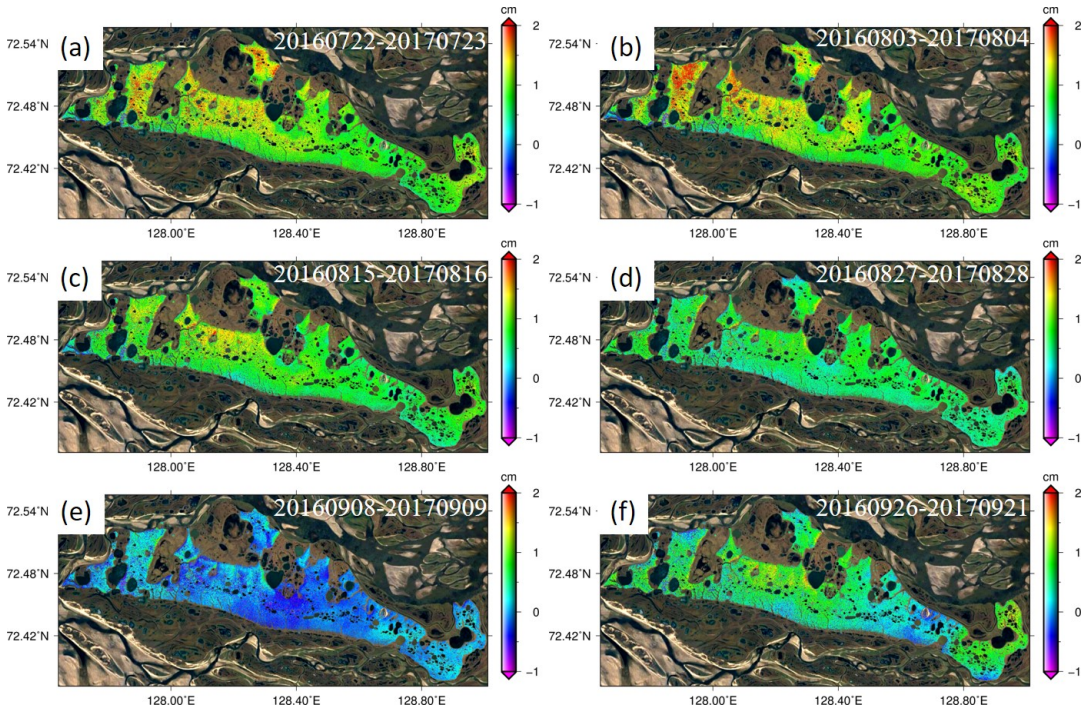

Figure 4.6 Inter-annual elevation changes between image pairs (**a**) 20160722–20170723 (**b**) 20160803–20170804; (**c**) 20160815–20170816; (**d**) 20160827–20170828; (**e**) 20160908–20170909 and (**f**) 20160926–20170921.

4.3.3 Time-Series Analysis of Elevation Changes

I selected four points to demonstrate the time series of elevation changes and their spatial variations derived from InSAR. The ground undergoes limited negative elevation changes between early August and the end of thaw season in 2016 (Figure 4.7). The ground shows stronger subsidence in 2017 comparing to the same period in 2016.

However, the ground begins to uplift around 0.5–1 cm during the early thaw season in 2017. Then, the ground turns to subside around 23 July 2017 and this seasonal subsidence period ends around 9 September 2017. Finally, ground uplift is detected again on 21 September 2017.

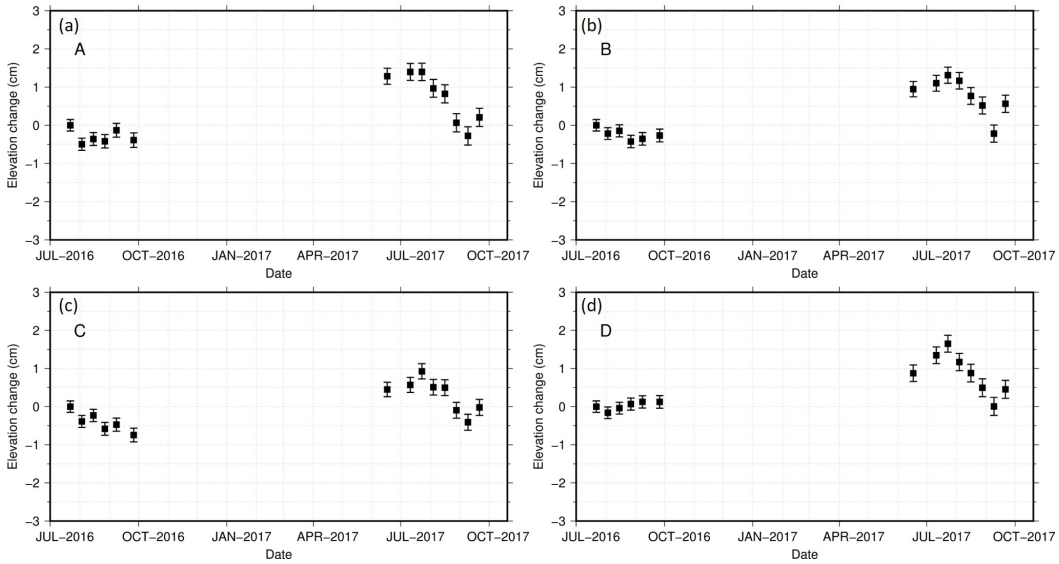

Figure 4.7 Time series of elevation changes based on our InSAR measurements at points (**a**) A; (**b**) B; (**c**) C; (**d**) D relative to the first acquisition on 22 July 2016. The error bars denote the uncertainty of the InSAR time series. The locations of the four points are shown in Figure 4.1.

4.4 Discussions

4.4.1 The Capability of Sentinel-1 InSAR over Permafrost Regions

Sentinel-1 InSAR measurements are capable of capturing both the seasonal thaw subsidence, as well as the inter-annual elevation changes in a permafrost environment. This study benefits from the availability of more InSAR measurements with sufficient coherence in one thaw season and across two thaw seasons. Sentinel-1 InSAR mea-

surements provide an excellent opportunity to identify permafrost-related elevation changes in a detailed manner and therefore help towards a better understanding of the dynamic land surface processes in an ice-rich permafrost region.

The interferometric coherence for all the possible image pairs in 2017 over the Yedoma uplands is shown in Figure 4.8. The 12-days interferograms present relatively low coherence at the beginning (image pair 20170716–20170729) and the ending of the thaw season (image pair 20170909–20170921), whereas the 12-days interferograms in July and August present relatively higher coherence. Antonova et al. (Antonova et al., 2016, 2018) utilized X-band TerraSAR images to detect elevation changes over Kurungnakh-Sise Island, around 50 km away from Sobo-Sise Island. The Yedoma deposits there are of the same origin as at our study site. In contrast to our study, they observed a relatively high coherence at the beginning and ending of the thaw season based on 11-days interferograms acquired from TerraSAR-X images. This might be related to the different sensitivity of X-band and C-band to the thawing and freezing processes. Furthermore, the X-band interferograms with time intervals of more than 22 days show severe decorrelation, when our Sentinel-1 interferograms present moderate coherence even for 48-days intervals or more (Figure 4.9). Better coherence, especially with relatively long temporal baseline, makes the C-band Sentinel-1 InSAR prevail over X-band InSAR in capturing surface elevation changes in permafrost regions.

4.4.2 Correlation between Yedoma Elevation and Seasonal Thaw Subsidence

I find that the highest flat Yedoma uplands, i.e., the undisturbed regions, present the highest seasonal thaw subsidence in 2017. Typically, the water/ice content in the active layer predominantly accounts for the seasonal elevation changes. The active

layer thickness does not significantly vary among the Yedoma uplands (Fuchs et al., 2018). Thus, the highest subsidence amplitudes over the top of Yedoma uplands suggest higher water/ice contents than in lower regions. While the soil organic layer acts as a protective layer slowing the thaw and degradation of underlying permafrost, the thickness of such insulating organic layers is generally rather small (<10 cm) on Yedoma uplands. However, radiocarbon dating of four Yedoma upland cores by Fuchs et al. (2018) demonstrated that even at a depth of 233 cm ice complex Yedoma deposits in a narrower sense were still overlain by the Holocene soil cover. This suggests that even on top of the Yedoma uplands very ice-rich deposits were reached only at greater depth, but with volumetric ice contents of 61.5 ± 15%, the Holocene cover was still prone to thaw and degradation and thus subsequent thaw subsidence processes. However, strong exposure to wind removes snow from uplands and thus limits winter insulation by snow, effectively cooling and preserving near-surface permafrost on Yedoma uplands. A key parameter for upland degradation and thaw subsidence potential seems to be availability and size of flat areas with poor drainage conditions, where subsidence and subsequent positive feedbacks such as water ponding and increases in snow thickness may happen, leading to thermokarst.

4.4.3 Temporal Evolution of Elevation Changes

The net inter-annual uplift from late season 2016–17 observed was possibly caused by delayed thawing associated with differences in summer air temperatures. I downloaded the air temperature and snow cover records from a meteorological station located on Stolb Island, about 40 km west of Sobo-Sise Island (`https://rp5.ru/Weather_in_the_world`). According to the air temperature records, degree days of thawing (days) in 2016 were 812, and in 2017 only 667. I also observed a shift of the warmest month from typically July to August (Figure 4.10). Mean air temper-

ature in July 2016 was 7.8 °C and in August was 7.3 °C. In 2017, July temperature was only 7.2 °C, while August was warmer at 8.3 °C. Even more pronounced were differences between September 2016 and 2017 (164 vs. 63 degree days of thawing). These support our observation of higher surface elevations in 2017 compared to those at the same time in 2016. However, the 20160908–20170909 image pair in Figure 4.6 suggests that elevation changes turn into inter-annual thaw subsidence later at the end of the 2017 thaw season. The apparent pseudo-uplift between the thaw seasons in 2016 and 2017, therefore, reflects a delay in progression of the thaw season and implies that seasonal thaw settlement may not develop simultaneously when compared to the preceding year. This also suggests that it is not appropriate to estimate the inter-annual subsidence by simply averaging the elevation changes. A detailed assessment of meteorological and permafrost conditions for the analyzed years should be necessary to interpret the actual evolution of elevation change dynamics.

The InSAR-derived elevation changes show obvious uplift in the early thaw season of 2017. This might be due to the so-called summer heave. In early thaw season, excess water (for instance, rain, snowmelt, and groundwater flow) could penetrate into the underlying frozen active layer and even the adjacent permafrost and refreeze. Mackay et al. (Mackay, 1983) observed summer frost heave up to 1 cm at Garry Island, Canada, from five years of field measurements. According to the relatively thicker snow accumulation in the winter season between 2016 and 2017, the excess snowmelt water makes the ground more prone to undergo summer heave. Furthermore, the downward water movement makes the frozen ground saturated or oversaturated and thus needs more heat flux to thaw, which further supports the likely delay of thaw season in 2017. However, Zwieback et al. (2015b) reported that the post-snowmelt drying processes would potentially change the dielectric property of the ground surface and thus contribute to the uplift-like signal in L-band InSAR.

Because the sensitivity of C-band Sentinel-1 InSAR to changes of dielectric properties is still not well determined and no in situ soil moisture measurements were conducted in our study area, so at this point I cannot determine if the uplift is spurious. Evidence of ice and snow suggests that penetration depth depends on carrier frequency, physical and electrical characteristics which may vary according to climate conditions (Lin et al., 2017). To account for the observed uplift within one thaw season, further efforts should focus on the question to what extent the soil moisture variations affects InSAR observations.

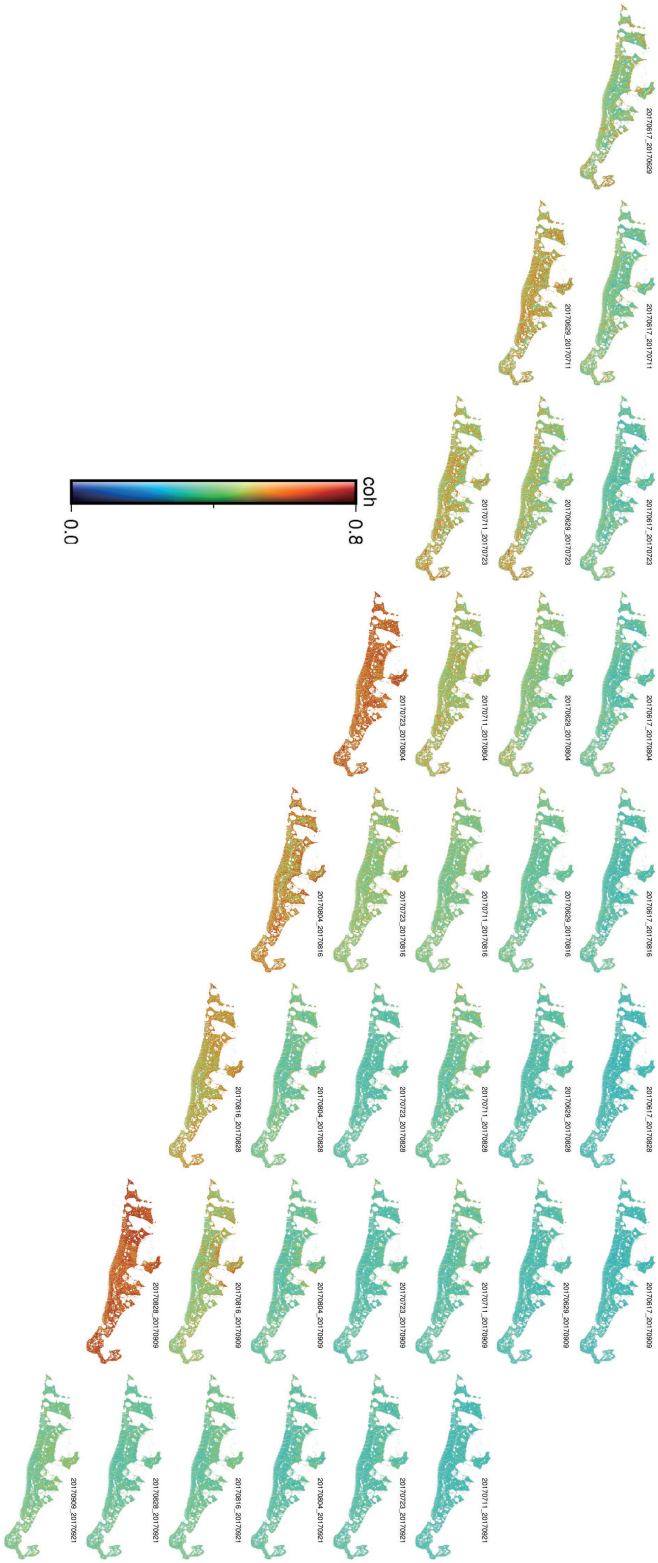

Figure 4.8 All the possible coherence maps for the thaw season of 2017.

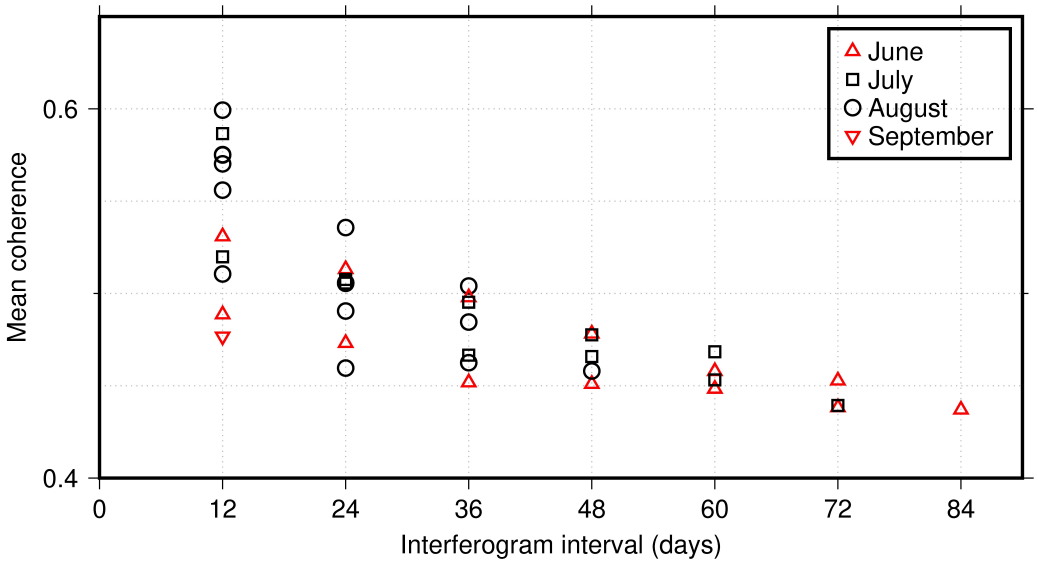

Figure 4.9 Mean coherence over the Yedoma upland for all the 2017 interferograms. The legend symbols denote the months of the master images used to construct the interferograms.

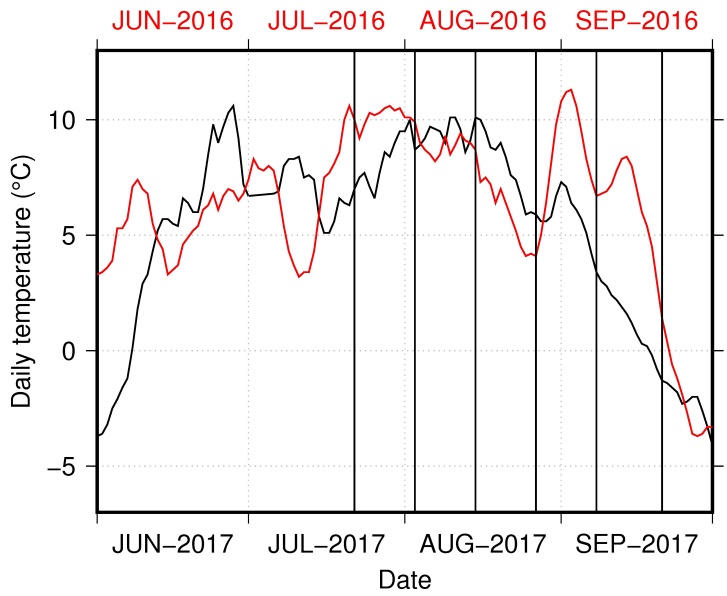

Figure 4.10 Daily air temperature for the thaw season of 2016 (red) and 2017 (black). The six vertical solid lines denote the dates of the inter-annual SAR acquisition pairs.

4.5 Summary

I explored and successfully tested the capability of Sentinel-1 InSAR measurements for quantifying both permafrost thaw subsidence during one thaw season and the inter-annual elevation changes between two thaw seasons. Compared with X-band InSAR in Yedoma uplands, the C-band Sentinel-1 InSAR shows higher coherence, even for the interferograms between the years. I found that the flat tops of Yedoma uplands exhibit the highest seasonal elevation changes. Benefitting from the Sentinel-1 InSAR measurements with short time intervals (12 days in this case), I found that delayed thawing associated with air temperature fluctuations affects inter-annual elevation changes. I also observed an uplift in the early season of 2017, which may relate to effects of early summer heave or soil moisture impacts. To discriminate these and to better interpret the InSAR-derived elevation changes, further research should focus on impacts of soil moisture variation on InSAR measurements. Our study suggests that the Sentinel-1 InSAR measurements with high temporal resolution are capable of detecting permafrost-related elevation changes in a detailed manner and therefore help to better understand the land surface dynamics in an ice-rich permafrost region.

Chapter 5

Permafrost degradation evidence from InSAR in Bayelva, Spitsbergen

5.1 Introduction

Permafrost in Svalbard is the warmest compared to other permafrost regions at the same latitude (Christiansen et al., 2010). Due to the complex topography and warm ocean current, permafrost in Svalbard is highly vulnerable to temperature and thickness changes when compared to the lowland permafrost in northern Siberia, Canada and Alaska (Humlum et al., 2003). Permafrost degradation and thawing is widespread in Svalbard. As illustrated in previous chapters (Chapter 3 and 4), thawing and degraded permafrost lower the ground surface and/or deepen the active layer. In addition, thawing and degrading permafrost is threatening the infrastructure (such as buildings, roads and railways, airports, and pipelines etc.). The infrastructure damage is unprecedentedly challenging the local economic and social sustainability, climate migration and adaptation, and human well-being. However, the ground elevation changes in Svalbard are little quantified or understood.

The ground subsidence from both the ground surface and the above buildings are key indicators for accessing the permafrost degradation and their impacts on infrastructures. The proposed PSI method in **Chapter 3** successfully detected the detailed subsidence around the thermal erosion gullies in QTP; but the extremely strong tem-

poral decorrelation aforementioned as well as the unknown subsidence model make the PSI unsuitable in this study. Through constructing small temporal- and spatial-baseline as well as utilizing boxcar multilooking spatial filter, small-baseline InSAR (SBAS) approach has been initiated to mitigate the aforementioned decorrelation and successfully documented the permafrost thaw subsidence (Liu et al., 2010, 2015). But, the spatial multilooking reduced the spatial resolution and cannot detect the infrastructures (e.g. building, roads) surrounded by permafrost ground.

The objectives of this study are to (1) map and quantify the long-term thaw subsidence both from the permafrost ground surface and the above infrastructures during the past three decades (1998-2018) based on multi-temporal InSAR approach, and (2) attempt to link the remote-sensing-based subsidence to field measurements. To isolate the persistent scatterers and meanwhile mitigate the resolution loss, an advanced hybrid multi-temporal InSAR approach is introduced.

5.2 Study site

The study site lies in the unglaciated coastal areas between two mountains (Zeppelinfjellet and Scheteligfjellet) and Ny-Ålesund village on Brogger peninsula, Svalbard (Figure 5.1). The depth of continuous permafrost is about 100 m and the active layer thickness (ALT) ranges between 1 and 2 m (Humlum, 2005). The coldest month is mostly in January with average air temperature ranging from -17 °C to -3.8 °C , whereas the warmest month is mostly in July with average air temperature ranging from 4.6 °C to 6.9 °C since 1998 (Boike et al., 2018b). The annual precipitation is about 400 mm, which mostly falls as snow between September and May. The vegetation coverage is about 50-60% with height up to about 20 cm, with the remainder being bare soil with a small portion of stones.

The Bayelva observation site was built about 3 km from Ny-Ålesund village in 1998 by researches from the Alfred Wegener Institute (AWI) (Roth and Boike, 2001; Boike et al., 2018b). Plenty of meteorological (e.g., air temperature, snow depth, rainfall) and subsurface soil data (e.g., permafrost temperature, soil moisture, soil dielectric properties) has been recorded since 1998.

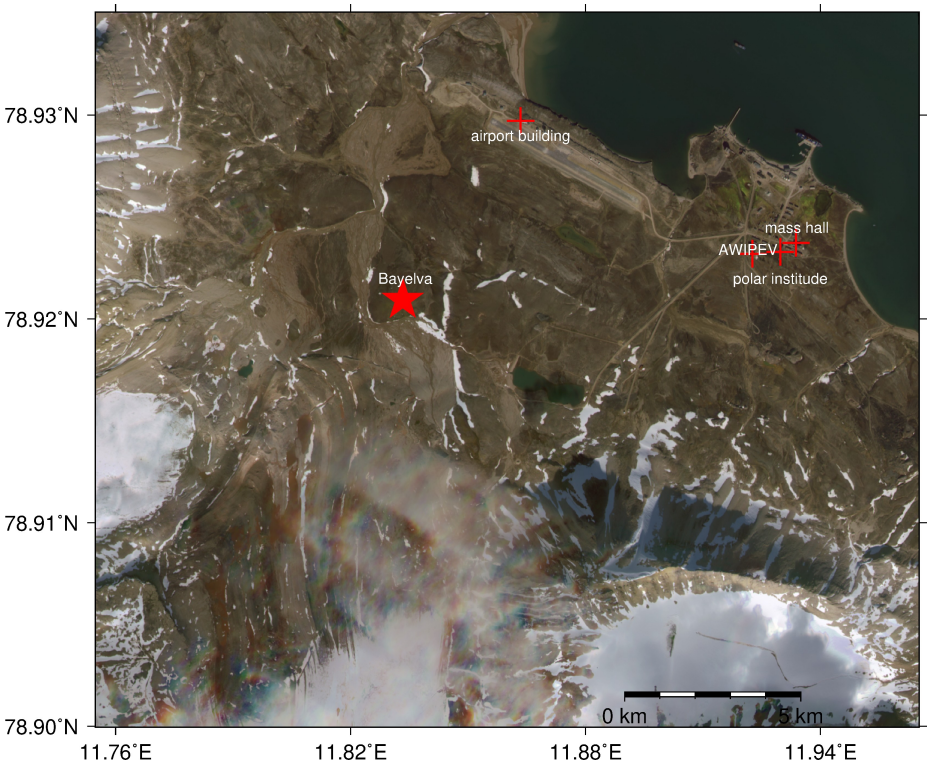

Figure 5.1 Aerial image captured in August 2008. The time-series of surface elevation changes at the red crosses labeled as 'airport building', 'polar institute', and 'mass hall' are shown in Figure 5.6. The red star marks the location of Bayelva observation site.

5.3 Data and methods

5.3.1 DEM data

The airborne HRSC-AX (high resolution stereo camera), a multi-spectral and multi-stereo pushbroom instrument, took place in July 2008 over our study site. A high-resolution (0.2 × 0.2 m) DEM is generated by using digital photogrammetric technique. The DEM is then resampled to 5 m and used to remove the topographic phase in interferograms. More details about HRSC-AX DEM is introduced in Boike et al. (2018b).

5.3.2 Hybrid multi-temporal InSAR approach

I take use of the single-look small-baseline (SB) interferograms and incorporate adaptive spatial filtering in the hybrid multi-temporal InSAR approach. SB interferograms have the advantages of less sensitivity to the strong geometric and temporal decorrelation, especially for the archived ERS-2 data. Instead of multilooking based on a box-car window in conventional SBAS, the adaptive spatial filtering (ASF) just calculates the average of the so-called statistically homogeneous distributed scatterers(Ferretti et al., 2011; Parizzi and Brcic, 2011). In this way, the adaptive filtering preserves the pixel-specific persistent scatterers and reduces the thermal noise by statistically averaging the distributed scatterers with minimum resolution loss. The flowchart of the hybrid multi-temporal InSAR approach is shown in Figure 5.2. Note that ERS-2 and Sentinel-1 data are processed separately but follow the same approaches.

5.3.2.1 ERS-2 and Sentinel-1 interferograms

To exploit the long-term subsidence trends, I use 35 descending ERS-2 and 59 descending Sentinel-1 SAR images taken during 1995-2009 and 2015-2018, separately. I select the SAR images acquired in snow-free seasons. There are averagely 2.3 ERS-2

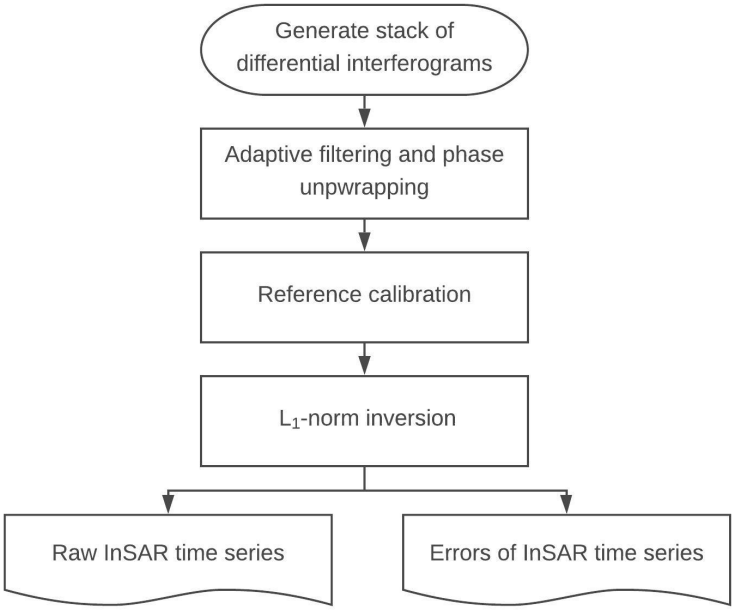

Figure 5.2 The flowchart of multi-temporal InSAR approach

SAR images in each summer season. In our study area, I obtain Sentinel-1A SAR images every 12 days from 2 August 2015 to 25 September 2016. The regular revisit time has became 6 days since both Sentinel-1A and Sentinel-1B started to be fully operation from 25 September 2016. Due to the different revisit time of ERS-2 and Sentinel-1 acquisitions, the strategies to construct the interferogram pairs are different. For Sentinel-1, the same method used in **Chapter 4** is used. For ERS-2, all the image pairs within 5 years are constructed, whereas the pairs with low quality are manually discarded. The acquisition dates and perpendicular baselines are shown in Figure 5.3. All the differential interferograms are generated by using the GAMMA software (Werner et al., 2000).

5.3.2.2 InSAR time-series analysis

To preserve PS targets and mitigate the resolution loss for DS targets, adaptive spatial filter (ASF) is used to filter the SB interferograms before spatial phase unwrapping

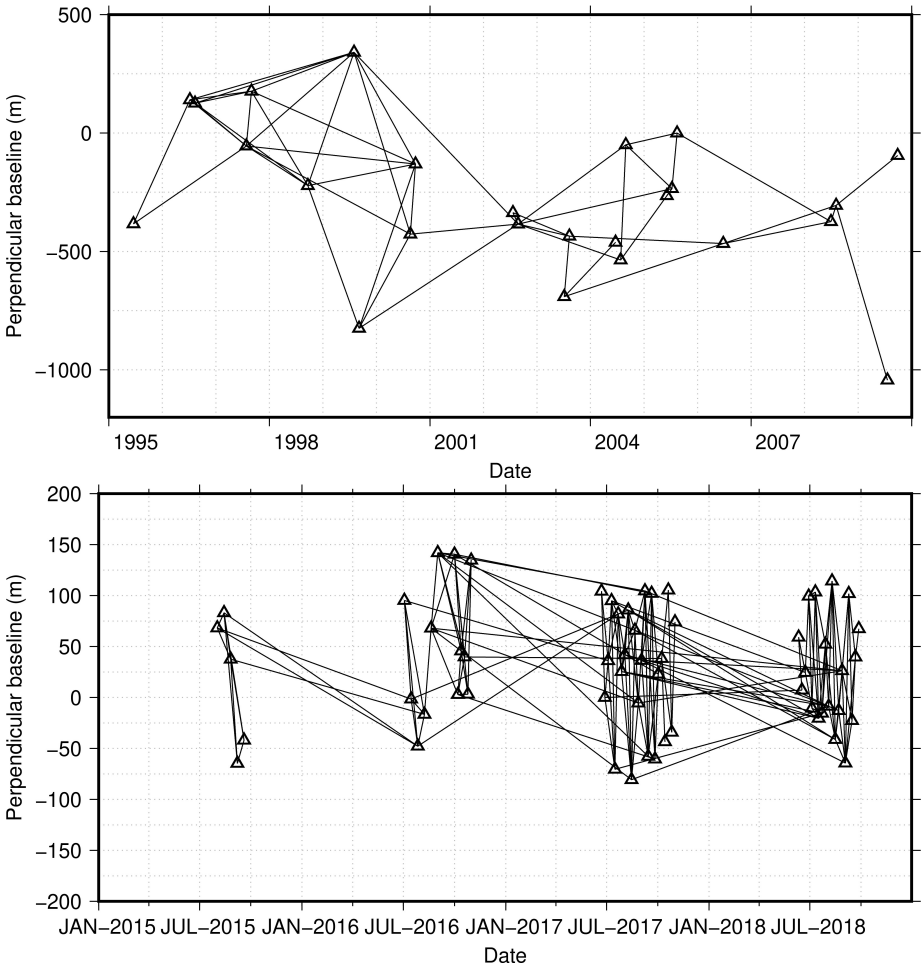

Figure 5.3 Baseline networking of (a) ERS-2; (b) Sentinel-1A and -1B

(Fornaro et al., 2012; Goel and Adam, 2012). Due to the limited numbers of SAR images, the Anderson-Darling (AD) test (Pettitt, 1976), a non-parametric hypothesis test approach, is used to identify the neighborhood homogeneous cluster around each pixel. The filtered SB interferograms are then spatially unwrapped by using minimum cost flow approaches (Costantini, 1998; Chen and Zebker, 2001).

InSAR-derived subsidence is a relative value with respect to a reference pixel which assumed to be stable. However, there are few stable targets in permafrost environment because the ground surface normally suffers from seasonal subsidence and uplift. Even stable targets exist, under the SBAS framework, these targets are multi-looked and

blurred by surrounding targets. The aforementioned ASF could preserve the signal from stable targets. In the study site, several buildings are anchored into about 10 meters depth in permafrost and are assumed stable. The reference value is then calculated from the average phases from these stable buildings.

The severe decorrelation, especially in the ERS-2 data stacks, may introduce phase unwrapping errors. An L_1-norm minimization, which is robust than L_2-norm minimization, is used to retrieve phase time series without any assumption on ground subsidence (Lauknes et al., 2011; Goel and Adam, 2012). During 1998-2018, the active layer thickness (ALT) changed roughly from 1 m to 2 m. The deepening ALT would enlarge the seasonal subsidence in terms of the seasonal thawing and freezing. In addition, the seasonal subsidence may be temporally correlated to subsidence trends, which makes the separation of seasonal subsidence and subsidence trend almost impossible by only using InSAR. Thus, I choose not to separate the seasonal subsidence and subsidence trends.

5.4 Preliminary results

5.4.1 InSAR subsidence maps

Figure 5.4 shows the map of accumulated subsidence and its uncertainties from 1995-06-18 to 2009-07-19. The maximum accumulated subsidence is around 6 cm and its uncertainty ranges from 0 to 3 cm.

5.4.2 Long-term InSAR time-series

5.4.2.1 Bayelva site

The subsidence time-series at the Bayelva site is shown in Figure 5.5. The total accumulated subsidence derived from ERS-2 InSAR is $\sim$ 4-6 cm between 1995-06-18

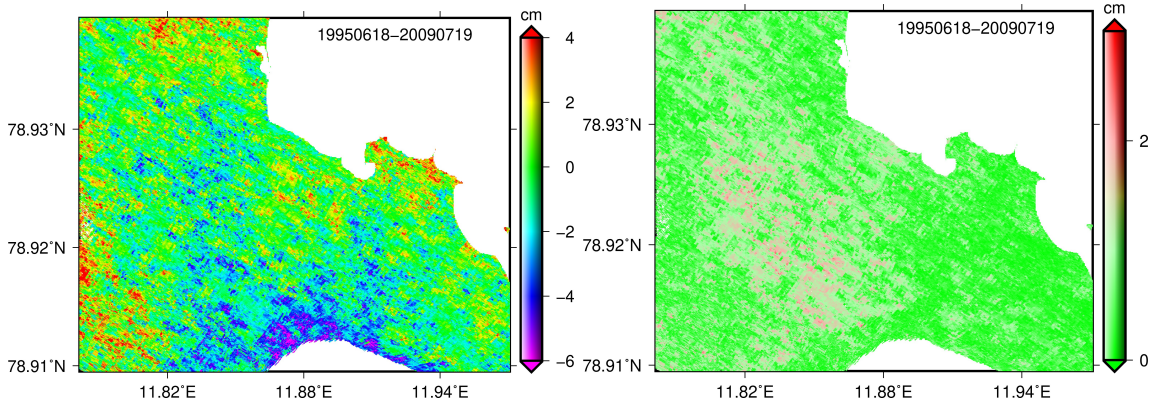

Figure 5.4 (a) Accumulated ground subsidence between 1995-06-18 and 2009-07-19; (b) The uncertainty of accumulated subsidence. Negative value means ground subsidence.

and 2009-07-19, whereas accumulated subsidence derived from Sentinel-1 InSAR is roughly 1-2 cm. Due to the large uncertainties and limited SAR images, there is no clearly seasonal subsidence in the ERS-2 InSAR time-series. The seasonal subsidence is roughly 2 cm in the Sentinel-1 InSAR time-series.

5.4.2.2 Buildings in Ny-Ålesund village and airport

The building of polar institute built in 1999 underwent 1-2 cm seasonal subsidence during 2015-2018. A sudden subsidence up to about 2 cm is found in the summer of 2018. The building of mass hall built in 1957 suffers strong elevation disturbance up to 4 cm in the summer season of 2017 and 2018. A building in the airport underwent similar seasonal subsidence around 1-2 cm. For all the three building, there is no clear subsidence trend.

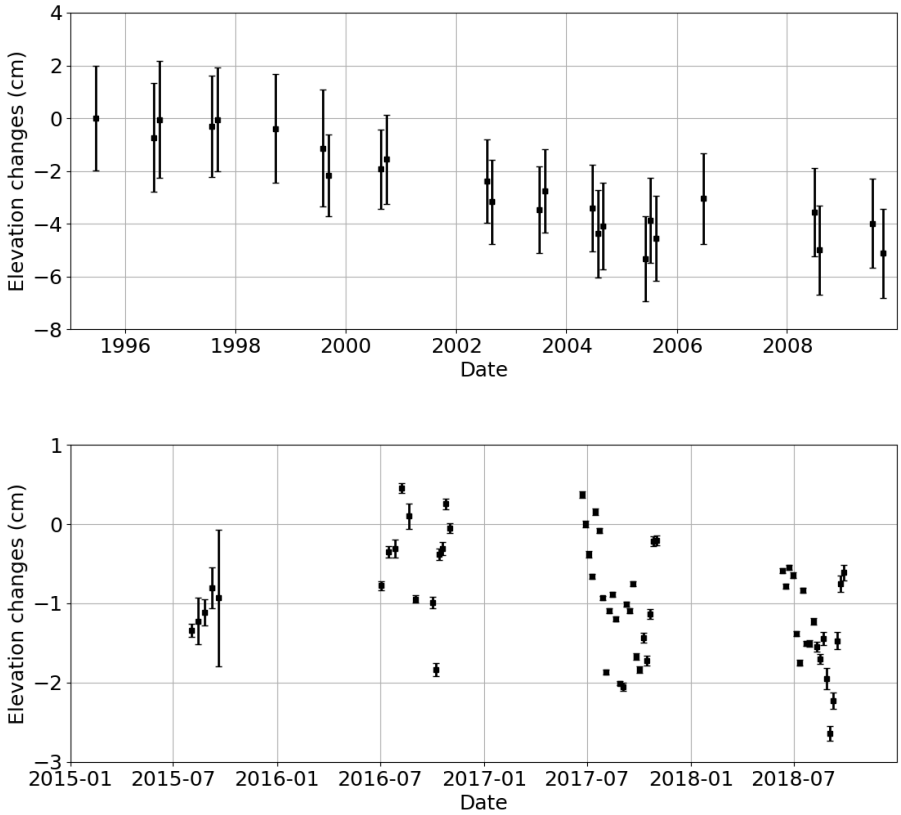

Figure 5.5 InSAR subsidence time-series of (a) ERS between 1995-06-18 and 2009-07-19; (b) Sentinel-1 between 2015-08-02 and 2018-09-21.

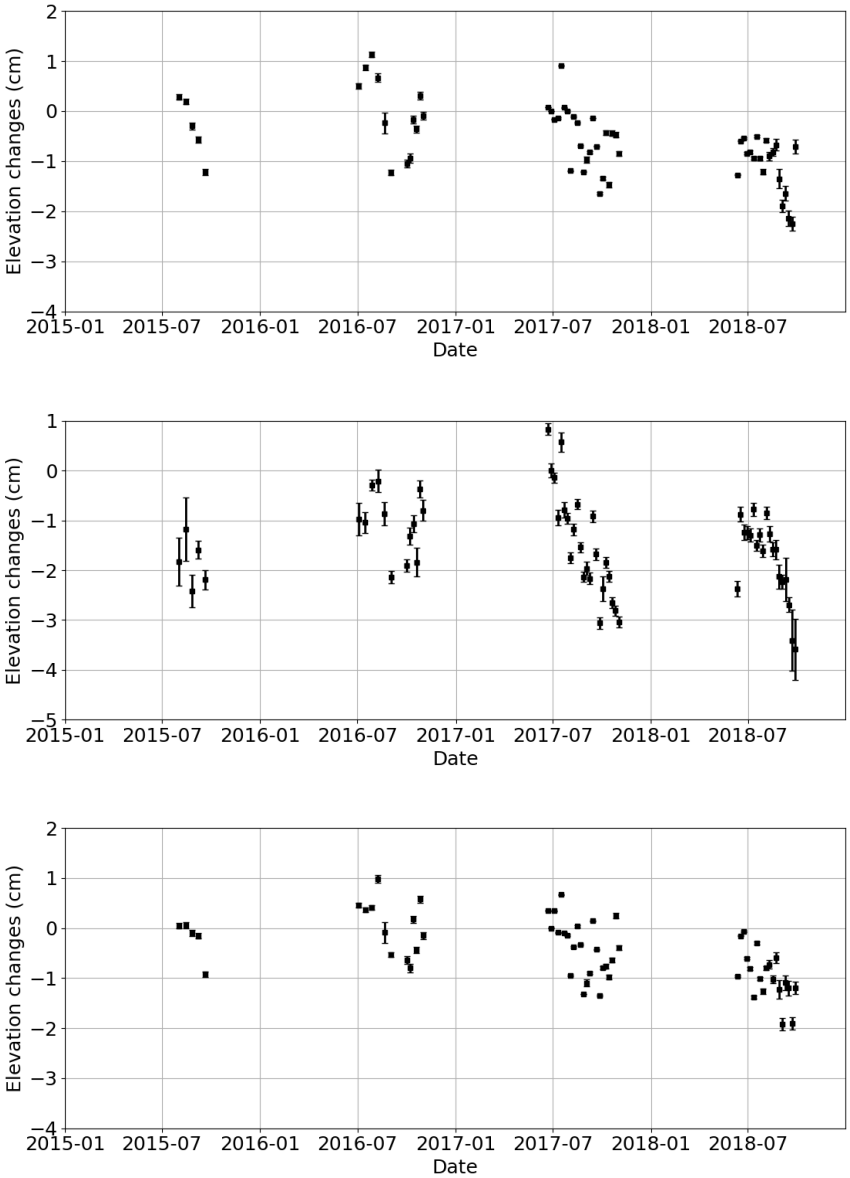

Figure 5.6 Sentinel-1 subsidence time-series of (a) the building of polar institute (latitude: 78.923283° , longitude: 11.929776°); (b) the mass hall (78.923732 ° , 11.933765°); (c) a building in the airport (78.929705° , 11.863437°) during 2015-2018. The position of the three buildings are marked out by the red crosses in Figure 5.1

5.5 Discussion

5.5.1 Degrading permafrost in Bayelva

Evidence from field measurements shows that permafrost at the Bayelva site is degrading and warming during 1998-2018 (Figure 5.7). The increased yearly averaged soil moisture is expected to be mainly related to the increased precipitation (Boike et al., 2018b). Meanwhile, the mean soil temperature in the active layer also increased by around 1 °C . The modeled active layer thickness using the Stefan equation and field measurements has increased continuously from about 1m in 1999 and is estimated to have surpassed 2 m in 2018 (Boike et al., 2018a). In addition, ground photo of soil taken from 1998 and 2018 qualitatively show that the ground ice has vanished (Figure 5.8).

The ground subsidence derived from both ERS-2 and Sentinel-1 InSAR indicates that the ground surface in Bayelva site has undergone long-term subsidence, which coincide with permafrost degradation evidenced from the field measurements. In general, the long-term subsidence trends in permafrost region is related to the loss of the ground ice in the uppermost permafrost which is found in Figure 5.8.

5.5.2 Buildings in Ny-Ålesund village and airport

In general, buildings in permafrost regions are expected to experience limited or no ground subsidence during their service time. Depending on the construction technique, the active layer beneath the building are artificially interfered aiming to keep it neither in frozen state or in thawed state. This is because the thawing and freezing of active layer may introduce seasonal ground subsidence and uplift and consequently damage the above buildings. The observed seasonal subsidence of the buildings in Ny-Ålesund village and airport indicates that the buildings may be unstable. The

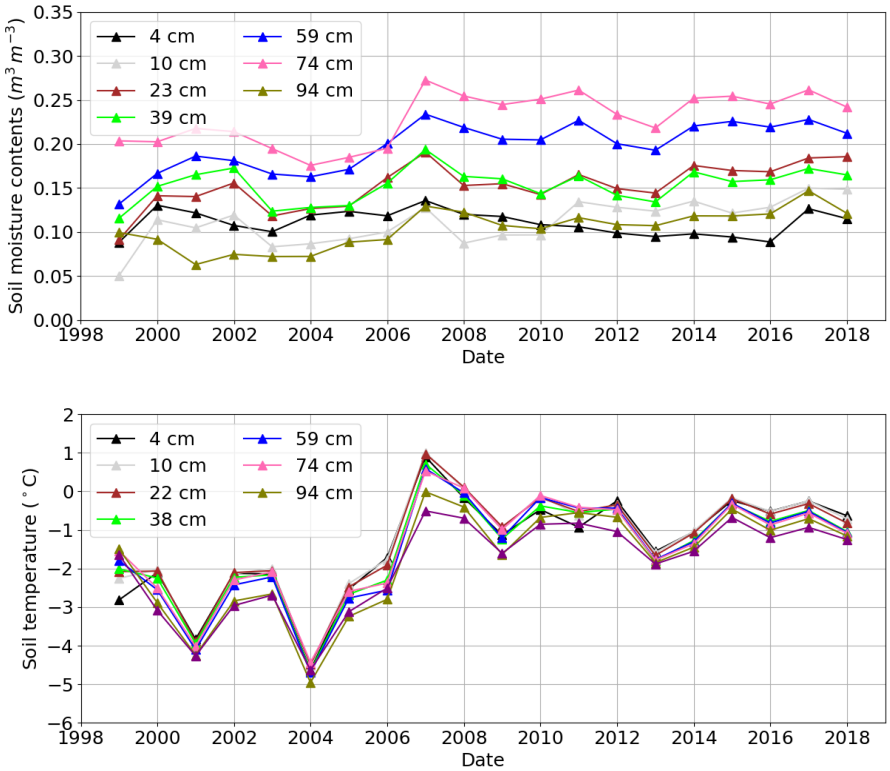

Figure 5.7 (a) Yearly averaged soil moisture; (b) Yearly averaged soil temperature in the active layer at different depth in Bayelva site.

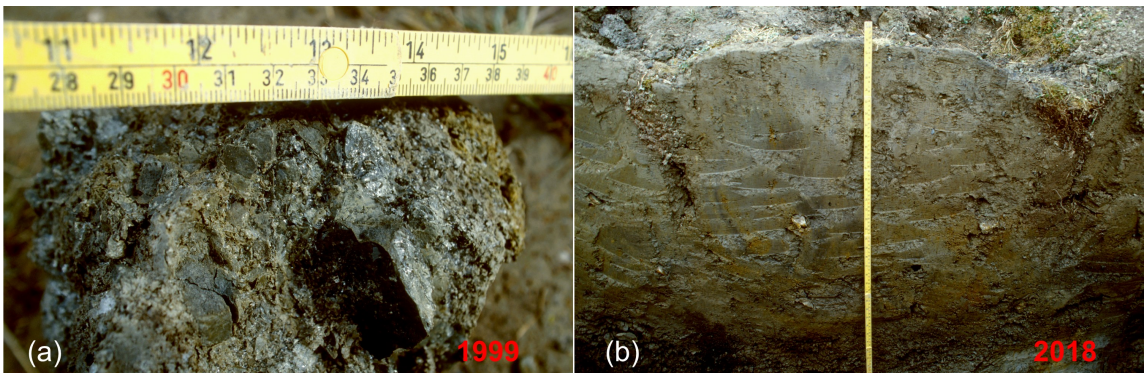

Figure 5.8 Ground photo of soil stratigraphy taken from (a) 1999; (b) 2018 by Dr. Julia Boike (AWI).

sudden noticeable subsidence in the building of mass hall observed in summer of 2018 suggest that this building is more prone to crack or failure.

5.6 Summary and future work

In this study, the long-term subsidence derived from ERS-2 and Sentinel-1 by using hybrid multi-temporal InSAR approaches is reported. During 1995-2009, the accumulated subsidence derived from ERS-2 at the Bayelve site is around 4-6 cm, indicating that the permafrost here is degrading. The field measurements show that the permafrost is warming and the active layer thickness is deepening, which coincided with the InSAR-derived subsidence. Three buildings in Ny-Ålesund village and airport experienced clearly seasonal subsidence during 2015-2018. More specifically, the building of mass hall underwent sudden enlarged subsidence during the summer of 2017 and 2018. However, these are still preliminary results. Further efforts will be focused on:

1. Fill the data gap between 2010 and 2015 (using images taken from space mission such as Radarsat-1/2 and TerraSAR-X) and investigate the combined long-term permafrost thaw subsidence.

   There are archived Radarsat-1/2 and TerraSAR-X SAR data, which can be used to fill the data gap between 2010 and 2015. To study long-term permafrost thaw subsidence, associated with the freeze and thaw cycling processes, it is of importance to understand the response of permafrost to surface disturbance and/or climatic changes. Then, the linkage between ground subsidence and field measurements (such as active layer thickness, soil temperature, and soil temperature) will be investigated.

2. Collect more information to assess the building stabilities

   Several buildings in Ny-Ålesund village and airport seemed to be undergoing unexpected ground subsidence, which may be an indicator of building risks. However, building stabilities in permafrost regions are complicated interactions

among climate impacts, social-cultural practices (such as removal and redistribution of snow, changes of water and sewage systems, infrastructure maintenance), and individual infrastructure status (such as structure, age, and availabilities). The aforementioned information is also important to figure out if the buildings are under risk.

Chapter 6

Soil moisture impacts on InSAR permafrost studies

6.1 Introduction

In **Chapters 3-5**, the applicability of multi-temporal InSAR approaches in permafrost region have been successfully demonstrated. The subsidence maps seem reasonable with accuracy on the order of millimeter to centimeters in local and regional scale. However, the fundamental assumption of interferometric models (see Equation 2.13) is the so-called phase consistency, although researchers tend to not explain it explicitly. Given three spatially averaged interferograms, the phase triplet or closure phase $\phi_{123} = \phi_{12} + \phi_{23} + \phi_{31}$ is consistent only if phase triplet equals to zero. De Zan et al. (2015) systematically introduced the theory and examples of phase inconsistencies, i.e., the closure phase is not equal to zero. In the case of lack of phase consistency, all the interpretation based on the typical InSAR and multi-temporal InSAR results are challenged (De Zan et al., 2015).

An important and common reason for phase inconsistencies is the variations of soil moisture among different SAR acquisitions (De Zan et al., 2014; Zwieback et al., 2015a). In this chapter, I will briefly introduce the microwave dielectric properties of moist soil. Then how the dielectric properties of moist soil affect the interferometric observables (phase, coherence, and phase triplet) will be introduced. I will also show preliminary results on soil moisture effects on multi-temporal InSAR inversion based on phase simulation.

6.2 Microwave dielectric properties of moist soil

Moist soil is a mixture of soil particles, air, and water. Dielectric properties of moist soil are mainly related to the complex dielectric constant (CDC) of each component, their volumetric fractions, their shape and orientation. The underlying assumptions are that all the inclusions are randomly distributed and oriented and their dimensions are much smaller than the radiated wavelength. Due to inconsistent dielectric behavior of soil water, the water contained in the soil medium is usually divided into bound and free water. Bound water is the fraction of water molecules in the first few molecular layers tightly held by the soil particles due to the matric and osmotic forces. Free water refers to the water molecules a few molecular layers away from the soil particles. The amount of bound water is mainly determined by the total surface area of the soil particles. Thus the dielectric constant of moist soil is a dielectric mixture of host dry soil (ϵ_s) and the inclusions of air (ϵ_a), bound water (ϵ_{bw}), and free water (ϵ_{fw}). Theoretically, the soil dielectric model is given by (de Loor, 1968) as:

$$\epsilon_m = \epsilon_s + \sum_{i=bw,fw,a} (\epsilon_i - \epsilon_s) \frac{V_i}{3} \sum_{j=1}^{3} \frac{1}{1 + A_j(\frac{\epsilon_i}{\epsilon^*} - 1)} \tag{6.1}$$

where V is the volume fraction of each inclusions and A refers to the depolarization ellipsoid factor; ϵ^* refers to the effective relative permittivity; $\epsilon_a = 1$. The dielectric constant of dry soil is essentially dependent on soil bulk density but independent of both temperature and frequency. The dielectric constant of pure free water in soil solutions obeys the modified Debye model (Wang, 1980; Dobson et al., 1985).

$$\begin{aligned} \epsilon'_w =& \epsilon_{w0} + \frac{\epsilon_{w0} - \epsilon_{w\infty}}{1 + (2\pi f \tau_w)^2} \\ \epsilon''_w =& \frac{2\pi f \tau_w (\epsilon_{w0} - \epsilon_{w\infty})}{1 + (2\pi f \tau_w)^2} + \frac{\sigma_w}{2\pi f \epsilon_0} \end{aligned} \tag{6.2}$$

where ϵ' and ϵ'' refer to the relative permittivity and loss factor, respectively; $\epsilon_{0/\infty}$ refers to static($f = 0$)/high-frequency($f = \infty$) dielectric constant; τ is the relaxation time (s) and f is the frequency; σ_w is the effective conductivity of water and ϵ_0 is the dielectric constant of free space.

Numerous studies have been conducted to investigate the semi-empirical refractive dielectric mixing model (SRDMM) of moist soil based on a large amount of experimental observations. For the first time, Dobson et al. (1985) proposed a SRDMM as a function of soil moisture and texture at frequencies between 1.4 and 18 GHz by treating the bound water as a distinct component. Dobson's model provide the general ideas for the development of SRDMMs. But, in permafrost regions, the ground surface thaws in summer and freezes in winter, whereas CDCs are also dependent on soil temperature. Mironov et al. (2004) proposed a generalized SRDMM as a function of both temperature and frequency. Mironov et al. (2010) further exploited the SRDMM on temperature ranging from -25 to 30 °C . The temperature-dependent SRDMM is extremely useful in permafrost environment where in winter the ground surface is frozen. More specifically, both the CDCs of mineral and organic soil are also conducted by exploiting the additional soil texture information (Mironov et al., 2017, 2019). Figure 6.1 shows an example of modeled relative permittivity and loss factor by using real soil moisture data.

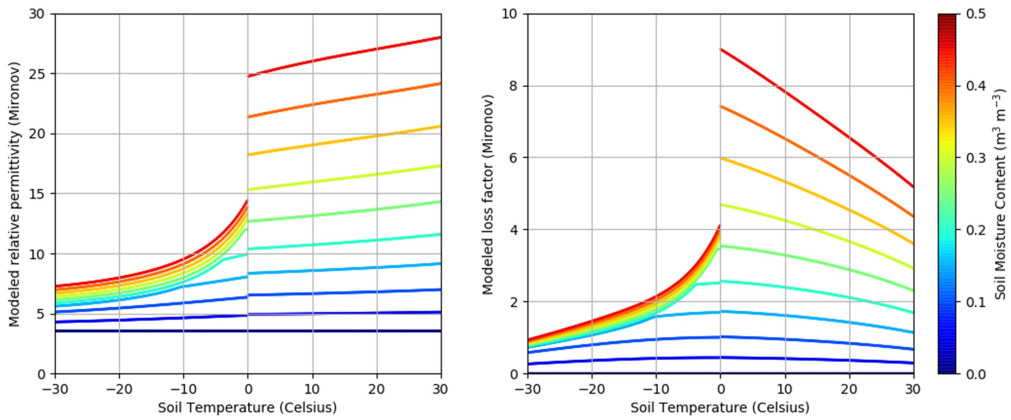

Figure 6.1 Modeled relative permittivity and loss factor by using Mironov's temperature-dependent SRDMM (Mironov et al., 2017)

6.3 Soil moisture impacts on InSAR observables

Soil moisture variation results in the changes of soil dielectric constant and consequently affects the radar backscattered power. To account for the soil moisture impact on InSAR observables, the first-order interferometric model between two acquisitions m and n could be expressed as an integral (De Zan et al., 2014; Zwieback et al., 2015a):

$$\begin{aligned} I(k_{z,m}, k_{z,n}) &= \int_0^\infty f(z) e^{-jk_{z,m}z} (e^{-jk_{z,n}z})^* dz \\ \text{where} \quad k_z(\epsilon) &= \sqrt{\omega^2 \mu \epsilon - k_{air}^2 \sin^2(\theta)} \end{aligned} \tag{6.3}$$

k_z is the vertical wavenumber propagated in soil and $f(z)$ is the vertical scattering profile. ω is the angular frequency, μ is the magnetic permeability and ϵ is the CDCs of moist soil. With the specific assumption $f(z) = 1$, i.e., uniform soil medium, interferometric phase and coherence in terms of soil CDCs can be expressed as (De

Zan et al., 2014):

$$\begin{aligned}\phi(\epsilon^m, \epsilon^s) &= \arg\left(\frac{1}{j(k_z^m(\epsilon^m) - (k_z^s(\epsilon^s))^*)}\right) \\ \gamma(\epsilon^m, \epsilon^s) &= \frac{2\jmath\sqrt{\Im(k_z^m)\Im(k_z^s)}}{(k_z^s(\epsilon^s))^* - k_z^m(\epsilon^m)}\end{aligned} \tag{6.4}$$

where $\Im()$ denotes the image part of a complex number.

Figure 6.2 shows an example of interferometric phase and coherence as a function of the soil moisture content of master and slave SAR images in the case of C-band. Given a fixed soil texture with 51.5% sand and 13.4% clay, the CDCs of moist soil are calculated by using Dobson's SRDMM model (Hallikainen et al., 1985). It is clearly shown that both interferometric phase and coherence are sensitive to soil moisture variation in C-band. It is straightforward to expect that the sensitivity will increase in L-band because of longer wavelength.

Phase triplet has been proposed to retrieve soil moisture, despite still no operational approaches because of the ambiguities in phase triplet (Zwieback et al., 2017; De Zan and Gomba, 2018). But the advantage of phase triplet is obvious: interferometric phase are a mixture of the typical linear phase components (e.g. displacement, atmospheric artifacts, topographic phase); coherence is generally affected by temporal and geometric decorrelation; only phase triplet is intrinsically immune to neither typical linear phase components nor decorrelation. Note that interferometric decorrelation is a proxy of the quality of interferometric phase and thus the phase triplets, which is linear combination of interferometric phase. In other words, decorrelation affects the noise level of phase triplet but not the phase amplitude. De Zan and Gomba (2018) initialized an approximation between phase closure and solely soil moisture content

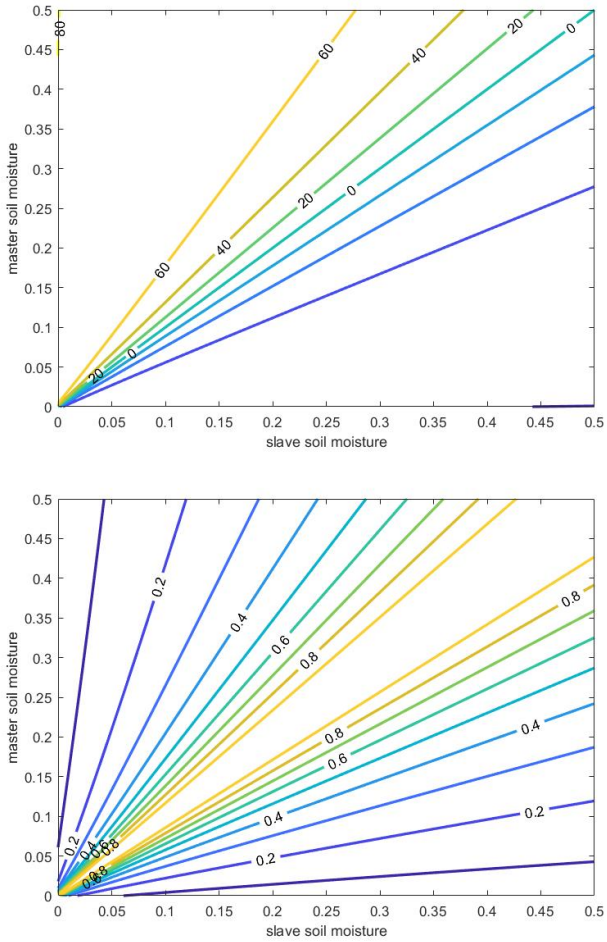

Figure 6.2 Simulated interferometric phase (in degrees) and coherence.

(m) by assuming an exponential scattering profile $(f(z) = e^{-2\alpha}, \alpha > 0)$:

$$\phi_{123} = \phi_{12} + \phi_{23} + \phi_{31} \approx -\alpha^{-3}(m_2 - m_1)(m_3 - m_2)(m_3 - m_1) \tag{6.5}$$

Figure 6.3 shows an example of phase triplets from real Sentinel-1 interferogram stacks in Lena Delta, Siberia. Figure 6.3 (a) shows a case of totally decorrelation which is likely due to the thawing processes. Based on the approximation in Equation 6.5, Figure 6.3 (b-c) shows clearly spatial pattern of moisture variations. In Figure 6.3 (d), there is no clearly moisture affected pattern.

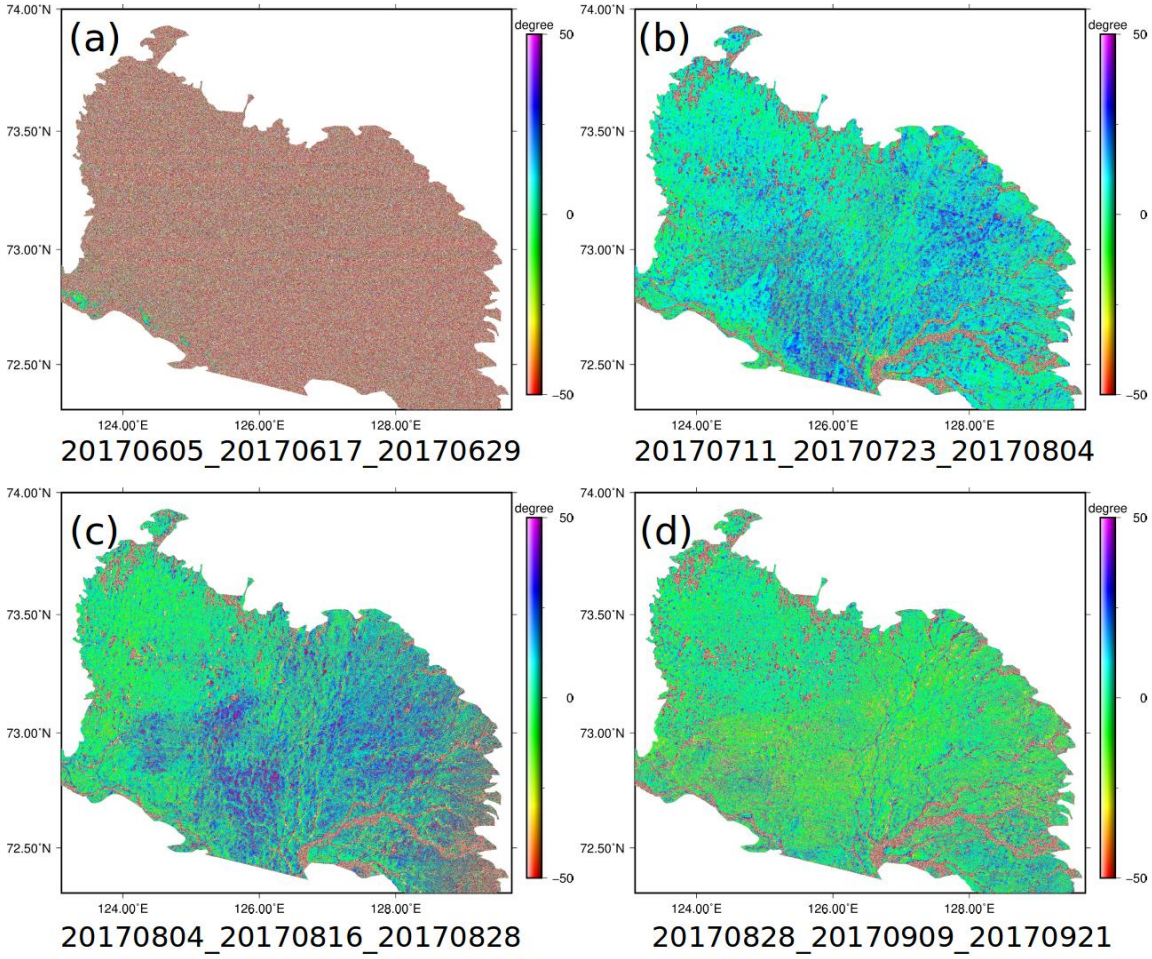

Figure 6.3 Phase triplets calculated from real Sentinel-1 interferogram stacks in Lena Delta, Siberia. The number under each sub-figure denotes the acquisition times (YYYYMMDD) of the three images.

6.4 Soil moisture impacts on multi-temporal InSAR

For conventional PSI approach, there is no multilooking or filtering processes performed on the single-master interferogram stacks. And in general, the selected PS targets are man-made infrastructures (such as building, roads, bridges) or stable natural targets (such as bedrocks) rather than bare soil. In this case, moisture can barely penetrate into the PS targets and thus it is expected that the CDCs of PS targets have no or very limited change in the time domain. In other words, the phase is con-

sistent for an ideal PS target. Therefore, it is expected that soil moisture variations do not affect the conventional PSI approach, which is preferred to be used in urban regions.

For all the SBAS and hybrid multi-temporal InSAR approaches, the multilooked or filtered interferometric phase may not be consistent due to the presence of soil moisture variations. In this case, any phase retrieval or inversion approaches (such as singular-value decomposition, maximum likelihood estimation, integer least squares, eigen-decomposition methods) dependent on linear interferometric model are more or less affected. In principle, if soil moisture variations are highly uncorrelated where subsidence is generally correlated in the time domain, the non-zero phase triplets could be treated as decorrelation noise. In this case, it is expected that soil moisture variations give rise to a certain level of phase uncertainties but no systematic bias. In another case, soil moisture variation may be correlated with subsidence and thus bias the phase. However, due to the highly nonlinear phase model in terms of soil moisture, it is difficult to directly assess the soil moisture impact on subsidence time-series derived from multi-temporal InSAR approaches.

As an alternative, I simulate the interferometric phase associated with real soil moisture data and incorporate it into different frameworks of multi-temporal InSAR processing: single-master and multi-master. Note that I choose to use the temperature-dependent SRDMM model because in permafrost regions the presence of frozen soil makes the CDCs of soil very different from unfrozen soil (Mironov et al., 2017). In Chapter 5, the raw subsidence time-series in Bayelva site (see Figure 5.5(b)) is retrieved by using small-baseline HM-InSAR approaches. A building anchored into deep permafrost is selected as the reference pixel, which is expected to be stable and not affected by moisture variations. For each small-baseline interferogram, the

unwrapped phase is firstly compensated by:

$$\begin{aligned} \phi'_{m,n} =& \phi_{m,n} - \phi_{moisture} \\ \text{where} \quad \phi_{moisture} =& \arg(\frac{1}{2j(k_z^m - (k_z^s)^*)}) \end{aligned} \tag{6.6}$$

$\phi'_{m,n}$ is the corrected phase and could be easily converted to displacement by dividing k_{air}. Then the same L_1-norm minimization is applied to retrieve the displacement time series (SBAS-based correction in Figure 6.4). More details could be found in Chapter 5. To demonstrate the effects of different process strategies, a post-correction is also performed. The calibration is directly conducted on the displacement values relative to a reference time:

$$d''_{ref,n} = d_{ref,n} - \arg(\frac{1}{2j(k_z^{ref} - (k_z^n)^*)})/k_{air} \tag{6.7}$$

$d''_{ref,n}$ is the directly corrected displacement which is similar to the framework of single-master multi-temporal InSAR approaches, referred to as single-based correction in Figure 6.4.

It is clearly shown that a systematic bias (about 5 mm) emerged during the freezing stage of 2017 and 2018 (see the two free red cycles between the raw InSAR time-series and SBAS-based correction in Figure 6.4). Most of the single-based corrections are between the raw InSAR time-series and sbas-based correction. The differences between sbas-based correction and single-based correction indicate that soil moisture effects are nonlinear and rely on construction strategies of interferometric pairs. In both cases, the subsidence time-series might be overestimated. During the freezing stage, soil moisture has an obvious decreasing trend due to the gradual phase transition from liquid water to solid ice within soil medium. This phenomenon is very common in permafrost regions. When the soil gets drier, the interferometric phase

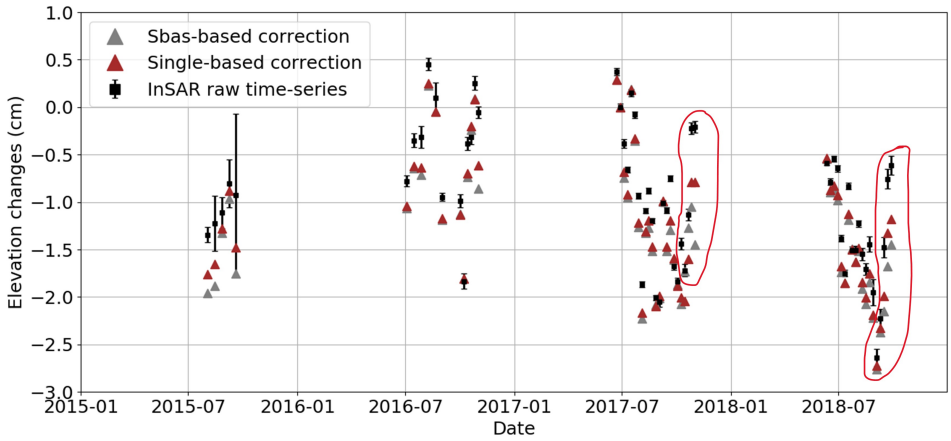

Figure 6.4 InSAR time-series calibration by compensating the simulated soil moisture phase. SBAS-based correction and raw InSAR time-series shows a noticeable bias within the two free red cycles which is mainly occurred during the freezing stage of 2017 and 2018.

acts as spurious "uplift". At the same time, the phase transition from water to ice also give rise to real ground uplift. It is very likely that the two uplift signals are superimposed in the InSAR-derived subsidence time-series or at least in this case study.

6.5 Summary and future work

Soil moisture impacts on InSAR observables and consequent effects on InSAR time-series inversion are illustrated. It is clearly shown that interferometric phase and coherence are sensitive to soil moisture variation even in C-band. Example of phase triplets with clearly spatial patterns have demonstrated the phase inconsistencies rather than the decorrelation noise, which is very likely caused by soil moisture differences.

The results from Chapter 5 are used to illustrate the possible soil moisture effects on

InSAR time-series. Note that in permafrost regions, the complex dielectric constants of moist soil are also dependent on soil temperatures especially when it is close to the freezing/thawing point. Thus, the temperature-dependent refractive dielectric mixing model (Mironov et al., 2017) is used to simulate soil CDCs. Both the calibration before (sbas-based correction) and after (single-based correction) InSAR phase inversion have produced an noticeable systematic bias during the freezing period of 2017 and 2018. It is very likely that the two signals are superimposed in the InSAR-derived subsidence time-series or at least in this case study: one from soil moisture, one from real ground uplift related to freezing processes. Since this phenomena is very common in permafrost regions, this explanation would challenge all the InSAR-based permafrost subsidence studies.

However, there are very few dense soil moisture measurements and continuous elevation change observations in the remote permafrost regions, which makes the assessment of soil moisture effects extremely difficult. Further efforts should be focused on building field observation networks to measure the soil moisture and ground subsidence simultaneously. In this way, fully investigating the soil moisture effects is possible. Then in the next step, it is important to mitigate or separate the soil moisture effects from the InSAR measurements. One possible solution is to isolate soil moisture effects by using the phase triplets which is insensitive to typical linear interferometric models together with amplitude or polarimetric information. Another possible solution is to simulate the soil moisture variation during the thawing and/or freezing stage based on the water and energy balance.

Chapter 7

Conclusions and outlook

7.1 Conclusions

In this thesis, the major work includes: (1) An tailored persistent scatterer InSAR approach to detect detailed thermokarst surface dynamics associated with the gradual permafrost thaw and freeze. (2) The capability of Sentinel-1 InSAR measurements to detect elevation changes over Yedoma uplands on Sobo-Sise Island, Lena Delta. (3) The evidence of permafrost thawing and degradation acquired from both long-term InSAR and ground measurements. (4) The illustration of soil moisture impacts on InSAR measurements in permafrost regions. In total, I demonstrate that InSAR is a useful technique to measure the historical permafrost thaw subsidence and freeze uplift both in Tibet and Arctic.

In **Chapters 3-5**, three case studies, one in Tibet and two in Arctic, are performed to map and quantify permafrost thaw subsidence by using multi-temporal InSAR approaches. Despite these case studies are conducted at different locations and different time periods, the subsidence trends and/or seasonal subsidence are all on the order of millimeter to centimeters. Due to different permafrost environments and research objectives, different multi-temporal InSAR approaches are developed: In **Chapter 3**, persistent scatterer InSAR is adopted to detect the detailed gully features under the condition of shallow snow and vegetation cover in local scale; In **Chapter 4**, conventional small-baseline InSAR is used to monitor large-scale permafrost thaw

subsidence without concerning local details; In **Chapter 5**, a hybrid multi-temporal InSAR is developed to detect the surface subsidence and the displacement of above buildings. In general, strong temporal surface processes (such as heave snowfall, vegetation succession, strong variation of surface soil moisture) introduces significant temporal interferometric decorrelation. Depending on the degree of surface processes and measuring targets (such as, natural ground, infrastructures, with/without vegetation cover), different multi-temporal InSAR could be selected.

The major findings of this thesis are: (1) The gradual permafrost thaw subsidence occurs both inside and around the thermal erosion gullies in an area located on Ebling Mountain between 2006 and 2011. The subsidence trends are up to 3 cm/year inside and around the thermal erosion gullies, suggesting that 28% of the study area experiences permafrost thaw processes, which is about 40 times larger than the visible gullies. The spatial pattern of gradual subsidence trends shows correlations between the gullies and their surroundings, suggesting that the permafrost thaws and degrades in a wider region than the gullies. (2) The highest flat Yedoma uplands, i.e., the undisturbed regions, present the highest seasonal thaw subsidence. While the active layer thickness does not significantly vary among the Yedoma uplands, the highest subsidence amplitudes over the top of Yedoma uplands suggest higher water/ice contents than in lower regions. Benefiting from the Sentinel-1 InSAR measurements with short time intervals (12 days in this case), I found that delayed thawing associated with air temperature fluctuations affects inter-annual elevation changes. (3) In the preliminary study of permafrost thaw dynamics in Svalbard, the long-term InSAR as well as the field measurements, such as permafrost temperature and thaw depth are all in wetness of local permafrost degradation. (4) Soil moisture impacts on InSAR time-series inversion might be noticeable and significant in permafrost regions. This is mainly related to the particular temporal pattern of soil moisture content associ-

ated with the freeze and thaw, which is very common in permafrost regions. It is very likely that soil moisture biases the InSAR-derived subsidence time-series during the freezing and thawing of the uppermost active layer. This explanation would challenge all the InSAR-based permafrost subsidence studies.

7.2 Outlook

7.2.1 Advance permafrost thaw subsidence model

In this thesis, the seasonal and linear subsidence trends is used to represent the ground elevation changes in permafrost regions. The seasonal subsidence and uplift is assumed to be solely related to the phase change between pore water and ice. The contribution from segregated ice within active layer is ignored. In the case of that the segregated ice dominates the ground elevation changes, the model proposed in this thesis might be failed. Thus, future efforts should be made on the understanding of permafrost elevation changes by considering both pore and segregated ice. Continuous field observation networks to simultaneously measure the ice dynamics in the active layer, elevation changes, soil conditions is necessary. On the other hand, the variations of active layer thickness make the subsidence model more complicated. By further understanding the dynamic processes of active layer and permafrost, there are opportunities to advance the elevation change models.

7.2.2 Integrate abrupt and gradual permafrost thaw subsidence

The capabilities of InSAR for detecting gradual permafrost thaw subsidence have been demonstrated in this thesis. In general, those targets in SAR images, which undergo abrupt subsidence, are always masked out. Differential digital elevation models (DEMs) generated from stereographic images (Lantuit and Pollard, 2005; Günther

et al., 2015), LiDAR (Jones et al., 2013; Obu et al., 2017) and Single-pass InSAR (Zwieback et al., 2018) have been successfully used to measure the abrupt thaw subsidence. By integrating abrupt and gradual permafrost thaw subsidence, we can have a more accurate estimation of permafrost ice loss under climate warming. However, the accuracy of abrupt subsidence is normally on the order of sub-meters, while the amplitude of gradual thaw subsidence is about millimeters to centimeters. In addition, abrupt subsidence is likely to occur at daily or monthly scale, while the gradual subsidence would be likely at annual or decadal scale. Thus, it is very challenging to combine the abrupt and gradual thaw subsidence from different temporal and spatial scales.

Bibliography

Adam, N., Kampes, B., Eineder, M., 2004. Development of a scientific permanent scatterer system: Modifications for mixed ERS/ENVISAT time series, in: Proceedings of the 2004 Envisat & ERS Symposium.

Agram, P.S., Jolivet, R., Simons, M., 2012. The Generic InSAR Analysis Toolbox (GIAnT) - User Guide, in: AGU Fall Meeting Abstracts, p. 0897.

Antonova, S., Kääb, A., Heim, B., Langer, M., Boike, J., 2016. Spatio-temporal variability of X-band radar backscatter and coherence over the Lena River Delta, Siberia. Remote Sensing of Environment 182, 169–191. doi:10.1016/j.rse.2016.05.003.

Antonova, S., Sudhaus, H., Strozzi, T., Zwieback, S., Kääb, A., Heim, B., Langer, M., Bornemann, N., Boike, J., 2018. Thaw Subsidence of a Yedoma Landscape in Northern Siberia, Measured In Situ and Estimated from TerraSAR-X Interferometry. Remote Sensing 10, 494. doi:10.3390/rs10040494.

Bamler, R., Hartl, P., 1998. Synthetic aperture radar interferometry. Inverse problems 14, R1.

Bamler, R., Just, D., 1993. Phase statistics and decorrelation in SAR interferograms. International Geoscience & Remote Sensing Symposium. IEEE. .

Bao, X., Zhang, F., 2013. Evaluation of NCEP–CFSR, NCEP–NCAR, ERA-Interim, and ERA-40 Reanalysis Datasets against Independent Sounding Observations over the Tibetan Plateau. Journal of Climate 26, 206–214. doi:10.1175/jcli-d-12-00056.1.

Bell, J.W., Amelung, F., Ferretti, A., Bianchi, M., Novali, F., 2008. Permanent scatterer In-

SAR reveals seasonal and long term aquifer system response to groundwater pumping and artificial recharge. Water Resources Research 44, W02407. doi:10.1029/2007WR006152.

Berardino, P., Fornaro, G., Lanari, R., Sansosti, E., 2002. A new algorithm for surface deformation monitoring based on small baseline differential SAR interferograms. Geoscience and Remote Sensing, IEEE Transactions on 40, 2375–2383. doi:10.1109/TGRS.2002.803792.

de Berg, M., Cheong, O., van Kreveld, M., Overmars, M., 2008. Computational Geometry: Algorithms and Applications. Springer Science & Business Media. doi:10.1007/978-3-662-03427-9.

Biggs, J., Wright, T., Lu, Z., Parsons, B., 2007. Multi-interferogram method for measuring interseismic deformation: Denali Fault, Alaska. Geophysical Journal International 170, 1165–1179. doi:10.1111/j.1365-246X.2007.03415.x.

Biskaborn, B.K., Smith, S.L., Noetzli, J., Matthes, H., Vieira, G., Streletskiy, D.A., Schoeneich, P., Romanovsky, V.E., Lewkowicz, A.G., Abramov, A., Allard, M., Boike, J., Cable, W.L., Christiansen, H.H., Delaloye, R., Diekmann, B., Drozdov, D., Etzelmüller, B., Grosse, G., Guglielmin, M., Ingeman-Nielsen, T., Isaksen, K., Ishikawa, M., Johansson, M., Johannsson, H., Joo, A., Kaverin, D., Kholodov, A., Konstantinov, P., Kröger, T., Lambiel, C., Lanckman, J.P., Luo, D., Malkova, G., Meiklejohn, I., Moskalenko, N., Oliva, M., Phillips, M., Ramos, M., Sannel, A.B.K., Sergeev, D., Seybold, C., Skryabin, P., Vasiliev, A., Wu, Q., Yoshikawa, K., Zheleznyak, M., Lantuit, H., 2019. Permafrost is warming at a global scale. Nature Communications 10, 264. doi:10.1038/s41467-018-08240-4.

Boike, J., Ebenhoch, S., Höfle, B., Westermann, S., Maturilli, M., Stern, L., Juszak, I. and Roth, K., 2018a. Warming trends in Permafrost and thermo-insulation effect of a seasonal snow-cover on permafrost soil in Bayelva, Svalbard (1998 - 2017), in: EGU General Assembly 2018, Vienna, Austria.

Boike, J., Juszak, I., Lange, S., Chadburn, S., Burke, E., Overduin, P.P., Roth, K., Ippisch, O., Bornemann, N., Stern, L., Gouttevin, I., Hauber, E., Westermann, S., 2018b. A 20-year record (1998-2017) of permafrost, active layer and meteorological conditions at a high Arctic permafrost research site (Bayelva, Spitsbergen). Earth System Science Data 10, 355–390. doi:10.5194/essd-10-355-2018.

Boike, J., Kattenstroth, B., Abramova, K., Bornemann, N., Chetverova, A., Fedorova, I., Fröb, K., Grigoriev, M., Grüber, M., Kutzbach, L., Langer, M., Minke, M., Muster, S., Piel, K., Pfeiffer, E.M.M., Stoof, G., Westermann, S., Wischnewski, K., Wille, C., Hubberten, H.W.W., 2013. Baseline characteristics of climate, permafrost and land cover from a new permafrost observatory in the Lena River Delta, Siberia (1998-2011). Biogeosciences 10, 2105–2128. doi:10.5194/bg-10-2105-2013.

Cao, B., Gruber, S., Zhang, T., Li, L., Peng, X., Wang, K., Zheng, L., Shao, W., Guo, H., 2017. Spatial variability of active layer thickness detected by ground-penetrating radar in the Qilian Mountains, Western China. Journal of Geophysical Research: Earth Surface 122, 574–591. doi:10.1002/2016JF004018.

Cao, B., Zhang, T., Peng, X., Mu, C., Wang, Q., Zheng, L., Wang, K., Zhong, X., 2018. Thermal Characteristics and Recent Changes of Permafrost in the Upper Reaches of the Heihe River Basin, Western China. Journal of Geophysical Research: Atmospheres 123, 7935–7949. doi:10.1029/2018JD028442.

Chen, C.W., 2001. Statistical-Cost Network-Flow Approaches to Two-Dimensional Phase Unwrapping for Radar Interferometry. Ph.D. thesis. Stanford University.

Chen, C.W., Zebker, H.A., 2001. Two-dimensional phase unwrapping with use of statistical models for cost functions in nonlinear optimization. Journal of the Optical Society of America A 18, 338–351. doi:10.1364/JOSAA.18.000338.

Cheng, G., Wu, T., 2007. Responses of permafrost to climate change and their environmen-

tal significance, Qinghai-Tibet Plateau. Journal of Geophysical Research: Earth Surface 112, F02S03. doi:10.1029/2006JF000631.

Christiansen, H.H., Etzelmüller, B., Isaksen, K., Juliussen, H., Farbrot, H., Humlum, O., Johansson, M., Ingeman-Nielsen, T., Kristensen, L., Hjort, J., Holmlund, P., Sannel, A.B.K., Sigsgaard, C., Åkerman, H.J., Foged, N., Blikra, L.H., Pernosky, M.A., Ødegård, R.S., 2010. The thermal state of permafrost in the nordic area during the international polar year 2007-2009. Permafrost and Periglacial Processes 21, 156–181. doi:10.1002/ppp.687.

Ciampalini, A., Raspini, F., Lagomarsino, D., Catani, F., Casagli, N., 2016. Landslide susceptibility map refinement using PSInSAR data. Remote Sensing of Environment 184, 302–315. doi:10.1016/j.rse.2016.07.018.

Colesanti, C., Ferretti, A., Novali, F., Prati, C., Rocca, F., 2003a. SAR monitoring of progressive and seasonal ground deformation using the permanent scatterers technique. Geoscience and Remote Sensing, IEEE Transactions on 41, 1685–1701. doi:10.1109/Tgrs.2003.813278.

Colesanti, C., Ferretti, A., Prati, C., Rocca, F., 2003b. Monitoring landslides and tectonic motions with the Permanent Scatterers Technique. Engineering Geology 68, 3–14. doi:10.1016/S0013-7952(02)00195-3.

Costantini, M., 1998. A novel phase unwrapping method based on network programming. IEEE Transactions on Geoscience and Remote Sensing 36, 813–821. doi:10.1109/36.673674.

Costantini, M., Falco, S., Malvarosa, F., Minati, F., Trillo, F., Vecchioli, F., 2014. Persistent Scatterer Pair Interferometry: Approach and Application to COSMO-SkyMed SAR Data. IEEE Journal of Selected Topics in Applied Earth Observations and Remote Sensing 7, 2869–2879. doi:10.1109/JSTARS.2014.2343915.

Crosetto, M., Monserrat, O., Cuevas-González, M., Devanthéry, N., Crippa, B., 2016. Persistent Scatterer Interferometry: A review. ISPRS Journal of Photogrammetry and Remote Sensing 115, 78–89. doi:10.1016/j.isprsjprs.2015.10.011.

Crosetto, M., Monserrat, O., Cuevas-González, M., Devanthéry, N., Luzi, G., Crippa, B., 2015. Measuring thermal expansion using X-band persistent scatterer interferometry. ISPRS Journal of Photogrammetry and Remote Sensing 100, 84–91. doi:10.1016/J.ISPRSJPRS.2014.05.006.

Daout, S., Doin, M.P., Peltzer, G., Socquet, A., Lasserre, C., 2017. Large-scale InSAR monitoring of permafrost freeze-thaw cycles on the Tibetan Plateau. Geophysical Research Letters 44, 901–909. doi:10.1002/2016GL070781.

De Zan, F., Gomba, G., 2018. Vegetation and soil moisture inversion from SAR closure phases: First experiments and results. Remote Sensing of Environment 217, 562–572. doi:10.1016/j.rse.2018.08.034.

De Zan, F., Monti Guarnieri, A., 2006. TOPSAR: Terrain Observation by Progressive Scans. Geoscience and Remote Sensing, IEEE Transactions on 44, 2352–2360. doi:10.1109/TGRS.2006.873853.

De Zan, F., Parizzi, A., Prats-Iraola, P., López-Dekker, P., 2014. A SAR interferometric model for soil moisture. IEEE Transactions on Geoscience and Remote Sensing 52, 418–425. doi:10.1109/TGRS.2013.2241069.

De Zan, F., Zonno, M., Paco, L.D., 2015. Phase Inconsistencies and Multiple Scattering in SAR Interferometry. IEEE Transactions on Geoscience and Remote Sensing 53, 6608–6616. doi:10.1109/TGRS.2015.2444431.

Dobson, M.C., Ulaby, F.T., Hallikainen, M.T., El-rayes, M.A., 1985. Microwave Dielectric Behavior of Wet Soil-Part II: Dielectric Mixing Models. IEEE Transactions on Geoscience and Remote Sensing GE-23, 35–46. doi:10.1109/TGRS.1985.289498.

van Everdingen, R.O., 1998. Multi-language Glossary of Permafrost and Related Ground-ice Terms. National Snow and Ice Data Center, Boulder, Colorado.

Fattahi, H., Simons, M., Agram, P., 2017. InSAR Time-Series Estimation of the Ionospheric Phase Delay: An Extension of the Split Range-Spectrum Technique. IEEE Transactions on Geoscience and Remote Sensing 55, 5984–5996. doi:10.1109/TGRS.2017.2718566.

Ferretti, A., Fumagalli, A., Novali, F., Prati, C., Rocca, F., Rucci, A., 2011. A new algorithm for processing interferometric data-stacks: SqueeSAR. Geoscience and Remote Sensing, IEEE Transactions on 49, 3460–3470. doi:10.1109/TGRS.2011.2124465.

Ferretti, A., Prati, C., Rocca, F., 1999a. Multibaseline InSAR DEM reconstruction: the wavelet approach. Geoscience and Remote Sensing, IEEE Transactions on 37, 705–715. doi:10.1109/36.752187.

Ferretti, A., Prati, C., Rocca, F., 2000. Nonlinear subsidence rate estimation using permanent scatterers in differential SAR interferometry. Geoscience and Remote Sensing, IEEE Transactions on 38, 2202–2212. doi:10.1109/36.868878.

Ferretti, A., Prati, C., Rocca, F., 2001. Permanent scatterers in SAR interferometry. Geoscience and Remote Sensing, IEEE Transactions on 39, 8–20. doi:10.1109/36.898661.

Ferretti, A., Prati, C., Rocca, F.L., 1999b. Permanent scatterers in SAR interferometry, in: IEEE 1999 International Geoscience and Remote Sensing Symposium, pp. 1528–1530.

Ferretti, A., Savio, G., Barzaghi, R., Borghi, A., Musazzi, S., Novali, F., Prati, C., Rocca, F., 2007. Submillimeter Accuracy of InSAR Time Series: Experimental Validation. Geoscience and Remote Sensing, IEEE Transactions on 45, 1142–1153. doi:10.1109/TGRS.2007.894440.

Fiddes, J., Endrizzi, S., Gruber, S., 2015. Large-area land surface simulations in heterogeneous terrain driven by global data sets: application to mountain permafrost. The Cryosphere 9, 411–426. doi:10.5194/tc-9-411-2015.

Fong, D.C.L., Saunders, M., 2011. LSMR: An Iterative Algorithm for Sparse Least-Squares Problems. SIAM Journal on Scientific Computing 33, 2950–2971. doi:10.1137/10079687X.

Fornaro, G., Reale, D., Verde, S., 2012. Adaptive spatial multilooking and temporal multilinking in SBAS Interferometry, in: Geoscience and Remote Sensing Symposium (IGARSS), 2012 IEEE International, pp. 1892–1895. doi:10.1109/IGARSS.2012.6351137.

Fornaro, G., Verde, S., Reale, D., Pauciullo, A., 2015. CAESAR: An Approach Based on Covariance Matrix Decomposition to Improve Multibaseline-Multitemporal Interferometric SAR Processing. Geoscience and Remote Sensing, IEEE Transactions on 53, 2050–2065. doi:10.1109/TGRS.2014.2352853.

French, H.M., 2007. The periglacial environment. John Wiley & Sons.

Fuchs, M., Grosse, G., Strauss, J., Günther, F., Grigoriev, M., Maximov, G.M., Hugelius, G., 2018. Carbon and nitrogen pools in thermokarst-affected permafrost landscapes in Arctic Siberia. Biogeosciences 15, 953–971. doi:10.5194/bg-15-953-2018.

Gernhardt, S., Adam, N., Eineder, M., Bamler, R., 2010. Potential of very high resolution SAR for persistent scatterer interferometry in urban areas. Annals of GIS 16, 103–111. doi:10.1080/19475683.2010.492126.

Goel, K., Adam, N., 2012. An advanced algorithm for deformation estimation in non-urban areas. ISPRS Journal of Photogrammetry and Remote Sensing 73, 100–110. doi:10.1016/j.isprsjprs.2012.06.001.

Gomba, G., Parizzi, A., De Zan, F., Eineder, M., Bamler, R., 2016. Toward Operational Compensation of Ionospheric Effects in SAR Interferograms: The Split-Spectrum Method. IEEE Transactions on Geoscience and Remote Sensing 54, 1446–1461. doi:10.1109/TGRS.2015.2481079.

Grosse, G., Harden, J., Turetsky, M., McGuire, A.D., Camill, P., Tarnocai, C., Frolking, S., Schuur, E.A.G., Jorgenson, M.T., Marchenko, S., Romanovsky, V., Wickland, K.P., French, N., Waldrop, M., Bourgeau-Chavez, L., Striegl, R.G., 2011. Vulnerability of high-latitude soil organic carbon in North America to disturbance. Journal of Geophysical Research: Biogeosciences 116. doi:10.1029/2010JG001507.

Guarnieri, A.M., Tebaldini, S., 2008. On the exploitation of target statistics for SAR interferometry applications. Geoscience and Remote Sensing, IEEE Transactions on 46, 3436–3443. doi:10.1109/TGRS.2008.2001756.

Günther, F., Overduin, P.P., Yakshina, I.A., Opel, T., Baranskaya, A.V., Grigoriev, M.N., 2015. Observing Muostakh disappear: permafrost thaw subsidence and erosion of a ground-ice-rich island in response to arctic summer warming and sea ice reduction. The Cryosphere 9, 151–178. doi:10.5194/tc-9-151-2015.

Hallikainen, M.T., Ulaby, F.T., Dobson, M.C., El-rayes, M.A., Wu, L.k., 1985. Microwave Dielectric Behavior of Wet Soil-Part 1: Empirical Models and Experimental Observations. IEEE Transactions on Geoscience and Remote Sensing GE-23, 25–34. doi:10.1109/TGRS.1985.289497.

Hanssen, R.F., 2001. Radar interferometry: data interpretation and error analysis. volume 2. Springer.

Hilley, G.E., Bürgmann, R., Ferretti, A., Novali, F., Rocca, F., 2004. Dynamics of slow-moving landslides from permanent scatterer analysis. Science 304, 1952–1955. doi:10.1126/science.1098821.

Hjort, J., Karjalainen, O., Aalto, J., Westermann, S., Romanovsky, V.E., Nelson, F.E., Etzelmüller, B., Luoto, M., 2018. Degrading permafrost puts Arctic infrastructure at risk by mid-century. Nature Communications 9, 5147. doi:10.1038/s41467-018-07557-4.

Hooper, A., Prata, F., Sigmundsson, F., 2012. Remote sensing of volcanic hazards and their precursors. Proceedings of the IEEE 100, 2908–2930. doi:10.1109/JPROC.2012.2199269.

Hooper, A., Zebker, H., Segall, P., Kampes, B., 2004. A new method for measuring deformation on volcanoes and other natural terrains using InSAR persistent scatterers. Geophysical Research Letters 31. doi:10.1029/2004GL021737.

Hu, Y., Liu, L., Larson, K.M., Schaefer, K.M., Zhang, J., Yao, Y., 2018. GPS Interferometric Reflectometry Reveals Cyclic Elevation Changes in Thaw and Freezing Seasons in a Permafrost Area (Barrow, Alaska). Geophysical Research Letters 45, 5581–5589. doi:10.1029/2018GL077960.

Hugelius, G., Strauss, J., Zubrzycki, S., Harden, J.W., Schuur, E.A.G., Ping, C.L., Schirrmeister, L., Grosse, G., Michaelson, G.J., Koven, C.D., O'Donnell, J.A., Elberling, B., Mishra, U., Camill, P., Yu, Z., Palmtag, J., Kuhry, P., 2014. Estimated stocks of circumpolar permafrost carbon with quantified uncertainty ranges and identified data gaps. Biogeosciences 11, 6573–6593. doi:10.5194/bg-11-6573-2014.

Humlum, O., 2005. Holocene permafrost aggradation in Svalbard. Geological Society, London, Special Publications 242, 119–129. doi:10.1144/GSL.SP.2005.242.01.11.

Humlum, O., Instanes, A., Sollid, J.L., 2003. Permafrost in Svalbard: a review of research history, climatic background and engineering challenges. Polar Research 22, 191–215. doi:10.3402/polar.v22i2.6455.

Instanes, A., 2003. Climate change and possible impact on Arctic infrastructure, in: Proceedings 8th International Permafrost Conference, Zürich, Switzerland.

Jiang, M., Ding, X., Hanssen, R.F., Malhotra, R., Chang, L., 2015. Fast Statistically Homogeneous Pixel Selection for Covariance Matrix Estimation for Multitemporal InSAR. Geoscience and Remote Sensing, IEEE Transactions on 53, 1213–1224. doi:10.1109/TGRS.2014.2336237.

Jin, H., Luo, D., Wang, S., Lü, L., Wu, J., 2011. Spatiotemporal variability of permafrost degradation on the Qinghai-Tibet Plateau. Sciences in Cold and Arid Regions 3, 281–305. doi:10.3724/SP.J.1226.2011.00281.

Jones, B.M., Grosse, G., Arp, C.D., Miller, E., Liu, L., Hayes, D.J., Larsen, C.F., 2015. Recent Arctic tundra fire initiates widespread thermokarst development. Scientific Reports 5, 15865. doi:10.1038/srep15865.

Jones, B.M., Stoker M., J., Gibbs, A.E., Grosse, G., Romanovsky, V.E., Thomas, A.D., Nicole, E.M.K., Bruce, M.R., 2013. Quantifying landscape change in an arctic coastal lowland using repeat airborne LiDAR. Environmental Research Letters 8, 45025. doi:10.1088/1748-9326/8/4/045025.

Jorgenson, M.T., 2013. Thermokarst Terrains, in: Shroder, J.F. (Ed.), Treatise on Geomorphology. Academic Press, San Diego, pp. 313–324. doi:10.1016/B978-0-12-374739-6.00215-3.

Jorgenson, M.T., Osterkamp, T.E., 2005. Response of boreal ecosystems to varying modes of permafrost degradation. Canadian Journal of Forest Research 35, 2100–2111. doi:10.1139/x05-153.

Kääb, A., 2002. Monitoring high-mountain terrain deformation from repeated air- and spaceborne optical data: examples using digital aerial imagery and ASTER data. ISPRS Journal of Photogrammetry and Remote Sensing 57, 39–52. doi:10.1016/S0924-2716(02)00114-4.

Kampes, B.M., Hanssen, R.F., 2004. Ambiguity resolution for permanent scatterer interferometry. Geoscience and Remote Sensing, IEEE Transactions on 42, 2446–2453. doi:10.1109/TGRS.2004.835222.

Kokelj, S.V., Jorgenson, M.T., 2013. Advances in Thermokarst Research. Permafrost and Periglacial Processes 24, 108–119. doi:10.1002/ppp.1779.

Koven, C.D., Ringeval, B., Friedlingstein, P., Ciais, P., Cadule, P., Khvorostyanov, D., Krinner, G., Tarnocai, C., 2011. Permafrost carbon-climate feedbacks accelerate global warming. Proceedings of the National Academy of Sciences 108, 14769–14774. doi:10.1073/pnas.1103910108.

Kvam, P.H., Vidakovic, B., 2007. Nonparametric Statistics with Applications to Science and Engineering. Wiley Series in Probability and Statistics, John Wiley & Sons, Inc., Hoboken, NJ, USA. doi:10.1002/9780470168707.

Lanari, R., Mora, O., Manunta, M., Mallorqui, J.J., Berardino, P., Sansosti, E., 2004. A small-baseline approach for investigating deformations on full-resolution differential SAR interferograms. Geoscience and Remote Sensing, IEEE Transactions on 42, 1377–1386. doi:10.1109/TGRS.2004.828196.

Lantuit, H., Overduin, P.P., Wetterich, S., 2013. Recent Progress Regarding Permafrost Coasts. Permafrost and Periglacial Processes 24, 120–130. doi:10.1002/ppp.1777.

Lantuit, H., Pollard, W.H., 2005. Temporal stereophotogrammetric analysis of retrogressive thaw slumps on Herschel Island, Yukon territory. Natural Hazards and Earth System Sciences 5, 413–423. doi:10.5194/nhess-5-413-2005.

Lauknes, T.R., Zebker, H.A., Larsen, Y., 2011. InSAR Deformation Time Series Using L1-Norm Small-Baseline Approach. Geoscience and Remote Sensing, IEEE Transactions on 49, 536–546. doi:10.1109/TGRS.2010.2051951.

Liljedahl, A.K., Boike, J., Daanen, R.P., Fedorov, A.N., Frost, G.V., Grosse, G., Hinzman, L.D., Iijma, Y., Jorgenson, J.C., Matveyeva, N., Necsoiu, M., Raynolds, M.K., Romanovsky, V.E., Schulla, J., Tape, K.D., Walker, D.A., Wilson, C.J., Yabuki, H., Zona, D., 2016. Pan-Arctic ice-wedge degradation in warming permafrost and its influence on tundra hydrology. Nature Geoscience advance on. doi:10.1038/ngeo2674.

Lin, H., Li, G., Cuo, L., Hooper, A., Ye, Q., 2017. A decreasing glacier mass balance gradient from the edge of the Upper Tarim Basin to the Karakoram during 2000–2014. Scientific Reports 7, 6712. doi:10.1038/s41598-017-07133-8.

Little, J.D., Sandall, H., Walegur, M.T., Nelson, F.E., 2003. Application of differential global positioning systems to monitor frost heave and thaw settlement in tundra environments. Permafrost and Periglacial Processes 14, 349–357. doi:10.1002/ppp.466.

Liu, L., Larson, K.M., 2018. Decadal changes of surface elevation over permafrost area estimated using reflected GPS signals. The Cryosphere 12, 477–489. doi:10.5194/tc-12-477-2018.

Liu, L., Schaefer, K., Gusmeroli, A., Grosse, G., Jones, B.M., Zhang, T., Parsekian, A.D., Zebker, H.A., 2014. Seasonal thaw settlement at drained thermokarst lake basins, Arctic Alaska. The Cryosphere 8, 815–826. doi:10.5194/tc-8-815-2014.

Liu, L., Schaefer, K., Zhang, T., Wahr, J., 2012. Estimating 1992–2000 average active layer thickness on the Alaskan North Slope from remotely sensed surface subsidence. Journal of Geophysical Research: Earth Surface (2003–2012) 117. doi:10.1029/2011JF002041.

Liu, L., Schaefer, K.M., Chen, A.C., Gusmeroli, A., Zebker, H.A., Zhang, T., 2015. Remote sensing measurements of thermokarst subsidence using InSAR. Journal of Geophysical Research: Earth Surface 120, 1935–1948. doi:10.1002/2015JF003599.

Liu, L., Zhang, T., Wahr, J., 2010. InSAR measurements of surface deformation over permafrost on the North Slope of Alaska. Journal of Geophysical Research: Earth Surface 115. doi:10.1029/2009JF001547.

de Loor, G.P., 1968. Dielectric Properties of Heterogeneous Mixtures Containing Water. Journal of Microwave Power 3, 67–73. doi:10.1080/00222739.1968.11688670.

Lunardini, V., 1978. Theory of n-factors and correlation of data, in: Proceedings of the Third International Conference on Permafrost, National Research Council of Canada Ottawa. pp. 40–46.

Luo, L., Ma, W., Zhang, Z., Zhuang, Y., Zhang, Y., Yang, J., Cao, X., Liang, S., Mu, Y., 2017. Freeze/Thaw-Induced Deformation Monitoring and Assessment of the Slope in Permafrost Based on Terrestrial Laser Scanner and GNSS. Remote Sensing 9, 198. doi:10.3390/rs9030198.

MacDougall, A.H., Avis, C.A., Weaver, A.J., 2012. Significant contribution to climate warming from the permafrost carbon feedback. Nature Geoscience 5, 719–721. doi:10.1038/ngeo1573.

Mackay, J.R., 1973a. A Frost Tube for the Determination of Freezing in the Active Layer above Permafrost. Canadian Geotechnical Journal 10, 392–396. doi:10.1139/t73-033.

Mackay, J.R., 1973b. The Growth of Pingos, Western Arctic Coast, Canada. Canadian Journal of Earth Sciences 10, 979–1004. doi:10.1139/e73-086.

Mackay, J.R., 1983. Downward water movement into frozen ground, western arctic coast, Canada. Canadian Journal of Earth Sciences 20, 120–134. doi:10.1139/e83-012.

Mackay, J.R., Burn, C.R., 2002. The first 20 years (1978-1979 to 1998-1999) of active-layer development, Illisarvik experimental drained lake site, western Arctic coast, Canada. Canadian Journal of Earth Sciences 39, 1657–1674. doi:10.1139/e02-068.

Melvin, A.M., Larsen, P., Boehlert, B., Neumann, J.E., Chinowsky, P., Espinet, X., Martinich, J., Baumann, M.S., Rennels, L., Bothner, A., Nicolsky, D.J., Marchenko, S.S., 2017. Climate change damages to Alaska public infrastructure and the economics of proactive adaptation. Proceedings of the National Academy of Sciences of the United States of America 114, E122–E131. doi:10.1073/pnas.1611056113.

Mironov, V.L., De Roo, R.D., Savin, I.V., 2010. Temperature-Dependable Microwave Dielectric Model for an Arctic Soil. IEEE Transactions on Geoscience and Remote Sensing 48, 2544–2556. doi:10.1109/TGRS.2010.2040034.

Mironov, V.L., Dobson, M.C., Kaupp, V.H., Komarov, S.A., Kleshchenko, V.N., 2004. Generalized refractive mixing dielectric model for moist soils. IEEE Transactions on Geoscience and Remote Sensing 42, 773–785. doi:10.1109/TGRS.2003.823288.

Mironov, V.L., Kosolapova, L.G., Fomin, S.V., Savin, I.V., 2019. Experimental Analysis and Empirical Model of the Complex Permittivity of Five Organic Soils at 1.4 GHz in the Temperature Range From -30 °C to 25 °C. IEEE Transactions on Geoscience and Remote Sensing 57, 1–10. doi:10.1109/TGRS.2018.2887117.

Mironov, V.L., Molostov, I.P., Luki, Y.I., Karavaysky, A.Y., Fomin, S.V., 2017. Frequency-, temperature-, and texture-dependent dielectric model for frozen and thawed arctic mineral soils, in: 2017 Progress In Electromagnetics Research Symposium - Spring (PIERS), IEEE. pp. 2546–2553. doi:10.1109/PIERS.2017.8262181.

Morgenstern, A., Grosse, G., Günther, F., Fedorova, I., Schirrmeister, L., 2011. Spatial analyses of thermokarst lakes and basins in Yedoma landscapes of the Lena Delta. The Cryosphere 5, 849–867. doi:10.5194/tc-5-849-2011.

Mu, C., Abbott, B.W., Zhao, Q., Su, H., Wang, S.F., Wu, Q.B., Zhang, T., Wu, X.D., 2017. Permafrost collapse shifts alpine tundra to a carbon source but reduces N2O and CH4 release on the northern Qinghai-Tibetan Plateau. Geophysical Research Letters 44, 8945–8952. doi:10.1002/2017gl074338.

Mu, C., Zhang, T., Wu, Q.B., Zhang, X., Cao, B., Wang, Q., Peng, X., Cheng, G., 2014. Stable carbon isotopes as indicators for permafrost carbon vulnerability in upper reach of Heihe River basin, northwestern China. Quaternary International 321, 71–77. doi:10.1016/j.quaint.2013.12.001.

Mu, C., Zhang, T., Zhang, X., Li, L., Guo, H., Zhao, Q., Cao, L., Wu, Q., Cheng, G., 2016. Carbon loss and chemical changes from permafrost collapse in the northern Tibetan Plateau. Journal of Geophysical Research: Biogeosciences 121, 1781–1791. doi:10.1002/2015JG003235.

Nauta, A.L., Heijmans, M.M.P.D., Blok, D., Limpens, J., Elberling, B., Gallagher, A., Li, B., Petrov, R.E., Maximov, T.C., van Huissteden, J., Berendse, F., 2015. Permafrost collapse after shrub removal shifts tundra ecosystem to a methane source. Nature Climate Change 5, 67–70. doi:10.1038/nclimate2446.

Nelson, F.E., Anisimov, O.A., Shiklomanov, N.I., 2001. Subsidence risk from thawing permafrost. Nature 410, 889–890. doi:10.1038/35073746.

Nelson, F.E., Anisimov, O.A., Shiklomanov, N.I., 2002. Climate Change and Hazard Zonation in the Circum-Arctic Permafrost Regions. Natural Hazards 26, 203–225. doi:10.1023/a:1015612918401.

Nelson, F.E., Shiklomanov, N.I., Mueller, G.R., Hinkel, K.M., Walker, D.A., Bockheim, J.G., 1997. Estimating Active-Layer Thickness over a Large Region: Kuparuk River Basin, Alaska, U.S.A. Arctic and Alpine Research 29, 367–378. doi:10.2307/1551985.

Obu, J., Lantuit, H., Grosse, G., Günther, F., Sachs, T., Helm, V., Fritz, M., 2017. Coastal erosion and mass wasting along the Canadian Beaufort Sea based on annual airborne LiDAR elevation data. Geomorphology 293, 331–346. doi:10.1016/j.geomorph.2016.02.014.

O'Donnell, J.A., Jorgenson, M.T., Harden, J.W., McGuire, A.D., Kanevskiy, M.Z., Wickland, K.P., 2012. The Effects of Permafrost Thaw on Soil Hydrologic, Thermal, and Carbon Dynamics in an Alaskan Peatland. Ecosystems 15, 213–229. doi:10.1007/s10021-011-9504-0.

Osterkamp, T.E., Viereck, L., Shur, Y., Jorgenson, M.T., Racine, C., Doyle, A., Boone, R.D., 2000. Observations of Thermokarst and Its Impact on Boreal Forests in Alaska, U.S.A. Arctic, Antarctic, and Alpine Research 32, 303–315. doi:10.2307/1552529.

Oveisgharan, S., 2007. Estimating snow accumulation from InSAR correlation observations. Ph.D. thesis. Stanford Univeristy.

Parizzi, A., Brcic, R., 2011. Adaptive InSAR stack multilooking exploiting amplitude statistics: A comparison between different techniques and practical results. Geoscience and Remote Sensing Letters, IEEE 8, 441–445. doi:10.1109/LGRS.2010.2083631.

Pettitt, A.N., 1976. A Two-Sample Anderson–Darling Rank Statistic. Biometrika 63, 161. doi:10.2307/2335097.

Rizzoli, P., Martone, M., Gonzalez, C., Wecklich, C., Borla Tridon, D., Bräutigam, B., Bachmann, M., Schulze, D., Fritz, T., Huber, M., Wessel, B., Krieger, G., Zink, M., Moreira, A., 2017. Generation and performance assessment of the global TanDEM-X digital elevation model. ISPRS Journal of Photogrammetry and Remote Sensing 132, 119–139. doi:10.1016/j.isprsjprs.2017.08.008.

Romanovsky, V.E., Osterkamp, T.E., 2000. Effects of unfrozen water on heat and mass transport processes in the active layer and permafrost. Permafrost and Periglacial Processes 11, 219–239. doi:10.1002/1099-1530(200007/09)11:3<219::AID-PPP352>3.0.CO;2-7.

Rosen, P.A., Gurrola, E., Sacco, G.F., Zebker, H., 2012. The InSAR scientific computing environment, in: Synthetic Aperture Radar, 2012. EUSAR. 9th European Conference on, VDE. pp. 730–733.

Roth, K., Boike, J., 2001. Quantifying the thermal dynamics of a permafrost site near Ny-Ålesund, Svalbard. Water Resources Research 37, 2901–2914. doi:10.1029/2000WR000163.

Samiei Esfahany, S., 2017. Exploitation of distributed scatterers in synthetic aperture radar interferometry. Ph.D. thesis. Technische Universiteit Delft.

Samiei-Esfahany, S., Martins, J.E., van Leijen, F., Hanssen, R.F., 2016. Phase Estimation for Distributed Scatterers in InSAR Stacks Using Integer Least Squares Estimation. IEEE Transactions on Geoscience and Remote Sensing PP, 1–17. doi:10.1109/TGRS.2016.2566604.

Sandwell, D.T., Price, E.J., 1998. Phase gradient approach to stacking interferograms. Journal of Geophysical Research: Solid Earth 103, 30183–30204. doi:10.1029/1998JB900008.

Schadel, C., Bader, M.K.F., Schuur, E.A.G., Biasi, C., Bracho, R., Capek, P., De Baets, S., Diakova, K., Ernakovich, J., Estop-Aragones, C., Graham, D.E., Hartley, I.P., Iversen, C.M., Kane, E., Knoblauch, C., Lupascu, M., Martikainen, P.J., Natali, S.M., Norby, R.J., O/'Donnell, J.A., Chowdhury, T.R., Santruckova, H., Shaver, G., Sloan, V.L., Treat, C.C., Turetsky, M.R., Waldrop, M.P., Wickland, K.P., 2016. Potential carbon emissions dominated by carbon dioxide from thawed permafrost soils. Nature Climate Change 6, 950–953. doi:10.1038/nclimate3054.

Schirrmeister, L., Froese, D., Tumskoy, V., Grosse, G., Wetterich, S., 2013. Yedoma: Late Pleistocene Ice-Rich Syngenetic Permafrost of Beringia, in: Encyclopedia of Quaternary Science: Second Edition. Elsevier Inc., pp. 542–552. doi:10.1016/B978-0-444-53643-3.00106-0.

Schirrmeister, L., Kunitsky, V., Grosse, G., Wetterich, S., Meyer, H., Schwamborn, G., Babiy, O., Derevyagin, A., Siegert, C., 2011. Sedimentary characteristics and origin of the Late Pleistocene Ice Complex on north-east Siberian Arctic coastal lowlands and islands – A review. Quaternary International 241, 3–25. doi:10.1016/j.quaint.2010.04.004.

Schneider, J., Grosse, G., Wagner, D., 2009. Land cover classification of tundra environments in the Arctic Lena Delta based on Landsat 7 ETM+ data and its applica-

tion for upscaling of methane emissions. Remote Sensing of Environment 113, 380–391. doi:10.1016/j.rse.2008.10.013.

Schuur, E.A.G., Bockheim, J., Canadell, J.G., Euskirchen, E., Field, C.B., Goryachkin, S.V., Hagemann, S., Kuhry, P., Lafleur, P.M., Lee, H., Mazhitova, G., Nelson, F.E., Rinke, A., Romanovsky, V.E., Shiklomanov, N., Tarnocai, C., Venevsky, S., Vogel, J.G., Zimov, S.A., 2008. Vulnerability of Permafrost Carbon to Climate Change: Implications for the Global Carbon Cycle. BioScience 58, 701–714. doi:10.1641/b580807.

Schuur, E.A.G., McGuire, A.D., Schadel, C., Grosse, G., Harden, J.W., Hayes, D.J., Hugelius, G., Koven, C.D., Kuhry, P., Lawrence, D.M., Natali, S.M., Olefeldt, D., Romanovsky, V.E., Schaefer, K., Turetsky, M.R., Treat, C.C., Vonk, J.E., 2015. Climate change and the permafrost carbon feedback. Nature 520, 171–179. doi:10.1038/nature14338.

Schwamborn, G., Rachold, V., Grigoriev, M.N., 2002. Late Quaternary sedimentation history of the Lena Delta. Quaternary International 89, 119–134. doi:10.1016/S1040-6182(01)00084-2.

Shiklomanov, N.I., Streletskiy, D.A., Little, J.D., Nelson, F.E., 2013. Isotropic thaw subsidence in undisturbed permafrost landscapes. Geophysical Research Letters 40, 6356–6361. doi:10.1002/2013GL058295.

Shiklomanov, N.I., Streletskiy, D.A., Nelson, F.E., Hollister, R.D., Romanovsky, V.E., Tweedie, C.E., Bockheim, J.G., Brown, J., 2010. Decadal variations of active-layer thickness in moisture-controlled landscapes, Barrow, Alaska. Journal of Geophysical Research: Biogeosciences 115, G00I04. doi:10.1029/2009JG001248.

Shiklomanov, N.I., Streletskiy, D.A., Swales, T.B., Kokorev, V.A., 2017. Climate Change and Stability of Urban Infrastructure in Russian Permafrost Regions: Prognostic As-

sessment based on GCM Climate Projections. Geographical Review 107, 125–142. doi:10.1111/gere.12214.

Short, N., Brisco, B., Couture, N., Pollard, W., Murnaghan, K., Budkewitsch, P., 2011. A comparison of TerraSAR-X, RADARSAT-2 and ALOS-PALSAR interferometry for monitoring permafrost environments, case study from Herschel Island, Canada. Remote Sensing of Environment 115, 3491–3506. doi:10.1016/j.rse.2011.08.012.

Short, N., LeBlanc, A.M., Sladen, W., Oldenborger, G., Mathon-Dufour, V., Brisco, B., 2014. RADARSAT-2 D-InSAR for ground displacement in permafrost terrain, validation from Iqaluit Airport, Baffin Island, Canada. Remote Sensing of Environment 141, 40–51. doi:10.1016/j.rse.2013.10.016.

Stoica, 2005. Spectral analysis of signals 452, Upper Saddle River, NJ: Pearson Prentice Hall.

Strauss, J., Schirrmeister, L., Grosse, G., Fortier, D., Hugelius, G., Knoblauch, C., Romanovsky, V., Schädel, C., Schneider von Deimling, T., Schuur, E.A.G., Shmelev, D., Ulrich, M., Veremeeva, A., 2017. Deep Yedoma permafrost: A synthesis of depositional characteristics and carbon vulnerability. Earth-Science Reviews 172, 75–86. doi:10.1016/j.earscirev.2017.07.007.

Streletskiy, D.A., Shiklomanov, N.I., Little, J.D., Nelson, F.E., Brown, J., Nyland, K.E., Klene, A.E., 2017. Thaw Subsidence in Undisturbed Tundra Landscapes, Barrow, Alaska, 1962-2015. Permafrost and Periglacial Processes 28, 566–572. doi:10.1002/ppp.1918.

Streletskiy, D.A., Shiklomanov, N.I., Nelson, F.E., 2012. Permafrost, Infrastructure, and Climate Change: A GIS-Based Landscape Approach to Geotechnical Modeling. Arctic, Antarctic, and Alpine Research 44, 368–380. doi:10.1657/1938-4246-44.3.368.

Streletskiy, D.A., Suter, L.J., Shiklomanov, N.I., Porfiriev, B.N., Eliseev, D.O., 2019. Assessment of climate change impacts on buildings, structures and infrastructure in the

Russian regions on permafrost. Environmental Research Letters 14, 025003. doi:10.1088/1748-9326/aaf5e6.

Tarjan, R., 1972. Depth-First Search and Linear Graph Algorithms. SIAM Journal on Computing 1, 146–160. doi:10.1137/0201010.

Ulrich, M., Grosse, G., Strauss, J., Schirrmeister, L., 2014. Quantifying Wedge-Ice Volumes in Yedoma and Thermokarst Basin Deposits. Permafrost and Periglacial Processes 25, 151–161. doi:10.1002/ppp.1810.

Vonk, J.E., Tank, S.E., Bowden, W.B., Laurion, I., Vincent, W.F., Alekseychik, P., Amyot, M., Billet, M.F., Canário, J., Cory, R.M., Deshpande, B.N., Helbig, M., Jammet, M., Karlsson, J., Larouche, J., MacMillan, G., Rautio, M., Walter Anthony, K.M., Wickland, K.P., 2015. Reviews and syntheses: Effects of permafrost thaw on Arctic aquatic ecosystems. Biogeosciences 12, 7129–7167. doi:10.5194/bg-12-7129-2015.

Walter Anthony, K., Daanen, R., Anthony, P., Schneider von Deimling, T., Ping, C.L., Chanton, J.P., Grosse, G., 2016. Methane emissions proportional to permafrost carbon thawed in Arctic lakes since the 1950s. Nature Geoscience 9, 679–682. doi:10.1038/ngeo2795.

Walvoord, M.A., Kurylyk, B.L., 2016. Hydrologic Impacts of Thawing Permafrost-A Review. Vadose Zone Journal 15. doi:10.2136/vzj2016.01.0010.

Wang, J.R., 1980. The dielectric properties of soil-water mixtures at microwave frequencies. Radio Science 15, 977–985. doi:10.1029/RS015i005p00977.

Wang, S., Jin, H., Li, S., Zhao, L., 2000. Permafrost degradation on the Qinghai-Tibet Plateau and its environmental impacts. Permafrost and Periglacial Processes 11, 43–53. doi:10.1002/(sici)1099-1530(200001/03)11:1<43::aid-ppp332>3.0.co;2-h.

Werner, C., Wegmüller, U., Strozzi, T., Wiesmann, A., 2000. Gamma SAR and interferometric processing software, in: Proceedings of the ERS-ENVISAT Symposium, Gothenburg, Sweden, p. 1620.

Wessel, B., 2016. TanDEM-X Ground Segment–DEM Products Specification Document. Technique Note 3.1. German Aerospace Center (DLR) .

Wright, T.J., Parsons, B.E., Lu, Z., 2004. Toward mapping surface deformation in three dimensions using InSAR. Geophysical Research Letters 31, L01607. doi:10.1029/2003GL018827.

Wu, Q., Zhang, T., 2008. Recent permafrost warming on the Qinghai-Tibetan Plateau. Journal of Geophysical Research: Atmospheres (1984–2012) 113, D13108. doi:10.1029/2007JD009539.

Wu, Q., Zhang, T., Liu, Y., 2010. Permafrost temperatures and thickness on the Qinghai-Tibet Plateau. Global and Planetary Change 72, 32–38. doi:10.1016/j.gloplacha.2010.03.001.

Yagüe-Martínez, N., Prats-Iraola, P., González, F.R., Brcic, R., Shau, R., Geudtner, D., Eineder, M., Bamler, R., 2016. Interferometric Processing of Sentinel-1 TOPS Data. IEEE Transactions on Geoscience and Remote Sensing 54, 2220–2234. doi:10.1109/TGRS.2015.2497902.

Yershov, E.D., 1998. General Geocryology. Cambridge University Press, Cambridge. doi:10.1017/CBO9780511564505.

Yu, C., Li, Z., Penna, N.T., Crippa, P., 2018. Generic Atmospheric Correction Model for Interferometric Synthetic Aperture Radar Observations. Journal of Geophysical Research: Solid Earth 123, 9202–9222. doi:10.1029/2017JB015305.

Zebker, H.A., Rosen, P.A., Hensley, S., 1997. Atmospheric effects in interferometric synthetic aperture radar surface deformation and topographic maps. Journal of Geophysical Research: Solid Earth 102, 7547–7563. doi:10.1029/96JB03804.

Zebker, H.A., Villasenor, J., 1992. Decorrelation in interferometric radar echoes. Geoscience and Remote Sensing, IEEE Transactions on 30, 950–959. doi:10.1109/36.175330.

Zhang, T., Baker, T.H.W., Cheng, G.D., Wu, Q., 2008. The Qinghai–Tibet Railroad: A milestone project and its environmental impact. Cold Regions Science and Technology 53, 229–240. doi:10.1016/j.coldregions.2008.06.003.

Zimov, S.A., Schuur, E.A.G., Chapin, F.S., 2006. Permafrost and the Global Carbon Budget. Science 312, 1612–1613. doi:10.1126/science.1128908.

Zou, D., Zhao, L., Sheng, Y., Chen, J., Hu, G., Wu, T., Wu, J., Xie, C., Wu, X., Pang, Q., Wang, W., Du, E., Li, W., Liu, G., Li, J., Qin, Y., Qiao, Y., Wang, Z., Shi, J., Cheng, G., 2017. A new map of permafrost distribution on the Tibetan Plateau. The Cryosphere 11, 2527–2542. doi:10.5194/tc-11-2527-2017.

Zwieback, S., Hensley, S., Hajnsek, I., 2015a. A Polarimetric First-Order Model of Soil Moisture Effects on the DInSAR Coherence. Remote Sensing 7, 7571. doi:10.3390/rs70607571.

Zwieback, S., Hensley, S., Hajnsek, I., 2015b. Assessment of soil moisture effects on L-band radar interferometry. Remote Sensing of Environment 164, 77–89. doi:10.1016/J.RSE.2015.04.012.

Zwieback, S., Hensley, S., Hajnsek, I., 2017. Soil Moisture Estimation Using Differential Radar Interferometry: Toward Separating Soil Moisture and Displacements. IEEE Transactions on Geoscience and Remote Sensing PP, 1–15. doi:10.1109/TGRS.2017.2702099.

Zwieback, S., Kokelj, S.V., Günther, F., Boike, J., Grosse, G., Hajnsek, I., 2018. Subseasonal thaw slump mass wasting is not consistently energy limited at the landscape scale. The Cryosphere 12, 549–564. doi:10.5194/tc-12-549-2018.

Zwieback, S., Liu, X., Antonova, S., Heim, B., Bartsch, A., Boike, J., Hajnsek, I., 2016. A Statistical Test of Phase Closure to Detect Influences on DInSAR Deformation Estimates Besides Displacements and Decorrelation Noise: Two Case Studies in High-Latitude Regions. IEEE Transactions on Geoscience and Remote Sensing 54, 5588–5601. doi:10.1109/TGRS.2016.2569435.